The Chemistry and Dynamics of Marine Stratocumulus

by
Stephan Randolph Kawa

Department of Atmospheric Science
Colorado State University
Fort Collins, Colorado

Richard Pearson Jr. – Principal Investigator

Colorado State University

Department of Atmospheric Science

Paper No. 430

THE CHEMISTRY AND DYNAMICS OF MARINE STRATOCUMULUS

by
Stephan Randolph Kawa

Richard Pearson, Jr.
Principal Investigator

Researh supported by the
National Science Foundation
under Grants ATM-8311405,
ATM-8312615, and ATM-8614956

Department of Atmospheric Science
Colorado State University
Fort Collins, Colorado

September, 1988

Atmospheric Science Paper No. 430

ABSTRACT

This thesis is a study of ozone chemistry and meteorological processes occurring in the eastern North Pacific stratocumulus regime. This climatological regime is characterized by widespread, persistent low cloud and an air history that does not include contact with continents for many days. Since both ozone and stratocumulus are important in the earth-atmosphere energy balance, the processes studied here are important in the system interactions that govern climate. The approach is analysis of observational data from the Dynamics and Chemistry of Marine Stratocumulus (DYCOMS) experiment.

Components of the regional ozone budget are investigated. Measurements of sea-surface deposition rate are smaller than most previous estimates. A significant variability of the rate exists. It is partially attributable to wind speed variation but appears to have other causes as well. Net photochemical production/destruction rate in the marine boundary layer is estimated using the ozone conservation relation. This rate, averaged over the flights, results in a small sink for ozone. This is an important verification of photochemical model predictions. Finally, the common presence of sharply defined concentration layers in the free troposphere is documented. These layers are shown to affect boundary layer concentration through entrainment and their possible origins are discussed.

Dynamical and thermodynamical processes controlling stratocumulus cloud layers are investigated. The entrainment rate of free tropospheric air into the cloud layer is calculated using a new method based on ozone conservation. This rate is compared to thermodynamic fluxes and previous estimates toward parameterization of entrainment for mixed-layer models. Layer average thermodynamic energy budgets are constructed. Divergence of solar radiation is a major component

for midday cases which complicates traditional mixed-layer model assumptions. Longwave radiative profiles consistently show good agreement with theoretical models, but the distribution of flux between inversion and mixed layers is not decided.

Budgets and mean distributions are also examined for several cases which are not typical of the generally cloudy conditions. These demonstrate the role of clouds in determining boundary layer structure and provide examples of cloud clearing and reformation. These transitions are shown to occur in response to a number of different perturbations.

ACKNOWLEDGEMENTS

For their help and guidance in this research, I wish to thank the members of my graduate committee: co-advisor Professor Wayne Schubert, Dr. Donald Lenschow, Professors Richard H. Johnson and Steven Strauss. Professor Stephen Cox has also made significant contribution. I thank Ms. Cindy Carrick for her expert preparation of the manuscript. Special thanks go to my wife Nancy and daughter Elizabeth for their patience and support. Aircraft and computing facilities were provided by the Research Aviation Facility and the Scientific Computing Division of the National Center for Atmospheric Research (NCAR). NCAR is sponsored by the National Science Foundation. This research has been supported by National Science Foundation grants ATM-8311405, ATM-8312615, and ATM-8614956.

Table of Contents

List of Figures

List of Tables

Chapter 1: INTRODUCTION

The climate of the earth is constantly changing. These changes occur on a wide range of time scales in response to many different perturbations. Climate response to any imposed forcing depends on an inscrutably complicated interactive network of natural processes encompassing the atmosphere, oceans, and biosphere. In order to deal with the effects of climate change we must better understand the causes and effects. Two of the major role players in this chain are clouds and trace gases, because of their influence on the net energy balance of the earth-atmosphere system. This paper is specifically directed to stratocumulus (SC) clouds and ozone (O_3) gas. SC is particularly important for its large areal extent and long persistence (Schubert et al., 1979a). O_3 is a radiatively important gas itself as well as a major reactant in the chemical lifecycles of other trace gases. The general goal of this research is to achieve a better scientific understanding of the processes controlling SC and O_3 in the atmosphere. This research is directly relevant to understanding earth's climate as well as to predicting local effects of SC cloud cover and oxidant concentration.

The basic approach in this paper is an observational one. Measurements are analyzed within several theoretical frameworks and conclusions are drawn regarding the nature of the physical processes. The experimental program is the Dynamics and Chemistry of Marine Stratocumulus (DYCOMS) experiment (Lenschow et al., 1988a). DYCOMS was an aircraft sampling program using the NCAR Electra equipped with an extensive array of meteorological and chemical instrumentation of the highest research quality. The flight mission was an almost total success providing more than 70 hours of high resolution, mean and fast

response data. Many of these data were unique and they are surely the most comprehensive reported to date for the SC regime.

The available data lead to the specific goals of this research. These are to evaluate the contributions of various terms in the O_3 budget and to assess the thermodynamical/dynamical processes controlling the existence of SC. These form two largely independent topics of study in this paper. The background specific to these problems is in the respective sections. Generally, these problems have been studied rather extensively through numerical modeling but observational analysis has lagged behind. Usually this is due to instrument and sampling limitations. The results of DYCOMS should therefore be particularly welcome both as a primary analysis tool and as a basis for comparison with models. Some of the results, such as direct measurement of O_3 deposition and entrainment in the SC boundary layer are unique.

The outline of this paper is the following. Chapter 2 provides a physical description of the experimental procedure and the meteorological background. It has a rather detailed account of the response of some of the instruments and estimates of how this may affect the data. Chapter 3 is a documentation of the processing of sensor data into physical quantities and derived parameters. Much of the data needed for analysis in the two succeeding sections is compiled here along with some other data of potential interest. This data, and the complete set of soundings in Appendix A, is made available for further use as discussed in the chapter introduction. Chapter 4 focuses on the O_3 budget. Surface deposition, photochemistry, and mean distribution are addressed in detail. Chapter 5 pertains to SC thermodynamics and dynamics. The entrainment rate is calculated using O_3 measurements and compared among the cases and with previous findings. Layer average thermodynamic budgets are constructed including turbulent and radiative fluxes and mean transport. These are used to study the varying influence of the components and the applicability of mixed-layer concepts. The important findings of Chapters 4 and 5 are summarized separately in those chapters. Chapter 6 is a

brief overall summary and some suggestions for further research that have grown out of this study.

Chapter 2: DESCRIPTION OF THE EXPERIMENT

2.1 FLIGHT SUMMARY

There were 10 research flights during the DYCOMS project in 1985. Table 2.1 lists their dates, times, and general characteristics. All of the flights took place around local solar noon (13:00 Pacific Daylight Time, PDT) except Flight 10 which began an hour before sunrise. The locations of the flight patterns were chosen for the best cloud conditions that we wished to study (e.g. a clear region for Flight 8 and solid cloud for 1 to 5, 7 and 10) based on satellite photos, climatology, and in-flight observations. The locations of the initial flight legs, before advection, are shown in Fig. 2.1 (Flights 6, 8 and 9 proceeded entirely in the positions shown).

A standard flight pattern consists of a level ferry portion from San Diego to the research area at an altitude of 3200 m, a descent sounding to near the surface, a horizontal leg at about 50 m, two legs about halfway between the surface and cloud base, a leg at cloud base, one in cloud, one at cloud top, three legs at about 100 m above cloud top, and another descent sounding. The set of legs is then repeated up to cloud top. A descent sounding and an ascent to the return ferry altitude of 5000 m complete the pattern. Each leg was 15 minutes, or about 100 km long. The legs of flights called "x-wind" in Table 2.1 were oriented perpendicular to the mean wind. Those labeled "L's" had right angle turns in the middle of the legs and consisted of cross and along wind portions. The legs were flown at constant aircraft heading and advected along the mean wind except for Flight 8 which was anchored to geographical coordinates. Turns at the leg ends were made in the upwind direction in order to avoid possible contamination of the chemical

samples by aircraft exhaust. It should be noted here that these turns, as well as difficulty in maintaining tracks exactly perpendicular to the mean wind, mean that the flight legs were not always precisely collocated in the Lagrangian frame of reference. This becomes significant in the presence of horizontal gradients as discussed in Sec. 4.2.1. Flights 6 and 9 were flown along the direction of the mean wind at various altitudes, essentially out and back from the starting point. No budgets are calculated for Flights 6 and 9 since the pattern does not allow estimation of the vertical derivative terms.

2.2 METEOROLOGY

The synoptic scale meteorology during DYCOMS generally conformed to the established climatology for the region (Neiburger, 1960). This climatological regime is produced by northerly, descending flow on the eastern side of the subtropical anticyclone which dominates the Pacific during summer. The large scale circulation is shown schematically in Fig. 2.2 from Danielsen et al. (1987). Temperature and humidity of the air near the surface are strongly coupled to the sea surface temperature (SST); its distribution is given in Fig. 2.3 (Schubert et al. 1979b). A strong inversion usually separates the cool, moist air in contact with the surface from the dry, adiabatically- warmed free tropospheric air. The lifting condensation level is often reached within the moist marine boundary layer (MBL) and clouds are formed. The inversion is an effective lid on cloud growth and stratocumulus is produced.

While conditions during most DYCOMS flights fit the climatological picture, the cloud cover was by no means steady state during the 23 days of the experiment. Examination of satellite photographs reveals major fluctuations in the extent and uniformity of the SC coverage as well as the cellular nature of the cloud. To some degree these events can be correlated with synoptic perturbations of the climatological flow which can be observed on the weather maps. These

changes may be relevant to the detailed analyses in subsequent chapters. A brief chronology of significant deviations from the general flow pattern follows.

Figure 2.4 shows the 850 mb analysis for the morning of 30 July 1985, Flight 1. This map is fairly representative of the experimental period except possibly for the developing short wave between 40° and 50°N near 130°W. Cloud cover in the study region was solid (Table 1). The baroclinicity of the aforementioned shortwave appears to be responsible for a general clearing on the following day at 1200 PDT which extended from about 40°N to almost 30°N and west from the coast to about 130°W. The association of strong cold advection above the MBL with SC clearing has been discussed by Weaver (1987). The SC was quickly reestablished on 1 August and remained through 4 August, Flight 3. Another general clearing from the north proceeded on 5 and 6 August. The SC was reformed by Flight 4 on 7 August but less solidly than previous flights. After a brief intrusion of clear air from the north on 8 August, again probably associated with an 850 mb shortwave, SC was widespread and uniform for Flight 5 on 9 August through 12 August. On 13 August, Flight 6, the profound influence of a northwestward moving tropical storm, located at 25°N, 130°W, was felt in the study region. Clearing proceeded from the south extending to about 35°N on 14 August followed by the appearance of less stratiform, more cellular clouds which filled the region by Flight 7, 16 August as the tropical system dissipated. Stratus was well established on 17 August but on 18 August a clear area once again propagated from the north. Flight 8 was flown in this clear region which in fact was surrounded by cloudy regions except to the north. The clearing continued on 19 August when Flight 9 proceeded from the clear region, through the transition, into the cloudy region south of 28°N. The SC was fully present again on 20 August through Flight 10 on 21 August.

In summary then, Flights 1 to 5 and 10 may be characterized as typical of the generally cloudy conditions. Flight 6 sampled conditions influenced fairly directly by a tropical disturbance with Flight 7 in its aftermath. Flight 8 sampled within

the clear region associated with occasional cold disturbances from the north and Flight 9 sampled across this frontal-like boundary.

2.3 MEASUREMENT TECHNOLOGY

The measurement platform for DYCOMS was the NCAR Electra research aircraft which is maintained and operated by the NCAR Research Aviation Facility (RAF). The meteorological instrumentation package provides mean and turbulence data for wind components, temperature, and humidity, bandwidth limited at 10 Hz and output at 20 Hz. O_3 output characteristics are the same. Liquid water, aerosol, radiation, and complete navigational data were also recorded. A wide assortment of chemical sampling was carried out by individual investigators (Lenschow et al., 1988a).

Measurement of atmospheric scalars in a partly cloudy environment can be very difficult, especially at the high resolution and fast response required for eddy correlation. In some cases the instrument response characteristics may spuriously affect the output signal. I have tried very hard to remove the possibility of any such effects influencing the analysis but sensor limitations should always be kept in mind when evaluating conclusions. For this reason, and the fact that one DYCOMS objective was instrument evaluation, a discussion of quality control for certain data is included here.

Ambient water vapor is measured on the Electra, in the mean, by a cooled mirror dew-point hygrometer (EG&G Model 137-C3-S3) and, fluctuations, by a Lyman-alpha hygrometer (NCAR-developed). Neither instrument is satisfactory for all applications. The virtue of the Lyman-alpha is its very fast response time; its fault is an uncertain absolute calibration (Buck, 1976; Buck and Hills, 1980). In addition, the Lyman-alpha output is very sensitive to the presence of cloud droplets, even in low liquid water. Figure 2.5 shows time series for a segment of data taken at cloud base level. Greatly increased variance in the calibrated Lyman-alpha signal can be seen during periods where the aircraft encounters

liquid water, q_l. This can better be seen by comparing the spectra from cloud base and subcloud shown in Fig. 2.6. Uncorrelated sensor noise would not be a problem for flux analysis, but since liquid water is usually correlated with vertical velocity, we expect that the Lyman-alpha droplet interference will be correlated in some way with vertical velocity. Indeed this does seem to be the case. The cospectra for the same segments are shown in Fig. 2.7 and increased covariance peaks are present on the cloud base leg. The frequency dependence and the net effect of the droplet interference is not clear however since the difference in covariance may be due partly to the altitude difference. The fact that the droplet interference is positively correlated with vertical velocity is seen from the enhancement of flux at 630 m in Fig. 2.8. The total water flux profile for this case is expected from mixed layer theory to be very nearly straight. The conclusion is that water vapor fluxes measured by the Lyman-alpha in cloud are not reliable. The instrument also was not operational for most of Flight 7.

Use of the thermoelectric (EG&G) hygrometer for flux calculation has been suggested under certain conditions (Friehe et al., 1986). Comparison of Lyman-alpha and EG&G derived fluxes in clear air shows very poor agreement for DYCOMS cases however, probably due to their small magnitudes relative to those of Friehe et al. (1986, Fig. 7). The effect of cloud droplets on the EG&G signal appears to be negligible for the liquid water contents of DYCOMS. Figure 2.9 shows that the measured dewpoint T_D is within one-half degree of the ambient temperature T in cloud where saturation may be assumed. This is within the published accuracy limits of the instruments and no trend in offset with liquid water is detectable. The behavior of the T_D profile near cloud top points out two more of the EG&G's undesirable characteristics. The first is its tendency to overshoot and oscillate at sudden increases in humidity typical of the inversion top. The second is its slow response time as the change in T_D at the inversion comes slightly after (lower) than T and l. Examination of the calibrated EG&G time series in Fig. 2.5 shows that it is able to follow humidity fluctuations of

horizontal extent on the order of several hundred meters (several seconds) quite well. The result of this is that the EG&G has been used for all mean humidity measurements including soundings, where its occasional overshooting is obvious, but not for flux calculations.

Water vapor fluctuations in cloudy air may also be obtained from the temperature measurements if saturation is assumed. Figure 2.9 indicates that this assumption appears good for mean humidity but fluctuations still may deviate. In practice the humidity fluctuations in this paper are determined from a combination of these three sensor outputs as discussed in Sec. 3.4.1.

Temperature is measured by two instruments, a Rosemount (Model 102E2AL) and a K-probe (NCAR-developed). The K-probe has a faster response time but is sensitive to wetbulb cooling in the presence of cloud droplets. This is apparent in Fig. 2.5 especially between 13:00 and 13:01 and after 13:06 in comparison to the Rosemount. The design of the Rosemount is such that its output should not be sensitive to small liquid water amounts (Brost et al., 1982; Nicholls, 1984; Albrecht et al., 1985). Comparison of fluxes from the Rosemount and K-probe in clear air shows very good agreement. Figure 2.10 shows the coherence between them is high right up to 10 Hz and the phase lag is zero. For these reasons the ambient temperature measured by the Rosemount is used exclusively in this analysis and with good confidence. The SST is measured by a radiation thermometer (Barnes PRT-5) on the 50-m legs and should be accurate to within 1°C (Spyers-Duran and Winant, 1985).

Liquid water is measured by two resistance-type probes, the Johnson-Williams LW4 (J-W) and the Particle Measuring System (PMS) King probe. There are serious performance problems with the J-W that make using the King probe preferable (Baumgardner, 1983). The King probe is susceptible to baseline drifting and the intercept must be adjusted frequently over a flight. This is done during data processing as discussed in Sec. 3.1. As a result the King probe is not useful for detecting the presence of liquid water amounts below about 0.01 g m^{-3}.

The accuracy of the mean is expected to be within 10% (King et al., 1985). The frequency response of the device is inherently fast (Bradley and King, 1979) but during DYCOMS the instrument electronics were inadvertently set to introduce a 0.2 s time constant into the response. The effect of this lag on the output can be evaluated by writing the input/response relationship as the classic differential equation

$$\frac{dx}{dt} + ax = f(t)$$

where x represents the instrument response, $1/a = 0.2$ s the time constant, and $f(t)$ is the liquid water input over time. Assuming a sinusoidally varying input of frequency ω, the response attenuation is $a/\sqrt{a^2 + \omega^2}$. This effect becomes greater than 10% at frequencies above about 2.5 Hz. The liquid water spectrum in cloud has a peak variance at 0.2 to 0.3 Hz decreasing by an order of magnitude by 2 Hz. Almost all of the wq_l cospectral energy is at frequencies less than 1 Hz. The phase lag introduced is well accounted for at these frequencies by simply advancing the ouput 0.2 s. As a result the calculated liquid water fluxes may be slightly underestimated but not by more than 10%.

Liquid water may also be estimated by integrating over the droplet spectrum measured by the PMS Forward Scattering Spectrometer Probe (FSSP) but this method is generally less accurate than the resistance-type measurements (Baumgardner, 1983). Comparison of mean liquid water and flux between the FSSP and King probes does not show good agreement nor any systematic calibration difference for DYCOMS. The FSSP does have a constant zero baseline however and its output is used for determining whether or not liquid water is present down to small threshold values.

Winds on the Electra are determined from the Litton LTN-51 inertial navigation system (INS) and the NCAR-developed gust probe (Lenschow, 1972; Kopp, 1985). The gust probe system sometimes encountered problems during DYCOMS

near cloud edges. Spikes and unexplainable level shifts occur in the output on these occasions. Consequently, these periods have been edited from the data in order not to contaminate the flux analysis. This editing is a somewhat subjective procedure in which time series of attack vane difference, vertical velocity spectra, and fluxes are examined for evidence of unnatural variations. Generally, I have included all the data unless something is obviously wrong. The vane problems do contribute an experimental uncertainty to the flux measurements, especially at cloud base.

The O_3 instrument used during DYCOMS is an improved version of the fast response chemiluminescent analyzer of Pearson and Stedman (1980). It has an intrinsic bandwidth of at least 20 Hz which is electronically filtered at 10 Hz to match the meteorological sensors. It has high sensitivity and stability which permit O_3 measurements accurate to within 0.1 ppbv from 10 to 100 ppbv ambient mixing ratio (Pearson, 1988). Instrument response is slightly sensitive to the operating temperature, which was monitored during the program. The calibration changes have been calculated for DYCOMS operation. They amount to less than 0.1% and have been disregarded in processing. The water vapor sensitivity and lag time have been taken into account as described in Sec. 3.1.

The upward and downward components of the net radiative flux are available in three bandwidths: ultraviolet UV (0.295 to 0.385 μm) by Eppley TUVR, visible SW (0.285 to 2.800 μm) by Eppley PSP, and infrared LW (4 to 45 μm) by Eppley PIR silicon dome. Temperature correction and calibration of these instruments is done by RAF. The output is used as reported by them except that portions of data following abrupt altitude changes are excised to avoid temperature equilibration problems in the LW instrument.

Table 2.1: DYCOMS Flight Summary

FLIGHT	1	2	3	4	5	6	7	8	9	10
DATE	7/30	8/2	8/4	8/7	8/9	8/13	8/16	8/18	8/19	8/21
TIME (PDT)	10:56 to 17:56	09:01 to 16:04	09:56 to 16:46	09:54 to 17:09	09:49 to 17:00	10:40 to 15:36	10:16 to 17:32	10:02 to 17:00	10:57 to 18:03	05:25 to 12:35
TYPE	x-wind	x-wind	x-wind	x-wind	x-wind	along-wind	L's	L's	along-wind	L's
CLOUD	solid	near solid	broken	broken	near solid	scattered	broken, layered	clear	broken to clear	near solid

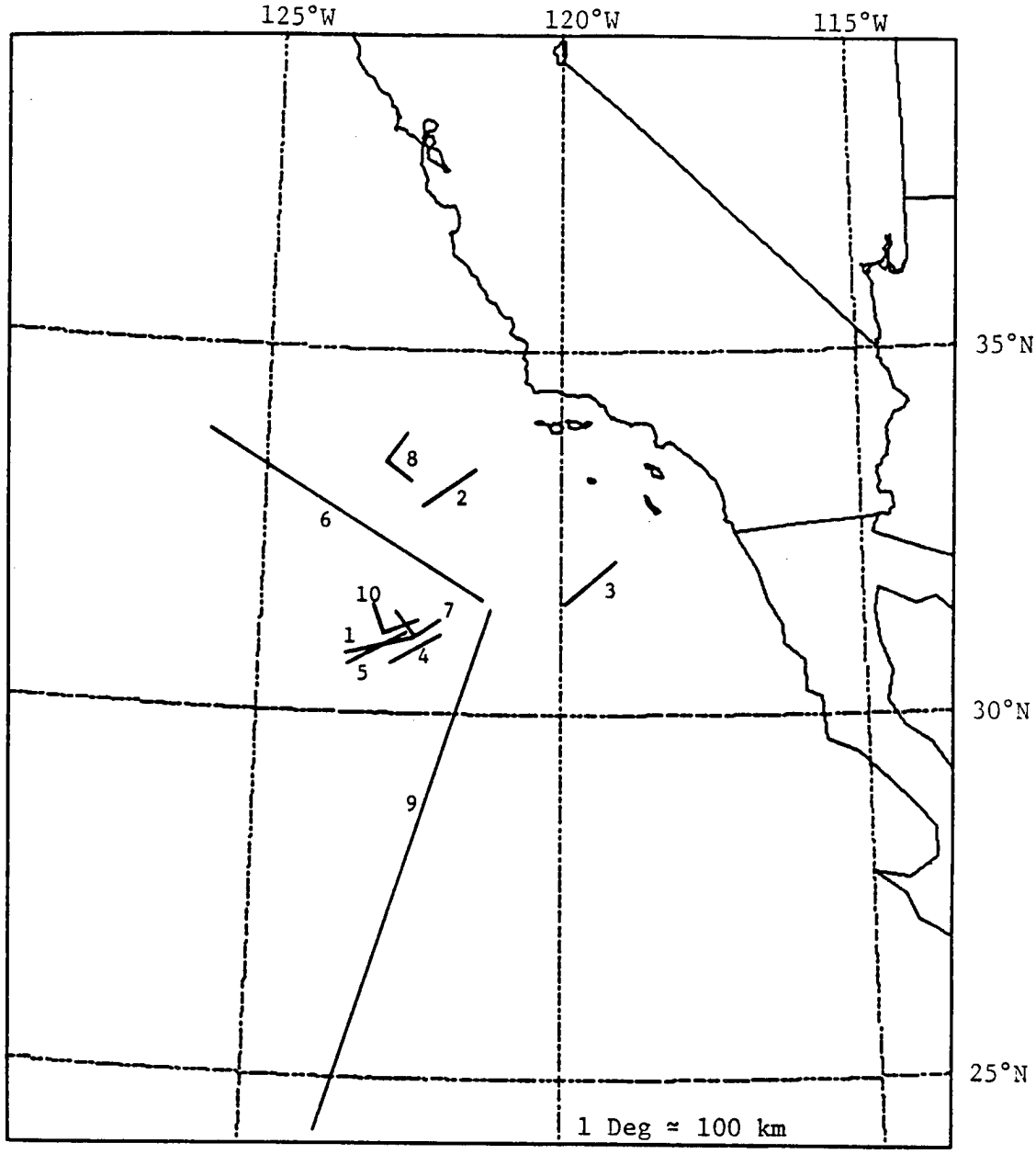

Figure 2.1: Locations of flight tracks. Shown are initial positions of the legs which were subsequently advected downwind. Flights 6 and 9 were simply flown out and back at various altitudes along the track shown, starting at the east end. Flight 8 "L's" were flown at a fixed position.

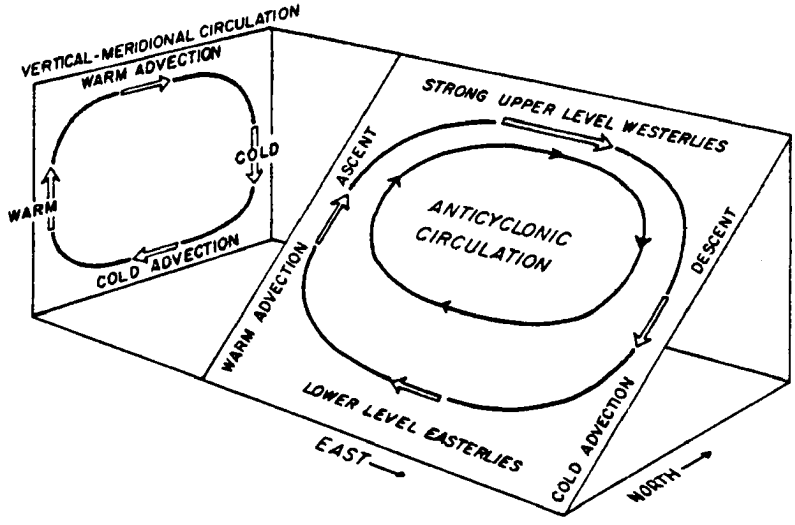

Figure 2.2: Vertical-meridional thermally direct circulation for a non-rotating earth and inclined anticyclonic circulation for the rotating earth. From Danielson et al. (1987).

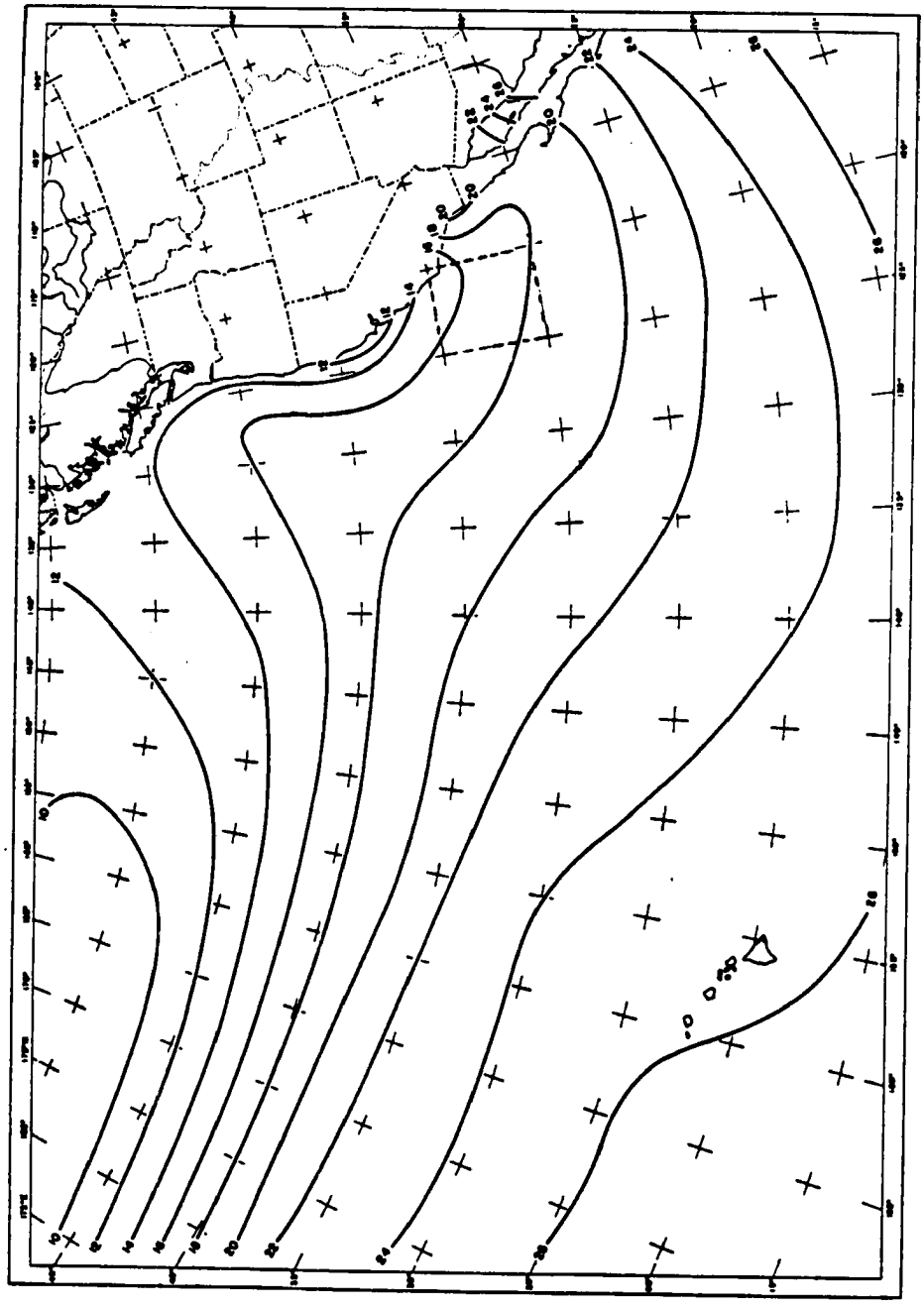

Figure 2.3: Mean sea surface temperature for July (°C). After Neiburger et al. (1961) from Schubert et al. (1979b). Dashed lines located DYCOMS region.

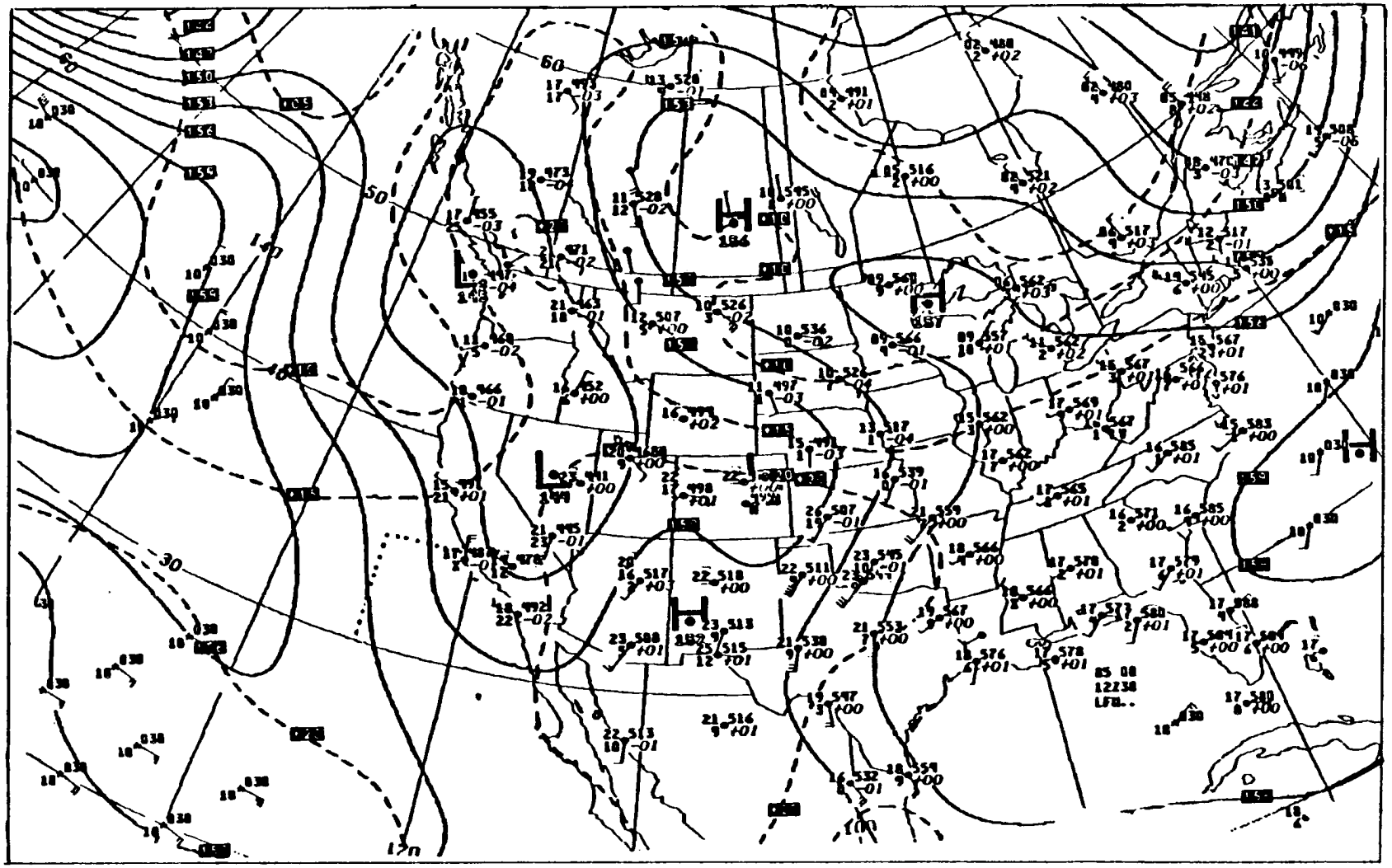

Figure 2.4: Temperature (dashed) and geopotential height (solid) at 850 mb, 12Z, 30 July 1985. Dotted lines locate DYCOMS region.

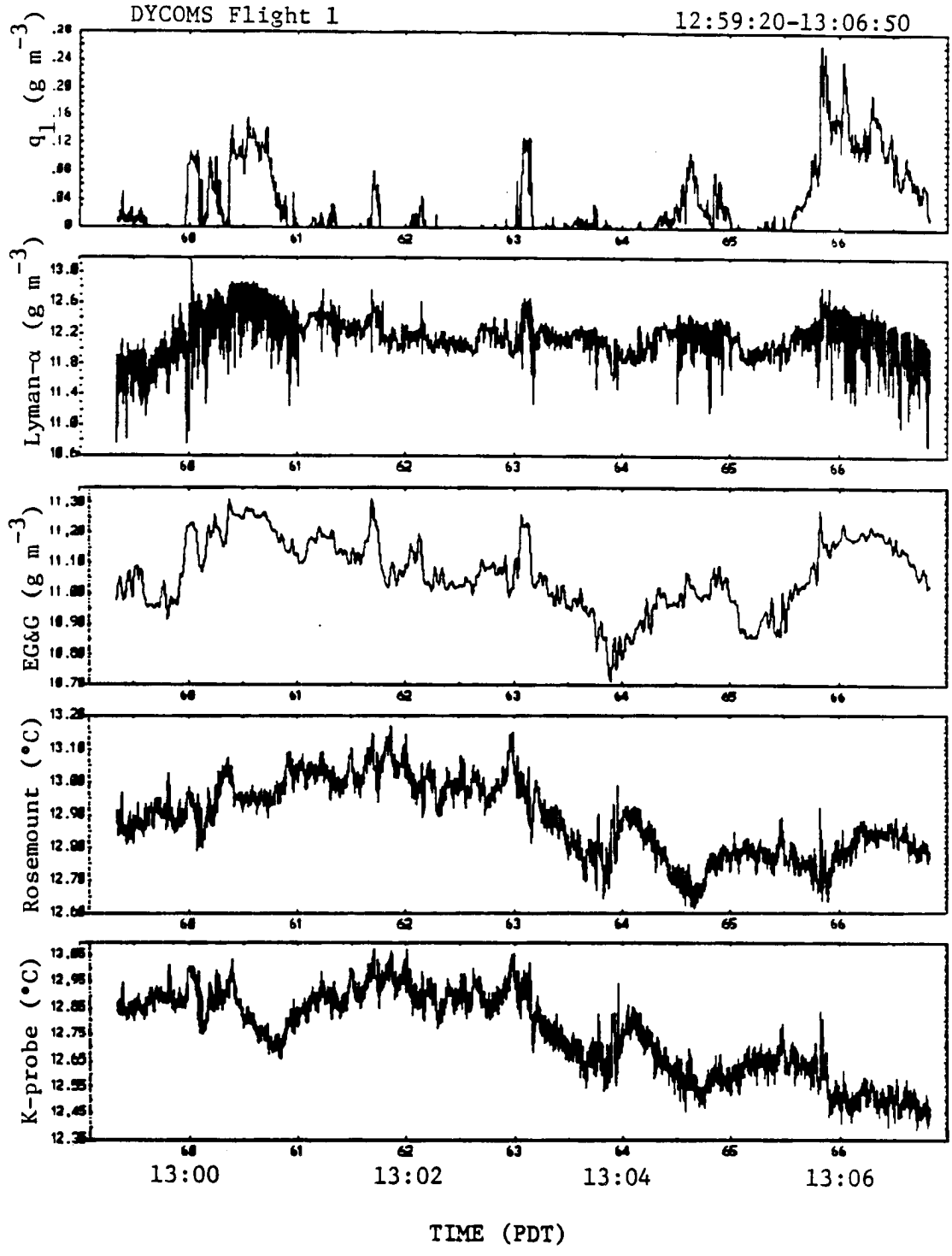

Figure 2.5: Time series at cloud base. See text for identification of sensors.

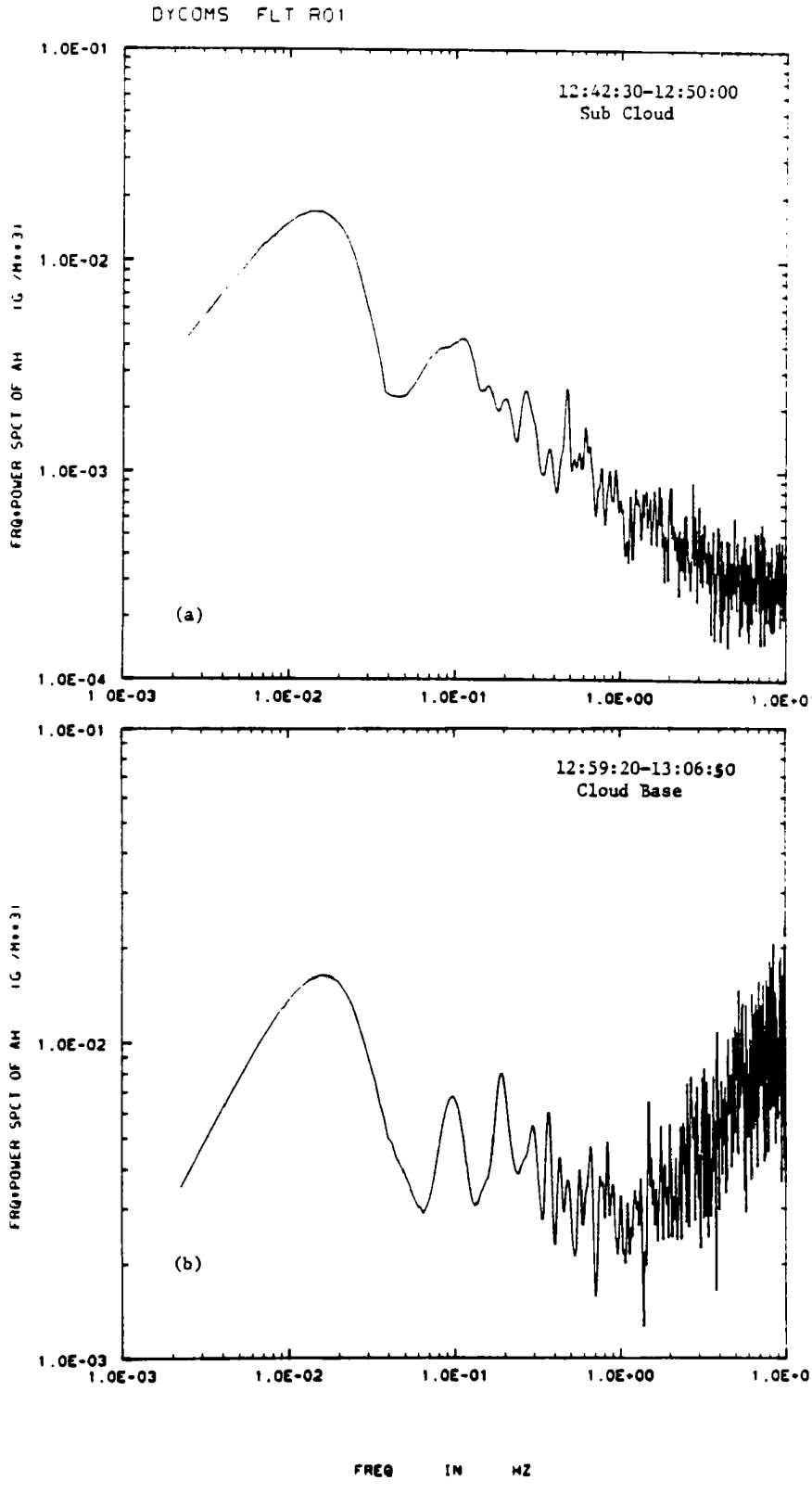

Figure 2.6: Power spectra of Lyman-alpha output from segments at 260 m (a) and 560 m (b).

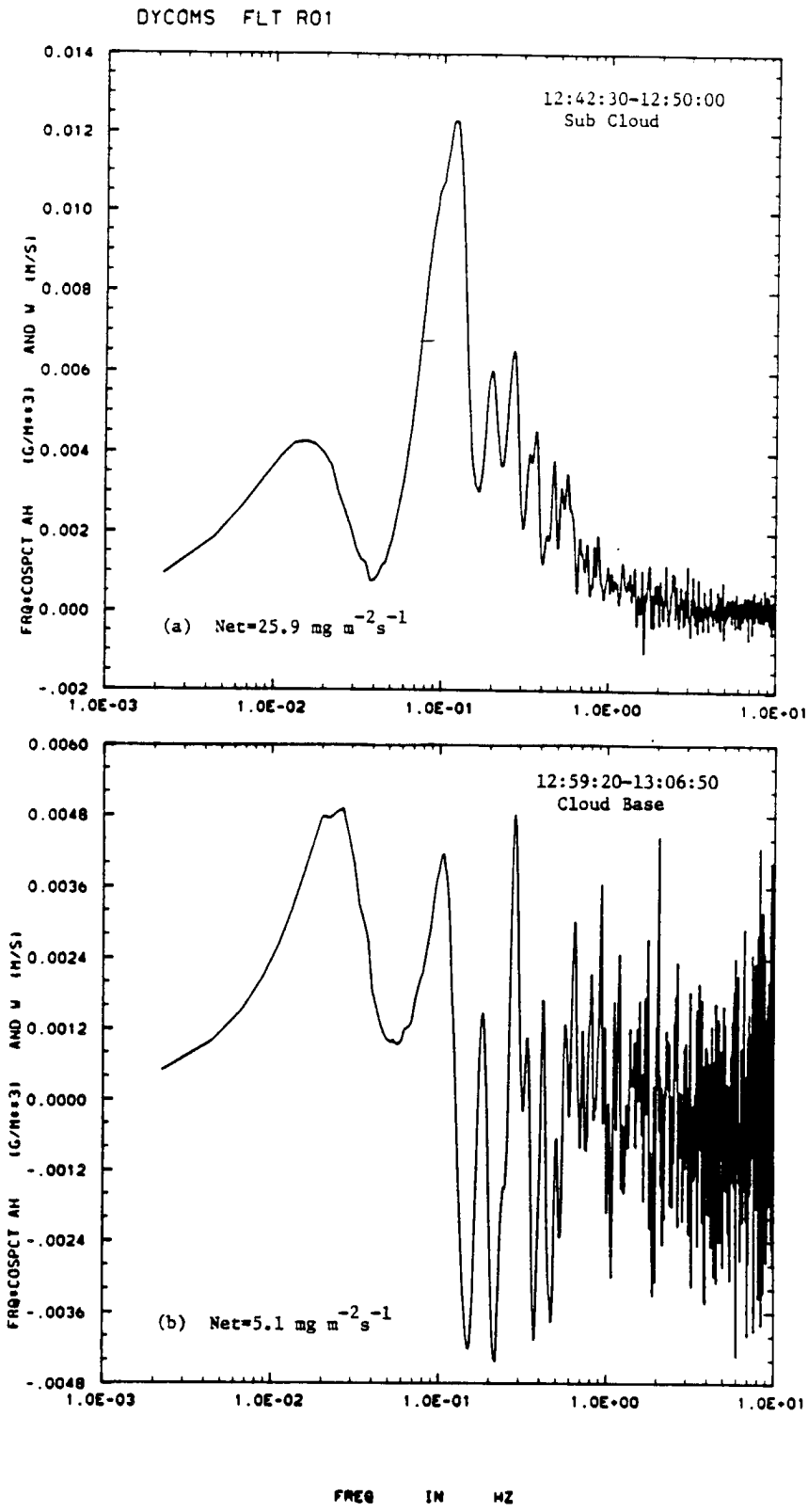

Figure 2.7: Cospectra of w and q_v from Lyman-alpha for same segments as Fig. 2.6.

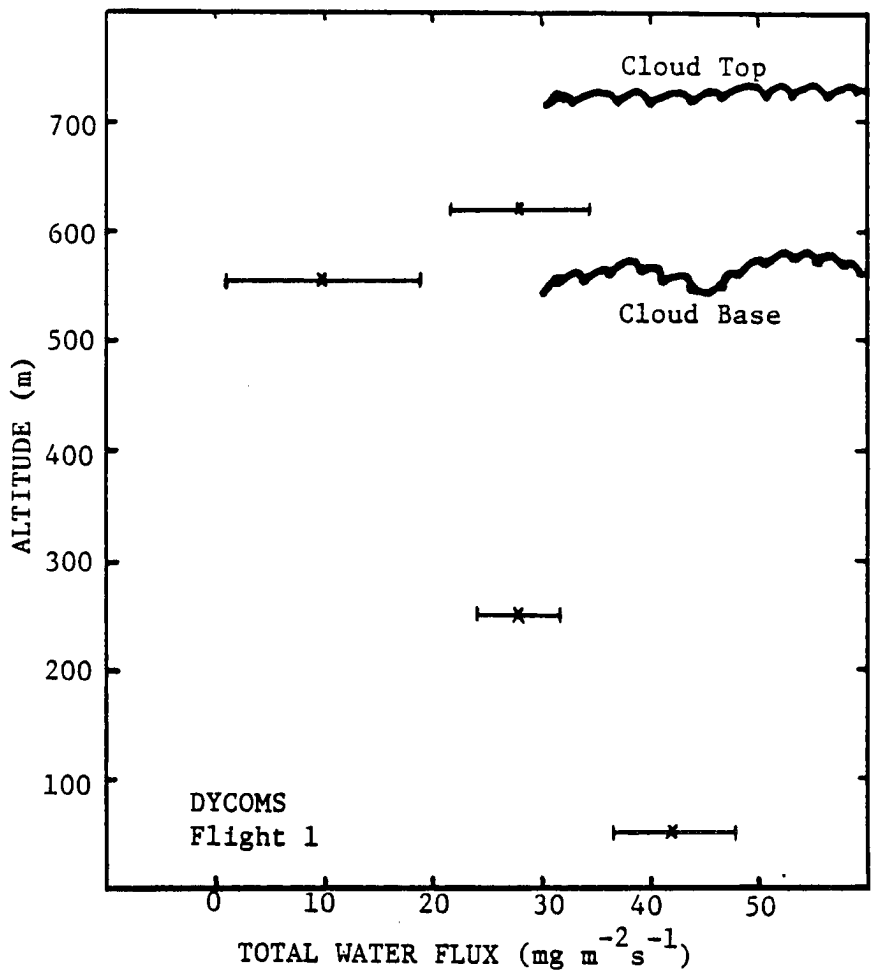

Figure 2.8: Total water flux derived from Lyman-alpha water vapor fluctuations and the King probe. Error bars are 90% confidence limits on the mean flux based on a Student t distribution.

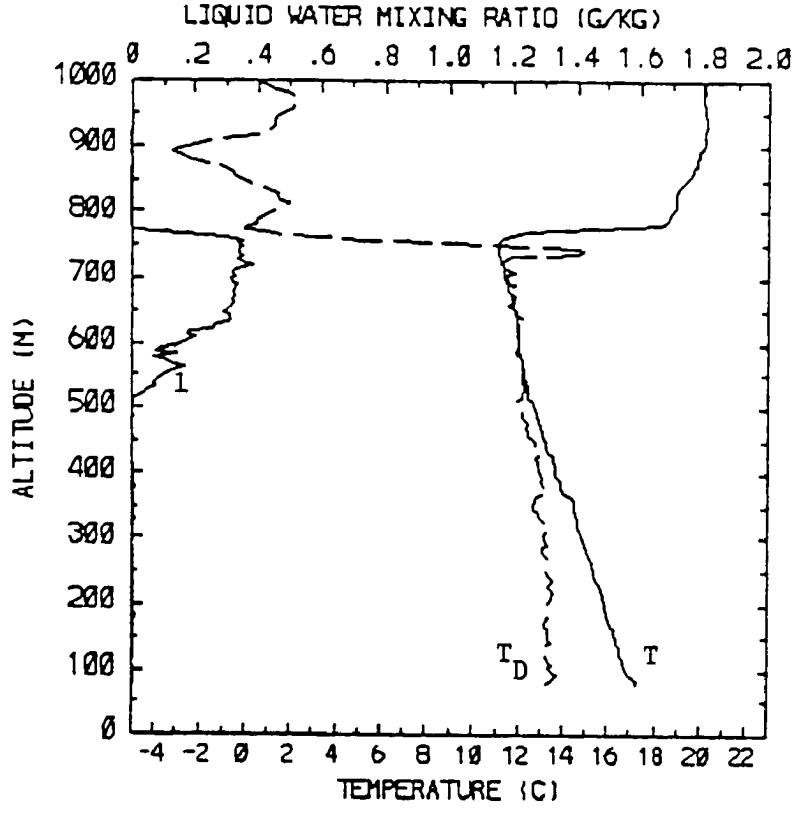

Figure 2.9: Descent sounding showing temperature (T), dewpoint (T_D), and liquid water (l) from Flight 1, 12:09-12:27 PDT.

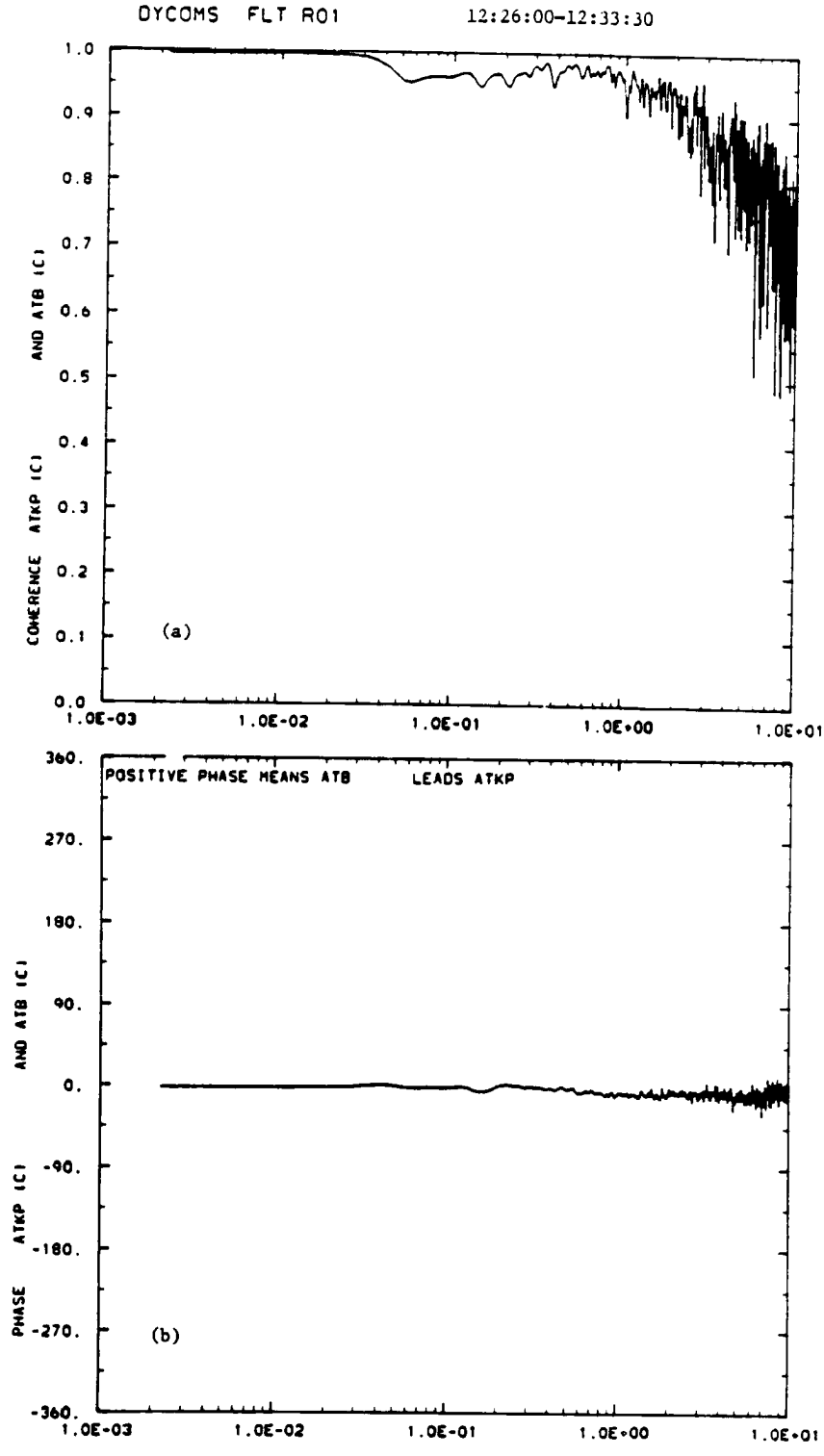

Figure 2.10: Coherence and phase between K-probe (ATKP) and Rosemount (ATB) calibrated temperatures near the surface.

Chapter 3: DYCOMS DATABASE AND SCALAR FLUXES

This chapter is intended to help fill the need for more observational data on the marine SC environment. The compiled data, required to address the scientific problems discussed in the next two chapters, form an extensive set of measured quantities and derived parameters. This data set can be used for initialization and validation of SC numerical models, for input to chemical transport/reaction models, to improve parameterizations in general circulation models, and for testing the representativeness of other observations.

The data are collected into a set of tables and figures. The accompanying text documents how the output variables are derived from measured quantities.

3.1 PREPROCESSING

Most of the preprocessing needed to transform raw sensor output into useful quantities is done by the RAF before making the data tapes available to users. A few of the output variables need further refinement to attain the most accurate measurement value. This process is detailed here.

In preprocessing, the O_3 data are corrected for water vapor quenching of the chemiluminescent reaction (Matthews et al., 1977; Lenschow et al., 1981). They have been advanced 0.2 s relative to the other data to account for the location of the O_3 probe aft of the gust probe and the sample residence time in the detector plumbing (Lenschow et al., 1982). Spurious electronic spikes are also removed.

The Lyman-alpha output voltage is calibrated by the method suggested by Friehe et al. (1986). This method uses a linear slope and intercept derived from comparison of the Lyman-alpha and the EG&G after advancing the EG&G

output, about 2 s, to account for its slower response time. Here the calibration coefficients are calculated for each data tape, about two hours of flight time, and assumed constant over that interval. The regression is performed for flight sections at several altitudes and averaged so the altitude dependence of the slope observed by Friehe et al. (1986) is neglected. The intercept is irrelevant for flux calculations. The resulting absolute humidity (q_v) fluxes may be underestimated by about 5% near the surface although the sensitivity decrease with time (0.5% hr^{-1}; Buck and Hills, 1980) would tend to offset this effect.

The King liquid water probe output is baselined during this stage of processing. This is done "by eye" for sections of the flight where liquid is encountered. For example in Fig. 3.1, 0.08 g m^{-3} would be added to the measurement for this period. Also during the preprocessing stage the output of several slow (1 Hz) sensors is interpolated to 20 Hz for convenience in later calculations.

3.2 SOUNDINGS

The complete set of soundings from DYCOMS is given in Appendix A, Figs. A.1 to A.24. They are vertical profiles of mean quantities averaged over 5-m height bins for low level (<2500 m) soundings and 10-m bins for deeper ones. The altitude z is obtained from the high range radio altimeter which may lose accuracy (±10 m) at less than about 100 m. The aircraft rate of ascent or descent is about 2 m s^{-1} in the lower part and 5 m s^{-1} above the boundary layer. The horizontal speed is about 105 m s^{-1}. Soundings are generally made on a slant path although are sometimes spiral as noted. A significant amount of horizontal averaging therefore, goes into the vertical average.

The sounding figures show plots of O_3 mixing ratio O_3, water vapor mixing ratio r from the EG&G sensor, and liquid water mixing ratio l from the King probe. Recall the overshooting value of r at the inversion top (e.g. Fig. A.1a) is an instrument problem, not an ambient phenomenon (Sec. 2.3). This example

shows a feature common to many of the r soundings above about 3000 m. The lower detectable limit of the EG&G is apparently about 0.8 g kg^{-1}.

Liquid water potential temperature θ_l is calculated (Betts, 1982) as

$$\theta_l = \theta \exp(-Ll/c_pT) \tag{3.1}$$

where potential temperature θ is derived from the Rosemount temperature T, fuselage pressure p, and dry air values of the gas constant and specific heat c_p. The latent heat of vaporization L is assumed constant. The equivalent potential temperature (θ_e) is calculated by the method suggested in Bolton (1980) using T, p, r, and the relative humidity. Note that both θ_e and θ_l may be reasonably well approximated by their linear forms (Betts, 1982) for DYCOMS conditions. Wind speed WS and wind direction WD measurements become inaccurate during aircraft turns so the plots are interpolated over those portions. Winds in a spiral sounding then are very questionable.

An additional set of profiles showing the variance of these variables over the height bins is available but are not shown because of their limited usefulness. They can be useful for determining inversion height when it is not apparent from the mean sounding.

3.3 MEAN BOUNDARY LAYER QUANTITIES

Table 3.1 gives values of quantities in the marine boundary layer averaged over the horizontal legs. The $\overline{T}_s$ is radiometric surface temperature, $\overline{T}_{50}$ is air temperature, and $\overline{q_w}$ is total water density. Variables $\overline{T}_{50}$, $\overline{T}_s$, and $\overline{p}_{50}$ are averages from the 50-m legs only. The others are averages over all of the legs within the marine boundary layer.

The mean height of the subsidence inversion z_i is determined from the set of soundings from each flight. In most cases this height also defines the mixed layer depth H. Estimates of z_i have also been obtained by comparing aircraft altitude

at the inversion penetrations during the cloud top legs. The estimates are in good agreement. The individual estimates of z_i may vary by as much as 100 m due to both small-scale and mesoscale variations.

3.4 FLUXES

Fluxes are calculated by the eddy correlation technique. This method relies on the principle of Reynold's decomposition of a time series into its mean and fluctuating components (Panofsky and Dutton, 1984, Chapter 4). The basic flux averaging period for the analysis is a segment of 225 s of the 20-Hz data. This is effectively a line average over about 23 km. The fluctuating component of the time series remains after the mean and linear trend have been subtracted from the original. The vertical eddy flux is then formed by multiplying the value of the fluctuating component at each point by the corresponding value of vertical velocity w and averaging over the segment.

3.4.1 Total Water Eddy Flux

Due to the inability of any single instrument to measure q_v in all conditions (Sec. 2.3) a hybrid time series has been constructed consisting of Lyman-alpha, EG&G, and Rosemount-derived humidities. The Lyman-alpha fluctuating value is used for sub-cloud legs and in cloud-free portions. In the presence of liquid water (deduced from the FSSP activity) q_v is assumed equal to the saturation absolute humidity q_{vs} derived from T and p using the Clausius-Clapeyron relation as approximated by Bolton (1980). However, since the Lyman-alpha is not calibrated exactly with the Rosemount, the combined time series is not continuous when passing in and out of cloud. This calibration switching could be correlated with vertical velocity and contribute a false flux. To minimize this problem, the means of the cloud free and saturated portions are separately adjusted to equal the EG&G-derived mean values for the same portions. The resulting time series is reasonably continuous in and out of cloud allowing an estimate to be made of

$\overline{w'q_v'}$. The total water eddy flux is then $\overline{w'q_w'} = \overline{w'q_v'} + \overline{w'q_l'}$ where the liquid water flux is calculated from the King probe output advanced 0.2 s (Sec. 2.3). Also $\overline{w'\theta_e'}$ is obtained using the q_v time series as described here.

3.4.2 Drizzle Flux

The liquid water mass flux due to gravitational settling relative to the air motion, or drizzle flux, is denoted $\widetilde{wq_l}$. This is calculated from the drop size distributions measured by the FSSP and the PMS 200X optical array probe:

$$\widetilde{wq_l} = \Sigma m_i N_i w_{Ti} \tag{3.2}$$

The sum is over the i size bins of the FSSP for mean diameters 5.7 to 75 μm and the 200X for 75 to 187 μm. The mass of a spherical drop at the bin mean diameter is m_i, w_{T_i} is the terminal velocity, and N_i the number concentration in the bin.

The terminal velocity is approximated (Rogers, 1979) by

$$w_T = -(1.19 \times 10^8\ m^{-1}s^{-1})\ r^2 \qquad r \leq 40\ \mu m \tag{3.3}$$

$$w_T = -(8 \times 10^3\ s^{-1})\ r \qquad 40\ \mu m \leq r \leq 600\ \mu m$$

for drops of mean radius r.

The drop size distributions have been used uncorrected although significant spectral distortions are known to arise in certain conditions (Dye and Baumgardner, 1984). Dead time and coincidence losses in measured concentration will be negligible for the typically low values observed in DYCOMS (Baumgardner et al., 1985; Baumgardner, 1986). Distortion due to response time limitations should also be small since the spectra are relatively narrow and in a band not greatly affected (Baumgardner, 1987). The measured distributions are expected to be accurate to about 15 to 20%.

3.4.3 Flux Profiles

The drizzle and vertical eddy fluxes as functions of normalized height in the MBL are shown in Fig. 3.2a to 3.2h. These are average values for each flight and 90% confidence limits on the mean based on a Student t distribution for flux estimates from each segment at an altitude. The calculation of virtual potential temperature (θ_v) includes liquid water loading.

Under mixed layer conservation assumptions the profiles of $\overline{w'O_3'}$ and $(\overline{w'q_w'} + \widetilde{wq_l})$ should be linear. Temperature flux profiles will not be linear if radiative effects are significant. The idealized flux profile may be fully characterized by specification of an intercept and slope. These coefficients, the projected value of the flux at z_i, and confidence limits on these values are calculated using a standard analysis of variance package (Draper and Smith, 1966). Altitude and segment-flux are input as independent and dependent variables respectively. Figure 3.3 shows an example scatter plot for the O_3 flux and the best fit line. The O_3 flux profile analysis is done in mixing ratio units which are conserved with height (1 ppbv $\simeq$ 2 μg m^{-3} at sea level). Since the flux variability is much higher in the upper marine boundary layer, the best estimate for surface flux is taken from extrapolation of the two lowest levels only. The values of the flux profile coefficients are given in tables in the next two chapters as they are used for analysis.

3.4.4 Surface Fluxes And Stability

Near-surface scalar fluxes, friction velocity u_* and Monin-Obukhov scaling length $-L$ are given in Table 3.2. These are averages from the 50-m flight legs.

3.4.5 Radiative Fluxes

The measured upward ($\uparrow$) and downward ($\downarrow$) components of the SW and LW fluxes have been averaged for each horizontal flight segment. Figure 5.1 shows the

average net LW flux at each normalized altitude from each flight and composite profiles for cloudy and cloud-free cases.

An example set of SW component and net profiles as well as the net LW + SW is shown in Fig. 5.3. Due to inhomogeneities in the cloud cover the standard deviations of the SW fluxes are fairly large and the net profiles from other flights may not be as smooth as the example in Fig. 5.3a. The general features are the same however for all the cloud-capped cases. Flight 8, the clear case, Fig. 5.3b, is radically different. The measured SW fluxes are normalized to a median solar zenith angle for each flight (Ackerman and Cox, 1981). The SW$\downarrow$ fluxes are corrected for the tilt of the aircraft relative to a horizontal surface assuming 10% diffuse above and 90% diffuse radiation below cloud (Kawa, 1986). The UV fluxes (not shown) follow SW very closely at 5 to 6% of the SW irradiance.

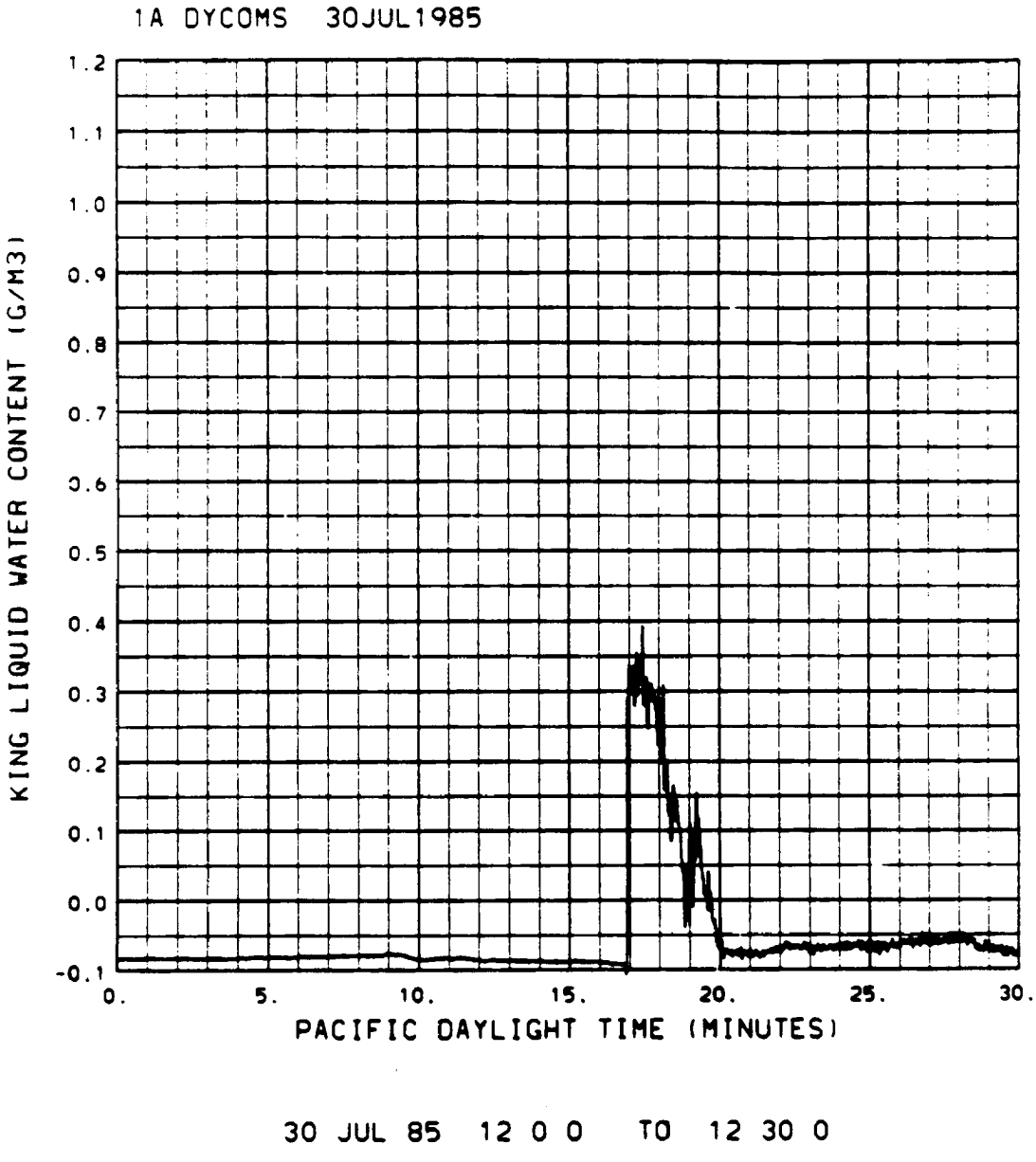

Figure 3.1: Time series of q_l before baselining.

Table 3.1: Mean Boundary Layer Quantities. See text for definition of symbols.

FLIGHT	1	2	3	4	5	6	7	8	9	10
$\overline{T}_{50}$ ($^{\circ}C$)	17.5	16.1	16.1	17.8	17.8	17.1	17.9	17.2	19.2	17.2
$\overline{T}_s$ (°C)	18.5	16.7	18.0	19.0	19.0	17.8	19.3	17.4	20.5	19.1
$\overline{p}_{50}$ (mb)	1012	1012	1011	1013	1011	1012	1007	1014	1013	1013
$\overline{q_w}$ (g m^{-3})	11.4	10.9	11.2	11.0	10.5	9.8	10.6	10.7	11.5	9.6
$\overline{\theta_l}$ (K)	289.6	288.4	288.4	290.0	290.2	289.0	291.4	289.5	291.5	289.3
$\overline{O}_3$ (ppbv)	19.7	25.4	32.7	23.5	24.5	44.3	50.5	25.8	27.4	39.3
$\overline{WS}$ (m s^{-1})	9.8	9.0	5.6	8.8	7.5	4.3	5.4	7.0	7.4	6.3
$\overline{WD}$ (deg)	342	322	321	340	328	276	308	316	357	349
z_i (m)	773	730	588	880	925	917	1380	1034	—	1009

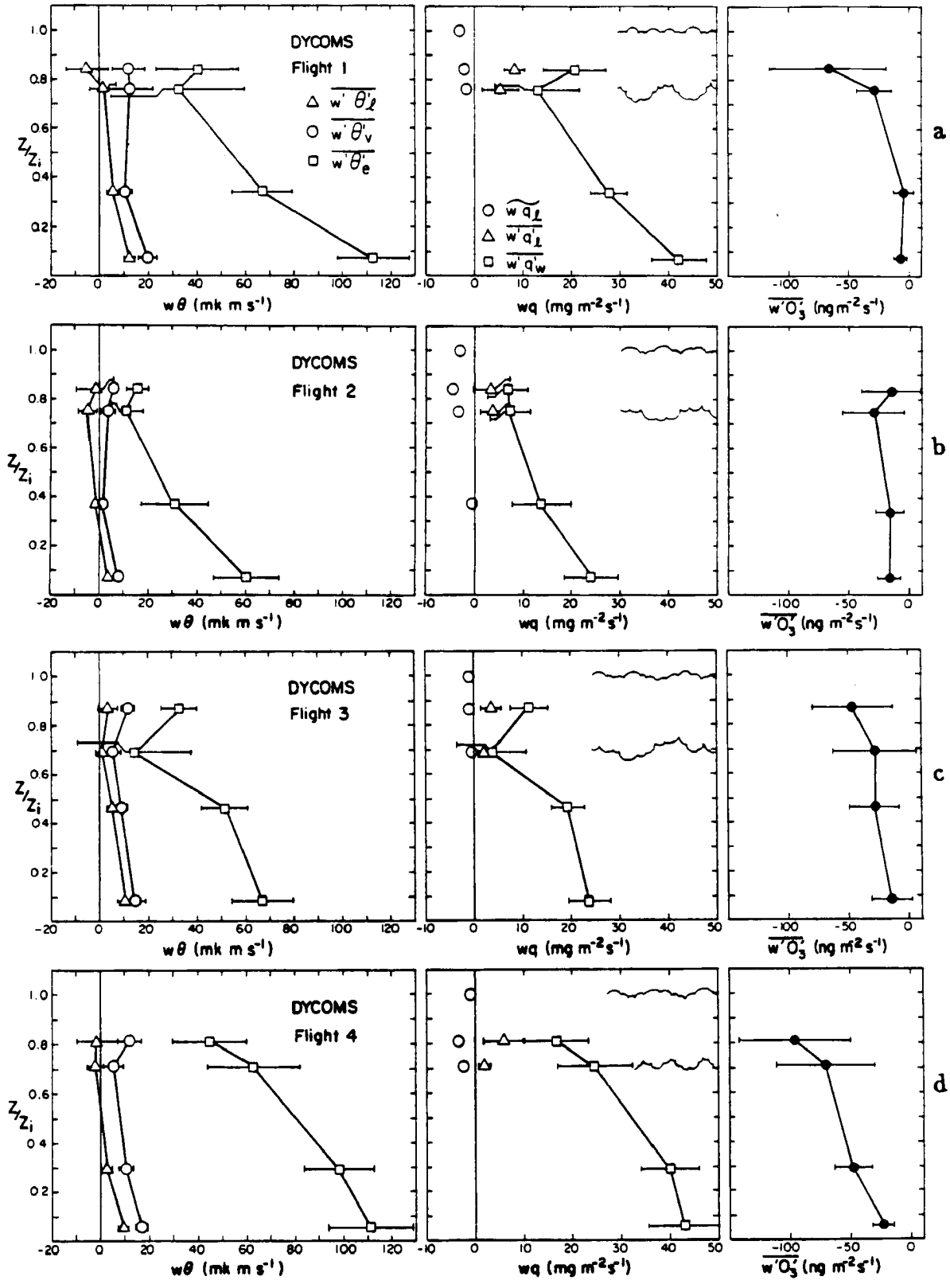

Figure 3.2: Complete set of DYCOMS flux profiles.

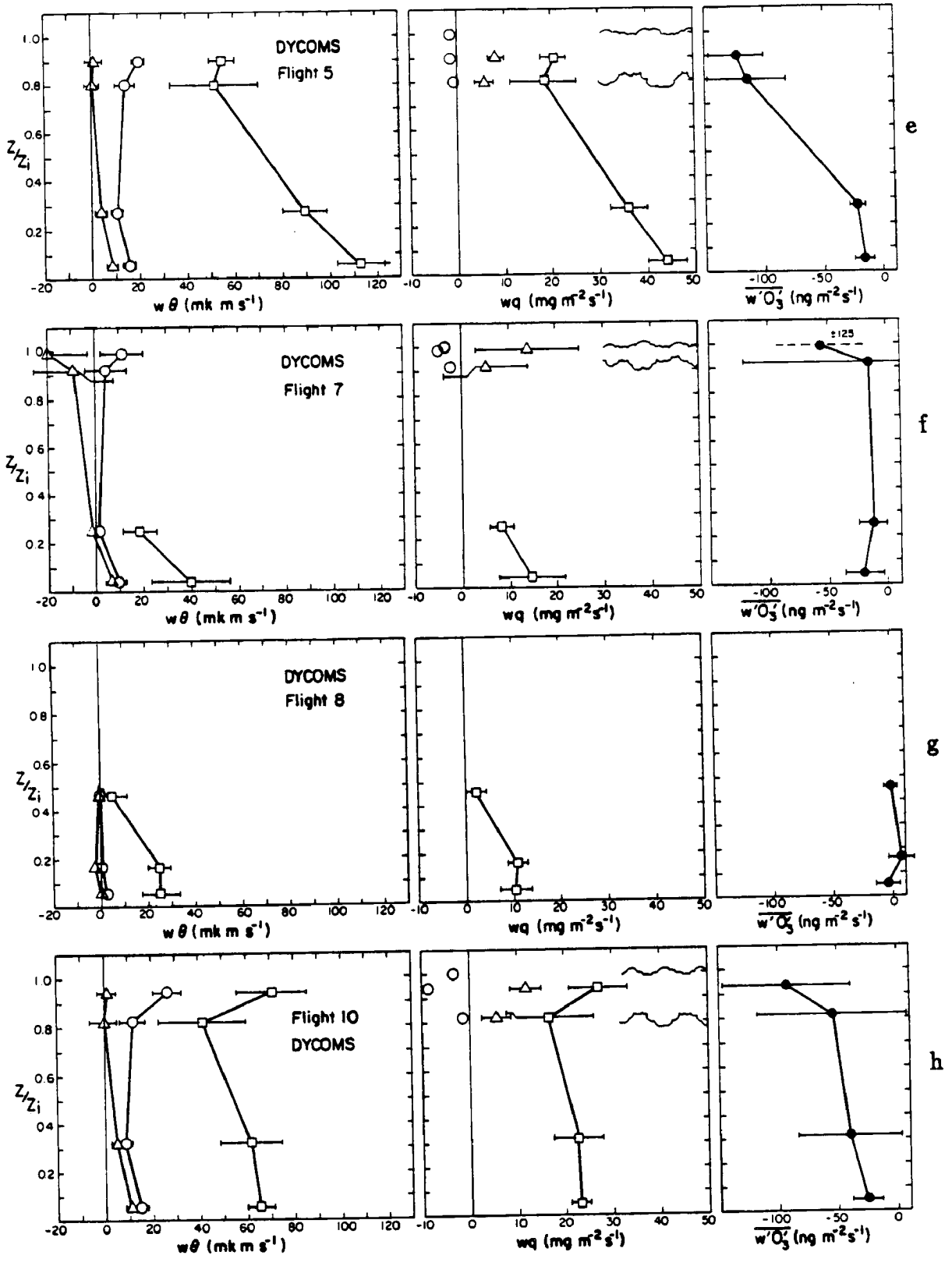

Figure 3.2: (cont.). DYCOMS flux profiles.

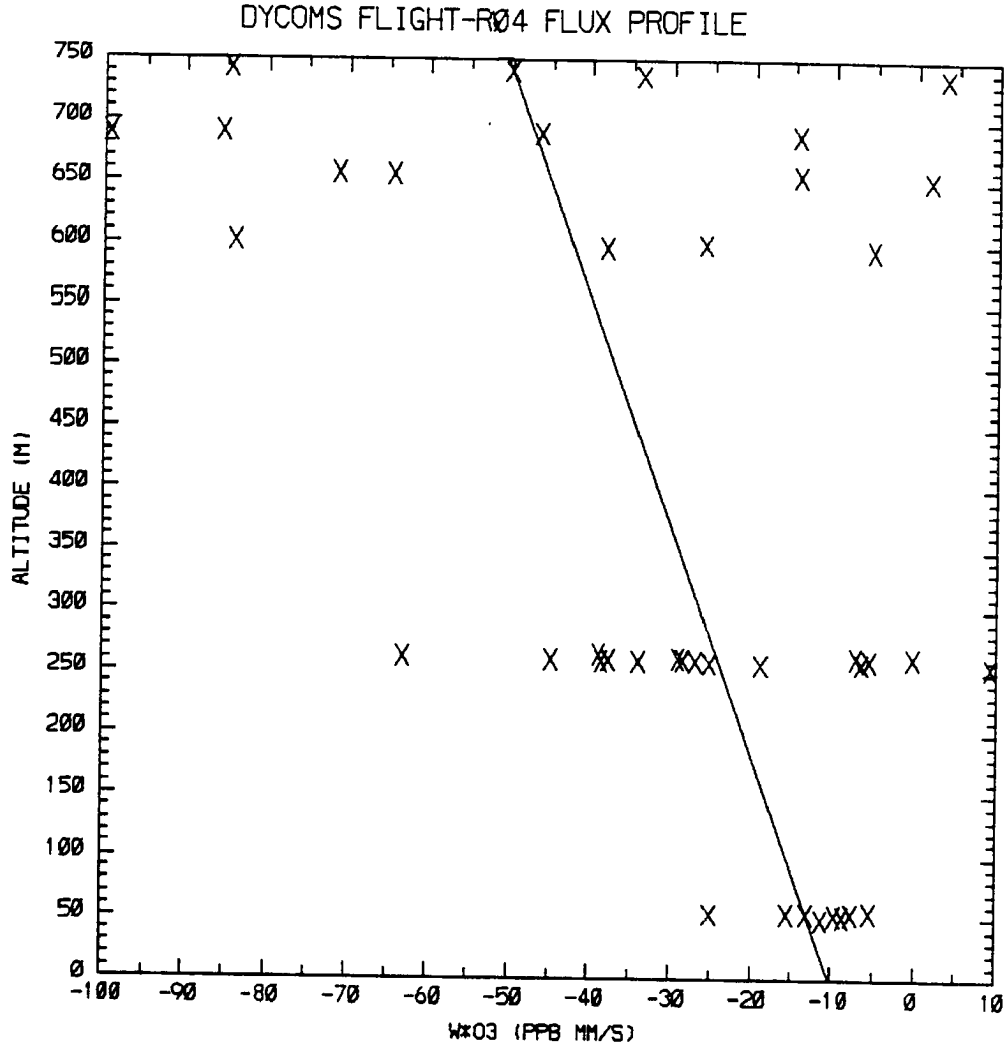

Figure 3.3: Example plot of O_3 flux measurements for each leg segment and the best-fit linear profile.

Table 3.2: Surface layer fluxes. See text for definition of symbols.

FLIGHT NUMBER	1	2	3	4	5	6	7	8	9	10
$\overline{w'\theta'}$ (mK m s^{-1})	12.6	3.9	10.3	10. 1	8.5	4.0	7.1	1.2	11.4	11.2
$\overline{w'q'_v}$ (mg $m^{-2}s^{-1}$)	41.7	24.3	23.6	42.8	43.9	28.5	14.7	10.5	44.1	22.5
$\overline{w'\theta'_v}$ (mK m s^{-1})	19.8	7.9	14.2	17.3	15.8	8.5	8.0	2.9	18.6	15.1
u_* (m s^{-1})	0.31	0.28	0.18	0.30	0.26	0.15	0.14	0.17	0.22	0.19
$-L$ (m)	119	205	36	132	87	38	34	212	52	40

Chapter 4: OZONE BUDGET

Current understanding of the global ozone (O_3) budget generally accepts that three primary processes control tropospheric O_3. These are: (1) a source from exchange of air with the ozone-rich stratosphere, (2) destruction at the earth's surface, and (3) ambient photochemical reactions which may yield either a net sink or source depending on reactant concentrations. The relative importance of these processes and their distribution over the globe and through the depth of the troposphere is, however, largely uncertain. The observational data of DYCOMS can be used within a suitable theoretical framework to address this uncertainty. Many of the results, specific to the eastern North Pacific SC regime, should be applicable to pristine marine areas over the globe including large portions of the Southern Hemisphere.

Recent advances in measurement technology allow calculation of the vertical O_3 flux in turbulent air by eddy correlation of aircraft data (Lenschow et al., 1981). Low level measurements of this type constitute a nearly direct estimate of the surface destruction rate. Combining flux and mean measurements with micrometeorological theory, values are obtained for surface characteristic variables which can be used to improve parameterization of O_3 surface destruction in global models. The measurement set is further used to estimate terms in the O_3 conservation equation and to diagnose the net chemical source/sink in the boundary layer. This is compared to photochemical model predictions for similar background conditions. Finally, the observed O_3 distributions, meteorological flow fields, and inferences for source regions are discussed.

4.1 SURFACE DESTRUCTION

Dry deposition at the surface is a major loss of ambient O_3 and therefore needs to be determined accurately for any simulation of tropospheric O_3 processes. Due to the complexity of the surface chemistry, theoretical determination of the deposition rate to seawater has not been satisfactory (Garland et al., 1980) and empirical methods are required. Several techniques have been employed by a variety of investigators (Aldaz, 1969; Galbally and Roy, 1980; Lenschow et al., 1982). The problem is that the measured deposition rates to ocean vary widely. In general, O_3 deposition to sea surfaces is much less than to terrestrial surfaces, except snow, and has an uncertain dependence on wind speed (Wesely, 1983). But the range of measured values is so great that Levy et al. (1985) concluded that a realistic simulation of surface loss was not possible and chose to use a range of O_3 deposition velocity that varied by a factor of five in their global transport model. Part of this variability is due to measurement artifact and the difference between techniques, and part is natural.

In this section I present measurements of O_3 surface deposition from the DYCOMS project. This represents 5 1/2 hours or about 2000 km of eddy correlation measurements from the aircraft at 50 m above sea level. These are the first available for the SC regime. The values are discussed in terms of mean and variability, and recommendations for use in large-scale models are given.

4.1.1 Method of Calculation

Two parameters that will be discussed as characteristic of the O_3 surface destruction rate are deposition velocity w_d and surface resistance r_s. Thus

$$w_d = \frac{-(\overline{w'O_3'})_o}{\overline{O_3}\ (50\ m)} \tag{4.1}$$

and

$$r_s = w_d^{-1} - r_a \tag{4.2}$$

where r_a is the aerodynamic resistance calculated by the method of Wesely (1983) for smooth surfaces. The surface flux $(\overline{w'O_3'})_o$ is obtained by extrapolating flux values at the two lowest measurement levels to the surface (except Flights 6 and 9 are 50-m means) and $\overline{O_3}$ (50 m) is the mean measured O_3 at the lowest level. Recall that this procedure assumes that no chemical reactions are occuring in the lowest 50 m on a time scale small enough to be comparable to the turbulent mixing time (Fitzjarrald and Lenschow, 1983). The statistical uncertainty in w_d and r_s comes largely from the variation in $\overline{w'O_3'}$ since σ_{O_3} is typically 0.5 ppbv and r_a turns out to be only a small fraction of r_s. The confidence intervals on $(\overline{w'O_3'})_o$ for each flight are 90% intervals based on a Student t distribution of the measured flux values.

4.1.2 Discussion

Values for the surface destruction parameters are given in Table 4.1 along with averages over the entire project. The first thing to note is that most resistance is contributed by the surface. For any case, r_a is less than 5% of the total resistance to O_3 transfer. Negligibility of r_a may sometimes be a useful approximation, valid in moderate winds for slowly depositing species. The second notable feature is the variability of w_d and r_s; values vary from flight to flight by more than a factor of two and the individual estimates are uncertain to more than $\pm 50\%$ at the 90% confidence level. Some of the variability may be understood by examining the flux profiles. For example, the extreme low w_d value for Flight 6 may be due to flux divergence below 50 m. The flux measured at 250 m, though further west along the track, is greater than the 50-m measurement. Extrapolating these values would increase w_d and decrease r_s by at least 10%. The other low w_d extreme, Flight 3, has the largest uncertainty for any 50-m flux in the program.

There is no apparent close correspondence between variations in O_3 deposition rate and the measured and observed conditions during DYCOMS. Based on O_3 solubility in water, r_s should be correlated with T_s, increasing 3% per °C (Garland et al., 1980). This is not supported by the mean data (Table 3.1) and would be a very small signal compared to the observed range. Flight 9, along the T_s gradient, shows this correlation but has the additional complication of decreasing u_*. The correlation between w_d (or $1/r_s$) and u_* (Table 3.2) is not strong but does appear to be significant ($R = 0.65$). Since increasing u_* corresponds to higher $\overline{u}$ and thus increased sea surface roughness, surface area, and sub-surface mixing, resulting increases in w_d or $1/r_s$ are expected. This tendency was reported by Galbally and Roy (1980). No dependence on $\overline{u}$ was detected by Wesely et al. (1981) over lake water however, nor by Lenschow et al. (1982) over ocean. Wesely et al. (1982) observed increasing CO_2 flux with u_* and suggested that coated bubbles mixing to the surface may enhance chemical reactions. The reaction of O_3 with surfactant species has been suggested by Garland et al. (1980) to explain the higher rate of O_3 deposition to natural sea water than that expected from laboratory measurements with prepared solutions. All of this suggests that, while wind speed exerts some control on O_3 surface resistance, some unmonitored condition of the sea state is operating as well, with a similar degree of influence. The DYCOMS measurements indicate that r_s might be best selected as 3000 s m^{-1} for $7 < \overline{u} < 10$ m s^{-1} and 5000 s m^{-1} for $4 < \overline{u} < 7$ m s^{-1}.

In contrast to this line of reasoning, if we assume that the above variability represents random variation of the same phenomenon with a normal distribution, the mean values of w_d and r_s for the program (Table 4.1) are accurate to about ±20% at the 90% confidence level. The program-mean $r_s = 4190$ s m^{-1} is about four times higher than Galbally and Roy (1980) proposed for ocean based on a compilation of previous measurements. It is also about twice that Lenschow et al. (1982) found for rather polluted conditions over the Gulf of Mexico and in high winds (15 to 18 m s^{-1}) over the North Pacific. The mean surface flux agrees

closely with box measurements of Aldaz (1969) however. In view of this it appears that the r_s estimate of Galbally and Roy (1980) should be revised upward but that caution and further study are needed to extend these observations to estimates of the O_3 surface sink over ocean areas such as the tropics or Southern Hemisphere.

4.2 BOUNDARY LAYER PHOTOCHEMISTRY

Photochemical processes have been proposed as a significant influence on O_3 in the unpolluted troposphere, largely on the basis of expected reactant concentrations (Crutzen, 1973) and the well-documented production of O_3 in polluted atmospheres (Leighton, 1961). Photochemistry has been proposed to explain several observed features of O_3 distributions (Chameides and Walker, 1973; Fishman et al., 1979; Liu et al., 1983). The impact of photochemistry on the global O_3 budget has been studied with numerical models of photochemical reactions (Fishman and Crutzen, 1977; Liu et al., 1980; Chameides and Tan, 1981; Logan et al., 1981). The problem, however, is that measurement of O_3 photochemical destruction and production in situ is very difficult and experimental verification of model predictions is lacking (Fishman, 1985). Lenschow et al. (1981, 1982), using a procedure very similar to the one used here, obtained experimental estimates of O_3 production over Colorado rangeland and the Gulf of Mexico in air characteristic of moderate anthropogenic influence. Kawa (1985) found a much greater production over Texas forest when under advection from the Houston urban plume. In this section I address the question of estimating O_3 photochemical processes in the unpolluted remote marine boundary layer using DYCOMS measurements.

4.2.1 Diagnostic Model

This section details the theoretical framework within which the measured quantities are used to diagnose the net chemical source/sink of O_3 in the planetary boundary layer. Starting with the conservation relation for a vertically conserved

scalar, $ds/dt = Q_s$, and performing Reynold's averaging, a general mixed-layer budget equation can be written (Lenschow et al., 1981) as

$$\frac{\partial \overline{s}}{\partial t} + \overline{u}\,\frac{\partial \overline{s}}{\partial x} + \frac{\partial \overline{w's'}}{\partial z} = Q_s \tag{4.3}$$

where Q_s represents the mean internal sources and sinks of the scalar s. This assumes anelastic continuity, horizontal homogeneity of flux terms, negligible mean vertical advection, and a coordinate system oriented along the direction of the mean wind $\overline{u}$. In a frame of reference following the aircraft motion (denoted D/Dt) we see, with the aid of Fig. 4.1, that the change in the mean quantity equals the total derivative plus the change due to the relative motion in the large scale gradient, $D\overline{s}/Dt = d\overline{s}/dt + (\partial \overline{s}/\partial n)(Dn/Dt)$. The budget equation, specifically for O_3, now becomes

$$\frac{D\overline{O_3}}{Dt} - \frac{\partial \overline{O_3}}{\partial n}\,\frac{Dn}{Dt} + \frac{\partial \overline{w'O_3'}}{\partial z} = Q_{O_3} \tag{4.4}$$

where Dn/Dt represents the aircraft motion relative to the mean horizontal wind and $\partial \overline{O_3}/\partial n$ is the gradient in that direction. Terms on the left hand side of (4.4) are evaluated from aircraft measurements and Q_{O_3} is calculated as the residual.

The $D\overline{O_3}/Dt$ term is the vertical average of the differences measured at each level between two sets of legs (at points A and B in Fig. 4.1). The flux divergence term is obtained from a linear regression of the flux measurements versus altitude. The relative advection term is approximated from the finite differences δx and δy as shown in Fig. 4.1 and the difference in time δt between measurement sets A and B. The gradient $\partial \overline{O_3}/\partial y$ is directly measured in all flights but $\partial \overline{O_3}/\partial x$ is available only for Flights 7 through 10. The x-component of mean advection is not included in the budgets for Flights 1 to 5 but is in the uncertainty estimates. The $\overline{u}$ is averaged over all flight legs in the boundary layer.

During planning for DYCOMS the aircraft flight pattern was intended to be advected as nearly as possible with the mean wind such that $Ds/Dt = ds/dt$

and gradient terms would not be calculated. The horizontal O_3 gradients were expected to be small enough that deviations from an advected flight path would not be significant. In the field, however, the O_3 gradients were found to be significant in some cases, belying the apparent horizontal homogeneity of the SC. Combined with deviations in the intended path due to outside turns (to avoid sampling aircraft exhaust), difficulty determining the exact crosswind direction from the initial sounding, and different winds above the boundary layer, the gradient terms became relatively large. Unfortunately, the uncertainty in calculating these terms contributes a large amount of the uncertainty in the diagnosed value of Q_{O_3}.

4.2.2 Results

Results from the eight DYCOMS budget flights are shown in Table 4.2. The most striking feature of this table is that in the long-term ($\sim$ 1 month) mean the total time derivative, sum of the first two terms, is zero and the vertical flux divergence is balanced by net chemical destruction. Closer examination of the Q_{O_3} terms reveals that the magnitude of Flight 7 is significantly larger than any others and may be an anomaly pulling the average too low. There is possible justification for disregarding Flight 7 since the boundary-layer soundings are decidedly not well-mixed and thus may violate assumptions regarding homogeneity. If Flight 7 is not included in the average, Q_{O_3} is about -0.02 ng m^{-3}s^{-1} and part of the average flux divergence balances a small increase with time.

The confidence intervals on the individual case values for $D\overline{O_3}/Dt$ are the uncertainties in the mean at the 90% confidence level based on a Student t distribution of the O_3 change with time at each altitude. Flight 8 is larger because fewer legs were flown. The confidence intervals on $(\partial\overline{O_3}/\partial n)$ (Dn/Dt) are determined from the 90% confidence interval on the gradient estimates plus $|\ (\delta x/\delta t)(\partial O_3/\partial y)\ |$ where $\partial O_3/\partial y$ is used because $\partial O_3/\partial x$ is not available. The confidence limits on $\partial\overline{w'O_3'}/\partial z$ are from a standard analysis of variance calculation on the linear regression at the 90% level (Draper and Smith, 1966). The interval

on Q_{O_3} is the sum of intervals on the three measured terms which is clearly a worst-case interpretation. The confidence intervals on entries in the Average column are 90% values based on the estimates for each flight entry.

Looking at individual terms we see that in every case the relative advection term tends to balance the time change, in most cases rather closely, even though the largest uncertainties reside in the advection terms. This lends confidence to the assertion that O_3 is near steady state in the SC. The flux divergence terms are all less than zero and fairly consistent in magnitude even though the uncertainty for any given case is comparable to the mean divergence. Taken with the above, this would indicate that the photochemistry is near steady state on a time scale from day to day. Whether the fluctuations in Q_{O_3} from flight to flight are significant is questionable given the measurement uncertainties but discussion pointing to their reliability is included in the next section.

4.2.3 Discussion

Detection of an O_3 sink in the marine boundary layer by this method is an important confirmation of photochemical model predictions. Moreover, the average magnitude of the destruction rate (0.02 to 0.07 ng $m^{-3}s^{-1}$ $\simeq$ 2 to 9 x 10^5 molec $cm^{-3}s^{-1}$) agrees closely with predictions for the daytime marine boundary layer with low background NO (Liu et al., 1983; Logan et al., 1981; Thompson and Cicerone, 1982). Further understanding of the O_3 budgets may be gained by looking at details of the photochemistry.

Very briefly, the O_3 photochemistry relevant to the remote marine boundary layer is the following. O_3 is consumed through ultraviolet photolysis and the occasional collision with a water molecule.

$$O_3 + h\upsilon(< 320\ nm) \rightarrow O_2 + O(^1D) \qquad (R1)$$

$$O(^1D) + H_2O \rightarrow 2OH \qquad (R2)$$

The OH will oxidize a variety of hydrocarbons and CO producing HO_2, CH_3O_2 or RO_2, any of which react with NO to regenerate OH. For example

$$HO_2 + NO \rightarrow NO_2 + OH \qquad (R3)$$

which will generate O_3 during daytime.

$$NO_2 + h\upsilon(< 420 \text{ nm}) \rightarrow NO + O \qquad (R4)$$

$$O + O_2 + M \rightarrow O_3 + M \qquad (R5)$$

If NO is low, however, then O_3 destruction may occur catalytically.

$$O_3 + HO_2 \rightarrow OH + 2O_2 \qquad (R6)$$

$$O_3 + OH \rightarrow HO_2 + O_2 \qquad (R7)$$

The strong dependence of net O_3 production/destruction on NO is a feature common to all models.

The equations point out the dependence of O_3 chemistry on sunlight. This is especially important to DYCOMS because of the influence of the SC. The cloud albedo for SW and UV is 40 to 50%, so from (R1) the O_3 destruction rate for the cloud-topped boundary layer should be less than for clear skies, all else being equal. The magnitude of this effect is predicted to be a 30 to 50% reduction in net O_3 destruction (Thompson, 1984; Chameides et al., 1987). Therefore, we would expect the mean destruction for DYCOMS to be small compared to the clear sky models mentioned above, which it is if Flight 7 is excluded. This is not clearly observable in the case to case variation, however. Flight 8, the cloud-free case,

and Flight 10, the morning case, have Q_{O_3} near the mean. Possibly, variations of NO in the boundary layer create variations in Q_{O_3} large enough to obscure the effect of clouds. The range of Q_{O_3} (excluding Flight 7) in DYCOMS is similar to that predicted for the marine boundary layer by Chameides et al. (1987) based on observed NO and O_3.

The sink for Flight 7 appears anomalously large, but the strong dependence of Q_{O_3} on the O_3 concentration (R1, R6, R7) and the fact that $\overline{O_3}$ is highest of any flight means that a larger sink in this case may be predictable. For Flight 3 the observed O_3 production may well be the result of higher NO due to the influence of continental air advecting from California. The typical DYCOMS trajectory shows no influence of continentality (Lenschow et al., 1988a) but Flight 3 is closer to the coast (Fig. 2.1) and the 300 K isentrope goes back to 1 km altitude approximately over Santa Barbara two days earlier.

So although the uncertainty in Q_{O_3} for any case is large, there is indication that the variation between them is meaningful. A most interesting experiment would be to include measurement of NO_x with this method. This was attempted in DYCOMS but the instrument failed. As far as using DYCOMS measurements to estimate Q_{O_3} for other remote marine regions, these results indicate that daytime O_3 destruction is in the range -0.02 ng $m^{-3}s^{-1}$ to -0.07 ng $m^{-3}s^{-1}$ or possibly lower for clear regions. This agrees with the findings of Levy et al. (1985) who required such a photochemical sink in the tropical and subtropical boundary layer in order to achieve a realistic simulation of O_3 transport.

4.3 LOCAL MEAN DISTRIBUTIONS

Although the O_3 measurements of DYCOMS are specific to a rather small area and shallow altitude range, they are extremely high resolution and can contribute to our understanding of the global O_3 distribution, particularly in terms of variability. In general, DYCOMS O_3 distributions conform to established climatology for remote regions: a tropical minimum increasing toward either

pole, low concentration in the boundary layer, an increase with height in the free troposphere and a definite seasonal cycle (Fabian and Pruchniewicz, 1977; Chatfield and Harrison, 1977; Seiler and Fishman, 1981; Logan, 1985; Piotrowicz et al., 1986). The most striking feature of the DYCOMS O_3 data is the large degree of variability, especially in the vertical profiles above the boundary layer. Knowledge and understanding of this variability are important for interpreting O_3 datasets, comparing model predictions to measurements, and possibly for simulating non-linear interactions among chemical species.

Within the marine boundary layer, DYCOMS O_3 is in the 20 to 30 ppbv range and vertically well-mixed (Figs. A.1 to A.24). The only notable exceptions are Flights 6 and 7 which have about twice the DYCOMS median O_3 (Table 3.1). Flight 7 also shows evidence of a layered, unmixed boundary layer. The meteorology on these days was perturbed by the influence of a tropical storm (Section 2.2) and the higher O_3 is probably related to increased entrainment of free tropospheric air (Section 5.3 below). None of the DYCOMS profiles show an O_3 gradient across cloud base supporting the contention that O_3 is a passive scalar in cloud processes (Pearson and Weaver, 1988) as well as confirming that the measurement technique is not sensitive to liquid water. There are no surface layer vertical gradients of the type observed by Fishman et al. (1987) and attributed by them to a strong surface sink. In view of the DYCOMS soundings and the discussion of sinks in the previous two sections, I suspect that the gradients of Fishman et al. (1987) over ocean are partially horizontal ones, interpreted as vertical along the aircraft slant path. The importance of horizontal gradients in the boundary layer to the budget analysis was mentioned in the previous section. DYCOMS O_3 gradients have a typical leg-average value of 0.02 ppbv km^{-1} in no preferred direction and a maximum of 0.07 ppbv km^{-1}. Larger gradients on a smaller scale were also observed. The boundary layer horizontal O_3 gradients appear to be in response to entrainment of O_3 layers from above. In all cases

except Flight 6, $\overline{O_3}$ is higher above the boundary layer than within, as expected with a low level sink.

The strongly layered nature of O_3 vertical distributions has been observed previously and associated with stratospheric influx (Routhier et al., 1980). Lenschow (1982) has demonstrated however, that a purely meteorological explanation of extremely thin layers is not sufficient. Some lamina of DYCOMS, for example Flights 4 and 5, (Figs A.8a, A.9b, A.10a, A.11b) are distinguishable in soundings 4 1/2 hours and 80 km apart. High O_3 values are often interspersed vertically with low concentrations typical of the boundary layer and the gradients can become almost like step-function changes (e.g. Fig. A.16). Interestingly, the November profiles of Fishman et al. (1987, Figs. 3 and 5) in the same general area show relatively little O_3 variation with height. The origin of these layers and the mechanism for maintaining the extreme gradients is not clear. Direct injection from the stratosphere (Danielsen and Mohnen, 1977), photochemical production in aged continental air (Fishman and Seiler, 1983), production enhanced by lightning-generated and/or entrained stratospheric NO (Chameides et al., 1987) have been proposed to explain high O_3 concentrations in the free troposphere. A typical DYCOMS trajectory (Lenschow et al., 1988a) traces air back to about 500 mb in the Gulf of Alaska six days previously. It was possibly involved in a cyclonic disturbance at that time. Continental influence can be ruled out for at least eight days and probably longer. In general the O_3 layers are anticorrelated with water vapor fluctuations (e.g. Fig. A.7) supporting an upper tropospheric or stratospheric O_3 source. Direct infusion versus production in the upper troposphere cannot be distinguished from this information. If production is important though, it must be completed by the time parcels subside into the boundary layer, as we have seen from the previous section.

Other advection scenarios appear as well. During Flight 6 a layer of characteristically tropical air is seen just above the boundary layer (Fig. A.13). This moist layer, about 500 m deep, has the lowest O_3 and highest θ_e of any during

the project. It appears to have been advected from the tropical disturbance to the southwest in an elevated wind jet.

Whatever their origin, the O_3 layers can have a significant effect on near-surface concentrations. Figure 4.2 shows the increase in O_3 in the boundary layer along a strong gradient in O_3 above. Downward O_3 flux also increases in this direction. The layering observed in O_3 may also lead to problems interpreting measurements of other chemical species for which a significant averaging time is required. For example, the change in concentration of a chemical species across the inversion may be required to close its budget. If this species is correlated with O_3 and measurement of it requires a leg-integrated sample (~15 min) the measured concentration above the boundary layer will be highly dependent on location within the vertical gradient and probably not representative of cloud top conditions.

4.4 CONCLUDING DISCUSSION

I have made an experimental determination of several aspects of the global O_3 budget. The rate of O_3 destruction at the ocean surface has been measured by a nearly direct technique. A significantly higher mean r_s than most previous estimates is found. A time constant for an exponential decrease in boundary layer O_3 due to surface deposition can be estimated from $\tau_o = \overline{z_i}/\overline{w_d} \simeq 40$ days. We have also seen that deposition rates may vary by as much as a factor of two between cases, in spite of apparently similar sea surface states. Extension of these measured rates to other ocean areas should therefore be done cautiously and more experimentation should be done to determine the reasons for variation in O_3 deposition.

The aircraft measurements have been used to estimate terms in the O_3 conservation budget. The results show that, in the average, O_3 in the SC boundary layer is near steady state and that a small photochemical O_3 sink is present. The time constant for destruction by this sink is estimated as $\tau_p = -\overline{O_3}/\overline{Q_{O_3}} \simeq 10$

to 32 days. This sink is at least comparable to and possibly greater than the estimated surface sink. This is an important validation of modeling results. Given the relative uncertainties, it is not known if case-to-case variations in the O_3 photochemistry are significant. Further studies of this kind, augmented by sampling other species, are required to more quantitatively evaluate this apparently important process.

Finally, the high resolution O_3 profiles from DYCOMS have been presented as a contribution to global O_3 climatology and its spatial variation. The observed O_3 layering can affect concentrations at the surface and provides a caution for interpreting any one-dimensional O_3 samples (e.g. Gregory et al., 1984). Clearly, a conceptual model like Fig. 4.3 (from Schubert et al., 1976) is not adequate to describe the general circulation of O_3 in the SC regime. Continued study of O_3 lamina while integrating meteorology, tracers, and chemistry can lead to a more complete model of O_3 circulation including the relative importance of stratospheric flux.

Table 4.1: Ozone Surface Deposition

FLIGHT NUMBER	1	2	3	4	5	6	7	8	9	10	AVE
$[\overline{w'O_3'}]_0$ (ng m^{-2}s^{-1})	−7.7 ±5.4	−17.7 ±9.6	−10.8 ±16.9	−17.5 ±8.2	−15.6 ±7.8	−13.5 ±6.2	−21.0 ±16.3	−10.0 ±10.1	−16.4 ±13.1	−23.8 ±12.4	−15.4
$\overline{O_3}$ (μg m^{-3})	39.3	51.6	66.4	47.0	49.0	89.3	101.1	53.6	51.1	77.5	62.6
w_d (mm s^{-1})	0.20	0.34	0.16	0.37	0.32	0.15	0.21	0.19	0.32	0.31	0.26 ±0.05
r_a (s m^{-1})	94	107	146	98	110	167	177	171	121	139	133
r_s (s m^{-1})	5010	2800	6020	2580	3030	6460	4640	5200	2990	3120	4190 ±840

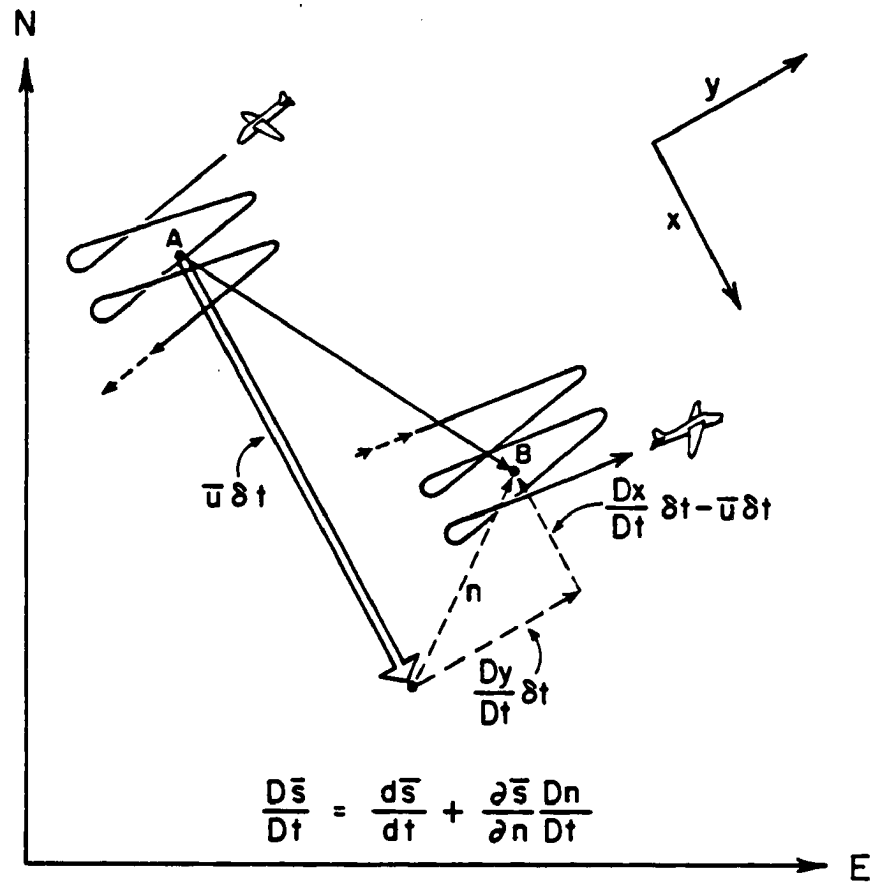

Figure 4.1: Schematic of typical DYCOMS crosswind flight pattern and the difference between Lagrangian and aircraft time derivatives. Points A and B are loci denoting an average position for each of the leg sets. Segment n is the difference in position between the aircraft and a parcel advected by $\bar{u}$.

Table 4.2: Ozone Budgets (ng m^{-3} s^{-1})

FLIGHT NUMBER	1	2	3	4	5	7	8	10	AVE
$D\overline{O_3}/Dt$	0.50	−0.18	0.21	−0.36	0.02	−0.50	−0.65	−0.08	−0.13
	±0.09	±0.06	±0.08	±0.07	±0.02	±0.13	±0.31	±0.14	—
$-(\partial\overline{O_3}/\partial n)(Dn/Dt)$	−0.51	0.24	−0.02	0.51	−0.04	0.14	0.62	0.09	0.13
	±0.10	±0.58	±0.20	±0.35	±0.02	±0.09	±0.30	±0.28	—
$\partial\overline{w'O_3'}/\partial z$	−0.09	−0.01	−0.07	−0.10	−0.17	−0.03	0.0	−0.07	−0.07
	±0.05	±0.05	±0.09	±0.06	±0.03	±0.07	±0.05	±0.08	—
Q_{O_3}	−0.10	0.05	0.12	0.05	−0.19	−0.39	−0.03	−0.06	−0.07
	±0.24	±0.69	±0.37	±0.48	±0.07	±0.29	±0.66	±0.50	±0.11

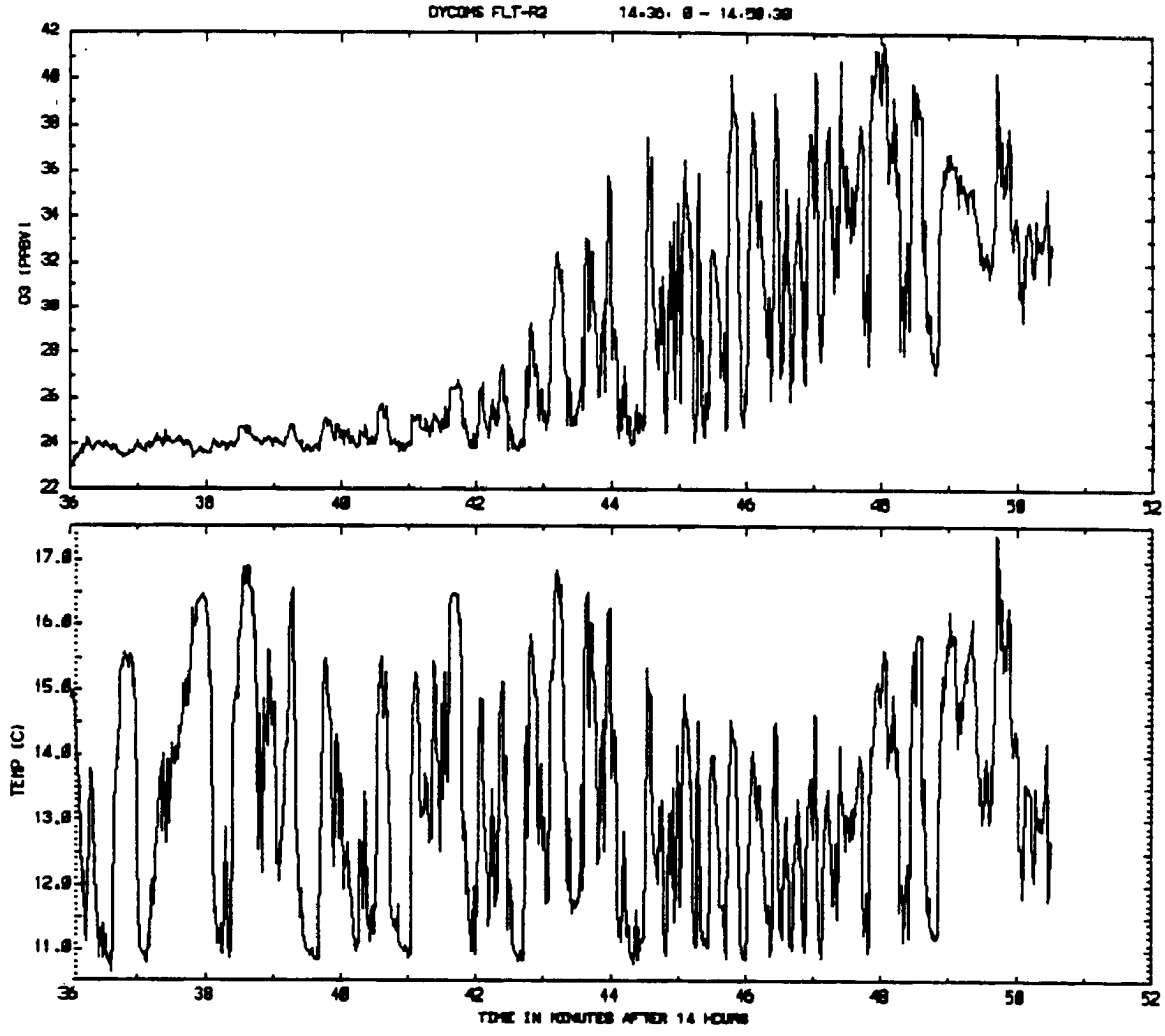

Figure 4.2: Time series from cloud-top leg flown such that aircraft was in cloud turrets about half of the time.

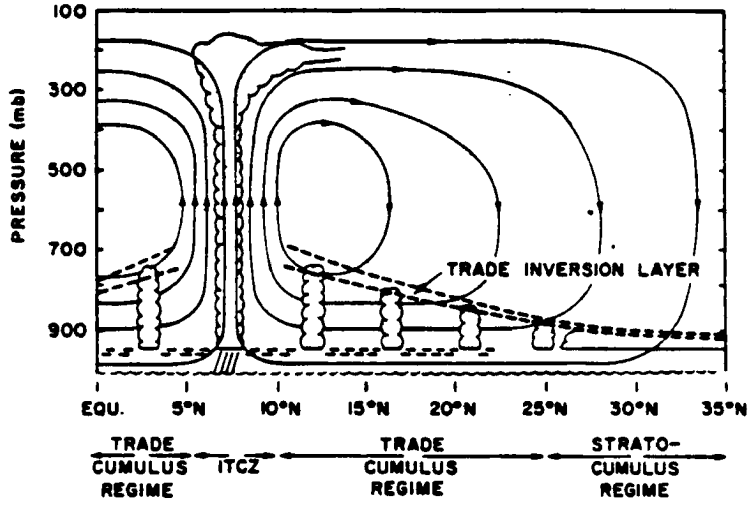

Figure 4.3: Schematic cross section from San Francisco to the Hawaiian Islands to the Marshall Islands. Three regimes are shown: the stratocumulus regime and the trade cumuous regime make up the broad descending branch of the Hadley circulation; the cumulonimbus regime, or ITCZ, makes up the narrow ascending branch of the Hadley circulation. From Schubert et al. (1976).

Chapter 5: DYNAMICS AND THERMODYNAMICS

Stratocumulus cloud layers play an important role in the earth's radiation balance and hence climate. They may likely provide a feedback mechanism for climate perturbations. In order to assess this role it would be desirable to accurately include SC formation, maintenance, and dissipation processes in general circulation model climate studies. Several questions remain before the dynamics and thermodynamics of the regime are understood well enough to do this however. SC have been widely studied through numerical models and, to a lesser extent, through empirical analysis. The essential processes have been identified as surface fluxes, latent heat release, radiative flux divergence, subsidence to form a capping inversion, and entrainment. Wind shear, drizzle, and other factors are important in certain cases. Randall et al. (1984) have identified a number of as yet unresolved issues that are amendable to observational study. Several of these, as well as a number of other problems, can be addressed using the DYCOMS dataset.

In this chapter DYCOMS measurements are used in several applications of theoretical conservation relationships. We begin with a background discussion of the problems that are the focus of this chapter. A descriptive analysis of the local mean conditions is provided to establish the place of this experiment in SC climatology. Measurement of entrainment into the SC-topped boundary layer is demonstrated using a new method based on O_3 conservation. These measurements are compared along with previous estimates in a discussion of entrainment dynamics. The measured components of the layer thermodynamic energy budgets are presented including turbulent fluxes, radiative flux divergence,

and mean transport. These are used to address the questions of the distribution of longwave (LW) cooling, the importance of shortwave (SW) heating, drizzle, and mixed-layer assumptions.

5.1 BACKGROUND

The mixed layer model (Lilly, 1968) is a very useful approximation for simulating SC processes, one which has yielded generally good results. The validity of this approach is supported by large eddy simulation (LES) (Deardorff, 1980a; Moeng, 1986) and some observations (Hanson, 1984; Albrecht et al., 1985). However, based on a one-dimensional (1-D) turbulence closure model, Duynkerke and Driedonks (1987) conclude that it is an oversimplification and obervational studies by Brost et al. (1982a,b), Nicholls (1984), and Nicholls and Leighton (1986) show mixed layer assumptions are not justified in all cases. In spite of these, the mixed layer model is a good tool for understanding SC and further investigation of its parameterizations is warranted.

A key requirement of mixed layer models is an assumption regarding entrainment rate at the layer top. From theoretical considerations, the entrainment energy is usually obtained from buoyant production in the turbulence kinetic energy (TKE) balance within the mixed layer. Various forms of parameterization have been tested but no concensus has been reached (Schubert, 1976; Deardorff, 1976a; Stage and Businger, 1981a,b). Comparison with observations by Nicholls and Turton (1986) indicates the models generally underestimate measured values. Brost et al. (1982b) conclude wind shear can be important and Deardorff (1980a) proposed that entrainment velocity (w_e) depends on the Richardson number at cloud top. Moeng (1987) found neither of the usual partitioning closures (Randall, 1984) are satisfactory.

Closely related to entrainment closure is the issue of how radiative flux divergence is distributed between the inversion and mixed layers (Deardorff, 1981). Lilly's (1968) original model specified all LW cooling within the thin inversion

layer, not contributing to the mixed layer energetics. Deardorff (1976) argued that some LW divergence should occur within the mixed layer, generating turbulence and cooling the boundary layer directly. Schubert et al. (1979a), Randall (1980), and Fravalo et al. (1981) found that model entrainment rate and mixed layer structure are quite sensitive to this distribution. The occurence of most LW cooling above the mixed layer is supported by the observational studies of Brost et al. (1982b) and Rogers and Telford (1986) as well as LES modeling (Deardorff, 1980a; Moeng, 1987). The contrasting view, that LW divergence occurs largely within the area-averaged mixed layer, is supported by 1-D second-order closure modeling (Chen and Cotton, 1987) and observational analyses of Albrecht et al. (1985), Slingo et al. (1982), Nicholls (1984), and Nicholls and Leighton (1986). Almost all of these studies agree that this problem needs further investigation. The effect of SW absorption in cloud is not included in many SC models but it does appear to be an important component (Fravalo et al., 1981; Nicholls, 1984; Chen and Cotton, 1987).

Further information toward resolution of these questions as well as questions regarding the importance of drizzle and the dissipation/reformation cycle will be contributed by analysis of the DYCOMS data.

5.2 LOCAL MEAN CONDITIONS

The DYCOMS typical (Flights 1-5, 10) mean profile shows a boundary layer that is vertically well-mixed in q_w, θ_l, and O_3 about 600 to 1000 m deep. Winds are generally well-mixed but somewhat more variable. The sea surface temperature (SST) distribution over the flight locations (Fig. 2.1) matches SST climatology (Fig. 2.3). With northerly winds and the observation that $T_s > T_{50}$ (Table 3.1), these cases are all characteristic of boundary layer flow over increasingly warmer surface. The cloud layer is typically 150 to 300 m deep with q_l increasing nearly linearly from cloud base to near cloud top. The liquid water content is relatively low: $\overline{q_l}$ (top) <0.5 g m^{-3} for any flight. Droplet spectra indicate that

the vertical q_l gradient is largely due to an increase in drop size and much less to an increase in number. Significant horizontal inhomogeneities in the cloud were observed in most flights including small holes, roll structures, and clear areas. No penetrating convection was observed. Above the boundary layer, large variations in scalar distributions are found but in every sounding, except Flights 6 and 9, the decrease in q_v is large enough that $\Delta\overline{\theta_e} < 0$ at cloud top. The $\Delta\theta_l$ is 5 to 10 K. Wind speed generally decreases upward across the boundary layer top but shear does not appear large.

Flights 6 through 9 are not typical cloud-topped cases. Flight 6 sampled in a scattered cloud region which shows advection of tropical air above the boundary layer. Strong positive wind shear is present in this case. Flight 7 is the only cloud-topped case that is not well-mixed. Compared to typical cases, the inversion is higher and the cloud more variable, even showing multiple layers in places. Horizontal inhomogeneity is large and a more cellular structure of the clouds is observed. Some of these clouds have the highest q_l measured during the program. Flight 8 is entirely free of low level cloud. The inversion is not as sharp and there is a significant surface layer moisture gradient. Wind shear also is more pronounced. While the bulk of the boundary layer is nearly well-mixed and only slightly stable, condensation is not present. Flight 9 samples across the boundary between clear and cloudy regions and shows a complicated series of soundings. Flux profiles and budgets are not constructed for Flights 6 and 9 due to the flight architecture.

5.3 ENTRAINMENT

5.3.1 Method of Calculation

The entrainment relationship is derived (Lilly, 1968) by integrating the conservation equation (4.3) across a thin layer at the mixed layer capping inversion. For an arbitrary scalar s

$$\left(\frac{\partial H}{\partial t} + \overline{u}\frac{\partial H}{\partial x} - w_H\right) \Delta\overline{s} + (\overline{w's'})_H = \int_{H-}^{H+} \overline{Q}_s \, dz \qquad (5.1)$$

where H is the height of the mean inversion, w_H the mean vertical velocity at H, $\Delta\overline{s}$ the change or "jump" in s across the layer, $(\overline{w's'})_H$ is the turbulent flux of s at H, and Q_s is the source/sink term which is integrated across the thin layer from below to above H. I have retained the horizontal advection term for the case of an inversion sloping along the direction of the mean wind $\overline{u}$. This assumes that the turbulent flux above H is zero and wind shear is insignificant. Denoting the first term in parentheses as the entrainment velocity w_e and applying it to O_3 we have

$$w_e = \frac{-(\overline{w'O_3'})_H}{\Delta\overline{O}_3} \qquad (5.2)$$

since the O_3 source/sink vanishes as the layer thickness goes toward zero.

Terms on the right of (5.2) are obtained from aircraft measurements with an estimate for w_e as the result. The $(\overline{w'O_3'})_H$ is from extrapolation of a linear regression of the flux measurements to height H, and $\Delta\overline{O}_3$ is obtained from the soundings and legs at cloud top. Since the soundings show that $\Delta\overline{O}_3$ is not always a step function, some assumption of a finite mixing depth is made to get $\Delta\overline{O}_3$. The $\Delta\overline{O}_3$ estimates have been confirmed with mixing line analysis (Betts, 1982) by Weaver (1987). The 90% confidence limits on $(\overline{w'O_3'})_H$ are determined by a standard analysis of variance program on the flux profile. Standard deviations of the $\Delta\overline{O}_3$ estimates, σ_Δ, are from the individual point evaluations.

5.3.2 Discussion

The ozone-derived entrainment measurements are shown in Table 5.1 along with the mean inversion heights. For the cloud cases w_e ranges from 1 to 5 mm s^{-1} and averages about 3 mm s^{-1}. The clear case, Flight 8, has no measurable entrainment. The uncertainties in each case are large. The episodic nature of

entrainment flux and large cloud-top O_3 gradients make good statistical estimates hard to get. I estimate that the w_e's are accurate to at best 50% of the mean with 90% confidence. Flight 7 is much worse. This makes it hard to conclude that variations among the flights are significant based solely on these measurements, but other information may corroborate them.

There is a good correlation ($R = 0.75$) between H and w_e for the cloudy cases. Since w_e is directly related to the rate of change of H this correlation can be expected and confirms that measured variations in w_e are physical. Correlation with other measured quantities is weak however. In particular, $w_e\Delta\overline{\theta_v}$ (not shown but almost exactly correlated with $w_e\Delta\overline{\theta_l}$, Table 5.4) is not apparently correlated with the buoyancy flux at the surface (Table 3.2) or its vertical integral (Fig. 3.2) except possibly Flight 10 with the high values.

This lack of correlation is somewhat disappointing as far as recommending an entrainment closure for mixed layer models but there are a number of reasons for not expecting good correlation. The first of these is that variations in radiative flux divergence at cloud top are controlling w_e. This can be seen by obtaining the entrainment relation for $\overline{w'\theta_v'}$ from

$$(\overline{w'\theta_e'})_H \;=\; -w_e\Delta\overline{\theta_e} \;+\; (\Delta F)_H \tag{5.3}$$

and

$$(\overline{w'q_w'})_H \;=\; -w_e\Delta\overline{q_w} \tag{5.4}$$

where $(\Delta F)_H$ is the net radiative flux divergence across the entrainment zone. Following Deardorff (1980b) then

$$w_e(-\alpha\Delta\overline{\theta_e} \;+\; \theta\Delta\overline{q_w}) \;=\; (\overline{w'\theta_v'})_H \;-\; \alpha(\Delta F)_H \tag{5.5}$$

where α is a constant depending on temperature. From this we see that w_e may vary depending on $(\Delta F)_H$ even if buoyancy flux is specified. We shall see in a

succeeding section however, that the total radiative flux divergence at cloud top is very similar for each flight. The problem then becomes one of determining whether the distribution of the total LW flux divergence varies between flights. The SW extinction depth in SC is long enough that flux divergence occurs well within the cloud layer and doesn't contribute directly to the energy balance in the entrainment region.

Another possible reason that entrainment flux doesn't correlate well with mixed layer flux may be that it depends on the respective production and consumption terms in the TKE balance rather than the net flux (Stage and Businger, 1981a). Further data analysis including conditional sampling (Mahrt and Paumier, 1984) would be required to test this theory. Another possibility would be the influence of shear-forced entrainment but there is little evidence for this from the soundings. Possibly numerical modeling with the experimental data as inputs could be used to sort out the causes for w_e variation.

In a further effort to determine the factors driving w_e, I attempted to separate w_e into its components (Eq. 5.1). Unfortunately, horizontal variations in H and the aircraft flight position make dH/dt very hard to determine. For DYCOMS the slope in H along the crosswind direction, up to the west, seems to dominate. In some cases dH/dt appears to be less than zero and in no case could a good estimate for w_H be obtained. The range of estimates for w_H is about -9.5 to 2.8 mm s^{-1} resulting in boundary layer divergence estimates from 1.2 x 10^{-5} to -3.8 x 10^{-6} s^{-1}. While zero is probably a better estimate for the minimum divergence in these conditions, the median of these estimates agrees well with climatology (Neiburger, 1960).

5.3.3 Entrainment From Total Water

The w_e for DYCOMS cases has been estimated from total water flux and mean measurements. This technique is somewhat more complicated than ozone-derived

but is a nearly independent check on those estimates. The entrainment relation from (5.1) for total water substance is

$$w_e \, \Delta\overline{q_w} = - \, (\overline{w'q'_v} + \overline{w'q'_l} + \widetilde{wq_l})_H \tag{5.6}$$

where $\widetilde{wq_l}$ is the gravitational settling, or drizzle flux of liquid water. The flux at H is evaluated by linear extrapolation of the the flux profile measured in the boundary layer (Fig. 3.2). The uncertainty in these measurements due to instrument limitations is discussed in Secs. 2.3 and 3.4. Nevertheless, w_e using (5.6) agrees well with (5.2) except for Flight 5 (Table 5.2). This result also confirms the physical nature of the variation of w_e between cases. The agreement is encouraging for aircraft experiments that do not have O_3 measurements available, however non-linearities in the $\overline{w'q'_w}$ profiles mean the measurements are probably not fully reliable. Aircraft instrumentation for the components of total water flux needs continued development. Inclusion of drizzle flux is generally not significant to the extrapolated flux value.

5.3.4 Comparison to Previous Measurements

In comparison to other measurements of w_e in the cloud-topped boundary layer, DYCOMS values are well to the low end. The only other measurement from the same location is Hanson (1984) whose $w_e = 3.5$ mm s^{-1} agrees well with DYCOMS. The measurements from further north off the California coast (Brost et al., 1982a) and the North Sea (Nicholl, 1984; Nicholls and Leighton, 1986) are about a factor of two higher. These other estimates are all based on total water flux and mean measurements. Compared to mixed-layer model estimates, the DYCOMS w_e definitely favors values of the "minimum entrainment" hypothesis (Lilly, 1968; Deardorff, 1976; Stage and Businger, 1981b). DYCOMS w_e does not agree well with results from LES models (Deardorff, 1980a; Moeng, 1986) which yield w_e in the 6 to 20 mm s^{-1} range, but did not include SW.

5.4 THERMODYNAMIC BUDGETS

In this section mixed-layer budgets of total water and thermodynamic energy, including radiative flux components, are discussed. The total water budget balance is an estimator of the uncertainty of the measurements and a check on the assumptions and analysis technique. The energy budgets are used to indicate what the dominant SC processes are and how to approach their parameterization. They are also used to estimate component terms like SW divergence that are hard to measure.

5.4.1 Total Water

The conservation relation for total water ($q_w = q_l + q_v$) is

$$\frac{d\overline{q_w}}{dt} + \frac{\partial(\overline{w'q'_w} + \widetilde{wq_l})}{\partial z} = Q_q \tag{5.7}$$

where Q_q, the source term for water, is now a residual measure of error. As in Sec. 4.2.1, the total derivative of the mean is actually the change measured by the aircraft plus the change due to aircraft position relative to the mean wind (Fig. 4.1). The results are shown in Table 5.3.

As expected for steady-state flow over a warmer surface, dq_w/dt is positive and the q_w increase is supplied by divergence of the turbulent flux. The sign of these processes is the same in each case and the magnitudes nearly balance. The small residuals Q_q confirm our faith in the measurement and analysis techniques. The average $d\bar{q}_w/dt$ is about equal to $\overline{u}\partial\overline{q}_w/\partial x$ expected from Clausius-Clapeyron at constant relative humidity for the given SST gradient.

The relative magnitude of the components of total water flux is seen in the flux profiles (Fig. 3.2). The turbulent liquid water flux is positive, increasing toward cloud top, and usually comparable to $\overline{w'q'_v}$ but smaller. Drizzle is small compared to $\overline{w'q'_v}$ except for Flight 10, and has only a small effect on the average

divergence. Perhaps if the scatter in measuring $\overline{w'q_v'}$ were not so large the effect of drizzle would be more significant to this analysis.

5.4.2 Radiative Fluxes

Composite LW flux profiles formed from the level leg averages are shown in Fig. 5.1. The scatter among the data points for the most part reflects the variations in SST and cloud top temperature between the flights. While there may be some contention about the exact shape of the profile below cloud, the data fit theoretical profiles for a warm surface and solid cloud layer (Slingo et al, 1982; Fravalo et al., 1981). The sub-cloud heating and total cloud top cooling are very consistent among the cloudy cases, apparently not sensitive to the variations in cloud structure or liquid water content found in DYCOMS. This is expected because of the relatively small LW extinction depth. The clear case is, of course, quite different. Note also that the sub-cloud heating is a substantial portion of the total cooling and should not be ignored.

The missing assumption needed to use these LW measurements in an entrainment relation (like 5.3) or a mixed layer energy budget (next section) is the distribution of LW divergence between inversion and mixed layers. Albrecht et al. (1985) have examined the changes of θ, LW, and q_l from several soundings in the inversion region. Using the time series from the cloud top legs we can observe many instances of inversion crossings. Fig. 5.2 is an example. From this example, and many others studied, it is clear that the LW cooling occurs almost entirely in the cloudy region which is within (below) the boundary of the cool region which defines the instantaneous position of the inversion. Note that there is an indication of about 10 to 15 W m^{-2} residual cooling in the inversion only when passing out of the cloud region. A major portion of this is probably due to instrument response lag. In any event, at least 70 of the total 80 W m^{-2} net LW divergence is in the cloud layer. The full LW cooling is not reached until the aircraft is about 3 km horizontally within the cloud. This confirms the findings of Albrecht et

al. (1985) that the zone of maximum LW cooling occurs somewhat below the θ transition. In Fig. 5.2 no subsaturated, cool regions are found; in this case the θ and q_l transition zones are the same. Cloud-free regions in the mixed layer are occasionally, but not commonly, found in other flights however, in agreement with the cases of Albrecht et al. (1985). These regions have been proposed as the mechanism by which cloud layers become metastable to the entrainment process (Rogers and Telford, 1986).

In the time series of Fig. 5.2 the aircraft flight level is such that it passes about equally through cloudy and clear areas. From this it appears that the LW extinction depth is roughly the same as the depth of the cloud top excursions. This depth can be estimated from data. The q_l spectra at cloud top peak at about 2×10^{-2} Hz so the horizontal wavelength is about 5 km. Assuming the domes have a half-sinusoidal shape and using an interface slope of 0.06 at $\pi/4$ (Lenschow et al., 1988b) the typical vertical variation is 70 m. This structure is in reasonable agreement with LES results of Moeng (1987). If the entrainment zone is defined, as in that paper, to include the entire depth of cloud top excursions, then most the LW cooling occurs in this region. If the top of the mixed layer is defined as the level at which the turbulent fluxes go to zero, then the LW cooling occurs in the mixed region. It is also quite likely that the distribution of LW divergence is not a constant ratio but varies depending on the turbulence structure which in turn affects the amplitude of cloud top fluctuations.

SW measurements in the SC are characterized by large variability, especially $SW \uparrow$ above and $SW \downarrow$ in and below cloud. This is a reflection of the variation of cloud structure which is manifest over a wide range of scales. For this reason measurements from a single aircraft are subject to large uncertainties even when averaged over tens of kilometers. The example profiles constructed from leg averages in Fig. 5.3 point out the effect of SC on SW fluxes. All cloud cases have a total albedo 0.4 to 0.5 compared to about 0.04 for the sea surface. The

net flux above the cloud layer is barely half that of the clear case. This is what makes SC so important to the global radiative balance.

The quantity of interest for SC thermodynamics is the divergence of the net SW flux, considered positive in the downward direction. All DYCOMS cases have significant SW divergence (heating) including Flight 8. This apparent heating is not restricted to the cloud layer but appears fairly linearly through the marine boundary layer (Fig. 5.3). This is a somewhat puzzling observation with respect to theoretical SW models (Stephens, 1978; Slingo and Schrecker, 1982; Hanson and Derr, 1987) and previous observations (Stephens et al., 1978; Slingo et al., 1982). To some degree the SW divergence observations may be due to flight geometry and a change in cloud thickness with time. Since the lower legs were flown first, any increase in cloud transmittance with time would be interpreted as a positive vertical gradient. A scatter plot of the change in net SW between legs, as a function of altitude (Fig. 5.4) confirms that SW is increasing at all altitudes below cloud top except for Flight 5 and one leg in Flight 7. The average change for Flight 8 is also positive but much smaller. The increase in cloud transmittance must be due to a decrease in cloud depth and/or liquid water concentration with time. This is consistent with the conceptual model of SC in transition to tradewind cumulus along the trajectory. An alternate conceptual explanation is thinning of the cloud in the insolated phase of the diurnal cycle. Although this is an interesting observation in its own right, it makes it difficult to extract the vertical component of the net SW divergence since $\delta SW/\delta t$ (Fig. 5.4) is not constant. Consequently, the best estimate for SW divergence across the mixed layer is obtained from the difference between the above-cloud and subsequent near-surface leg averages. Obviously this is less informative and more uncertain than a full SW flux profile. In each case a substantial heating is still observed and these values are input to the budgets in the next subsection.

None of this explains the measured heating for Flight 8, the case without low cloud. The temperature and moisture profiles for this case were input to a

clear-air radiative transfer model (Cox and Griffith, 1979). The model SW profile showed about one-third the observed divergence. In addition, the modeled $SW\downarrow$ at the boundary layer top exceeded the measurement by about 75 W m^{-2}. This difference is probably attributable to the presence of high clouds which were noted during the flight. This is indicated also by excess measured $LW\downarrow$ compared to the model. Thus one possible explanation for the observed SW divergence is decrease in upper-level cloud creating an effect similar to that described above but of a small magnitude. Another possibility is absorption by marine aerosol-haze. A dark grey haze within the marine boundary layer was clearly visible to the flight observers. Unfortunately, absorption characteristics of the particles are not available to test this hypothesis. This question is related to the topic of "anomalous absorption" (Stephens et al., 1978) which has a background in the literature but is beyond the scope of DYCOMS measurements. While the exact magnitude of the DYCOMS net SW divergence eludes our measurement technique, the respective estimates agree fairly well with predictions and contribute to validation of the models (Slingo and Schrecker, 1982; Liou and Wittman, 1979; Stephens et al., 1978, 1984).

5.4.3 Energetics

The energy conservation relation in the mixed layer may be written in terms of an arbitrary temperature θ_x conserved with respect to phase change as

$$\frac{d\overline{\theta_x}}{dt} + \frac{\partial\overline{w'\theta_x'}}{\partial z} = Q_{\theta_x} \tag{5.8}$$

In this section we will concentrate on θ_l (Betts, 1982; Deardorff, 1976b) since it does not rely on q_v measurement in cloud, a problem discussed in Sec. 2.3. Specifically then

$$\frac{d\overline{\theta_l}}{dt} + \frac{\partial\overline{w'\theta_l'}}{\partial z} = \frac{1}{\rho c_p}\left(\frac{\partial SW}{\partial z} - \frac{\partial LW}{\partial z}\right) + \frac{L}{c_p}\frac{\partial\widetilde{wq_l}}{\partial z} \tag{5.9}$$

where SW is net downward and LW net upward radiative flux, and the drizzle term represents an additional sink of θ_l. Since the flux profiles can no longer be assumed linear, as in the case of O_3 or q_w, this equation becomes difficult to evaluate near the mixed layer top using measurements. If, however, we integrate (5.9) from near the surface through the entrainment zone, the resultant terms can be estimated from measurements. These are

$$-H\left[\frac{d\overline{\theta_l}}{dt}\right] + w_e\Delta\overline{\theta_l} + (\overline{w'\theta_l'})_o + \frac{1}{\rho c_p}(SW_H - SW_o - LW_H + LW_o) = R_\theta \quad (5.10)$$

where the total time derivative term is a vertical mixed-layer average combining the aircraft measured change and the relative position change as in Sec. 4.2.1. The zero subscripts refer to values measured at the lowest flight level and the H subscripts to those just above cloud top. The residual R_θ is a measure of the total error. In this bulk energy budget the drizzle flux and the distribution of radiative flux divergence no longer enter, assuming drizzle doesn't reach the surface. It is useful to compare the relative importance of the various inputs and their variation among the cases.

Since the SW estimates are so uncertain, the R_θ term is assumed to be zero and (5.10) is used to diagnose the net SW divergence. The results are shown in Table 5.4. In all cases the boundary layer θ_l is increasing at a rate corresponding to the mean SST gradient and the previously noted increase in q_w. The surface flux is fairly consistent in the cloudy cases and the turbulent flux divergence contributes about half the θ_l increase with time, except for Flight 10. The LW cooling is consistent among the cloudy cases and the diagnosed SW heating is reasonably constant for those at midday. In each of these the SW heating exceeds LW cooling to some degree, balancing the remainder of $d\theta_l/dt$. This finding agrees with North Sea SC measurements (Slingo et al., 1982; Nicholls, 1984) whose daytime SW heating balanced or slightly exceeded LW cooling. The Pacific case of Hanson (1984) shows SW heating exceeds LW cooling by more than a factor of two for

relatively high liquid water content. The effect of SW heating in cloud can be seen in the $\overline{w'\theta_l'}$ flux profiles (Fig. 3.2) which show a positive slope in cloud below $z/z_i = 0.95$, except Flight 1.

The early morning case, Flight 10, has different energetics. Here the time increase is entirely balanced by turbulent flux divergence which also balances the excess LW radiative divergence. This implies that SW divergence inhibits entrainment, presumably by stabilizing the cloud layer (Fravalo et al., 1981). This is also reflected in the $\overline{w'\theta_v'}$ profile (Fig. 3.2h) which is higher in cloud for Flight 10 than any other. Radiatively this case is similar to Brost et al. (1982a,b) but without the wind shear that typified their cases, the flux profiles and w_e are quite different. This is the only case in which drizzle is a significant contribution to the water flux suggesting SW absorption influences the drop distribution interactively.

The clear case, Flight 8, is almost entirely stabilized as SW heating overcomes the slight LW cooling, throughout the layer depth here, and drives the time increase in temperature reducing the air-sea temperature difference (Table 3.1) and surface flux to near zero. About 60% of the previously discussed observed SW divergence is diagnosed by the budget. A slight moisture-driven buoyancy flux persists near the surface, but turbulence is greatly reduced from other cases, the resulting entrainment is near zero, and the mixed layer shows evidence of detachment from the surface layer. What is the evolution of this boundary layer? A meteorological disturbance propagating from the north induced the SC to dissipate. In the absence of cloud-generated turbulence the Flight 8 case results. Satellite photos show that the SC did not re-appear in the area on the following day but did two days later. Simply turning off ΔSW did not allow the upper layer to cool to saturation. The northern soundings from Flight 9 (Figs. A.19a and A.21b), the day following Flight 8, show a surface based mixed layer up to about 500 m. The mixed layer θ_l is the same as Flight 8 but q_v has increased. Further south along the trajectory (Figs. A.19b and A.20b), the surface-based mixed layer deepens and warms, some mixing now extends vertically up to about

1200 m, and a cloud layer is formed. The cloud-topped mixed-layer has been re-established from the surface up. Further south still (Fig. A.20a) the mixed layer deepens to about 1400 m and clouds persist.

The original cause of the dissipation is not apparent from this data. Increased subsidence has been suggested (Weaver, 1987) but if anything the boundary layer grew slightly during Flight 8. The θ_e profile is slightly unstable to entrainment into a cloudy layer but less so than many other flights. The relation between entrainment instability and break-up is not yet clear (Kuo and Schubert, 1988). How these clearing episodes relate to the break-up into tradewind cumulus is not clear either. The boundary layer characteristics are entirely different (Schubert, 1976). Finally, an entirely different SC dispersion scenario occurred when a tropical disturbance affected the region (Sec. 2.2 and 4.3, Figs. A.12 and A.13).

Returning to the budgets, the measured SW divergences (in parentheses) do not match the diagnosed values for most flights. This is most likely due to the large uncertainty associated with the measurements. The respective averages for the cloudy cases match well which is some consolation.

5.5 CONCLUSION

Most of the DYCOMS experimental cases are climatologically typical of eastern North Pacific marine SC. In addition, there are a number of atypical or "disturbed" cases which serves as a valuable comparison. These observational data contribute directly to our understanding of SC dynamics and thermodynamics. They also form an excellent basis for testing numerical models and addressing some of the problems of parameterization.

The w_e has been determined using a new technique, based on O_3 measurements. This method has an advantage over others due to its lack of assumptions and the difficulty of making meteorological scalar measurements in cloud. An independent estimate for w_e is provided which can be used to study its relationship to mixed layer fluxes in the pursuit of a parameterization for entrainment. The

w_e results will also be used with measurements of other chemical species during DYCOMS to construct budgets from mean concentrations.

In regard to the use of a mixed-layer type formulation in representing DYCOMS cases, the data definitely indicate that SW divergence cannot be ignored. The bulk energy budgets require a relatively large amount of SW heating, supported by SW flux measurements, of which a significant portion occurs well into the "mixed" layer. The θ_l flux profiles are no longer linear as required by the model. The magnitude of the observed effect of SW damping entrainment indicates that even a diurnally averaged model should incorporate SW flux divergence in the mixed layer. Study of the diurnal cloud cycle will be one of the most interesting results of the FIRE program (Albrecht et al., 1988).

Many other applications of mixed layer assumptions are, however, upheld by the data. The fact that the advective time rate of change is in equilibrium with the observed SST gradient means that the time scale for vertical adjustment is small compared to advection or the diurnal radiative cycle. The impact of drizzle is generally small. The conserved scalar mean profiles are well-mixed and no evidence for detached or shear-driven layers is found in the typical cases. These processes may be important in the disturbed cases however, and merit further study. These cases provide examples that SC dissipation can be caused by a number of different perturbations.

The measured LW flux profiles confirm that cooling occurs in a relatively thin, but finite, layer at cloud top, clearly associated with the liquid water discontinuity. The difficulty in determining LW distribution between entrainment and mixed layers is due to the problem of approximating the finite entrainment depth by a jump condition. Perhaps the development of a fast response net LW instrument would help. The LW extinction depth could be measured accurately as a function of cloud physical parameters and correlation between cooling and vertical velocity could be obtained.

Table 5.1: Entrainment velocity from O_3 measurements. Uncertainties on inversion-level flux are 90% confidence limits on the mean. Uncertainty on the average w_e is 90% confidence limit based on the individual flight values excluding Flight 8.

FLIGHT NUMBER	1	2	3	4	5	6	7	8	9	10	AVE
$(\overline{w'O_3'})_H$ (ppbv mm s^{-1})	−29.8 ±12.1	−12.2 ±10.6	−24.7 ±15.4	−55.6 ±17.6	−75.3 ±9.7	—	−22.3 ±32.6	0.0 ±19.4	—	−44.2 ±62.9	−37.7
$\Delta\overline{O}_3$ (ppbv)	15.3	6.2	25.5	23.3	14.9	—	5.3	2.1	—	9.9	12.6
σ_Δ	7.4	5.1	12.6	11.0	7.0	—	11.3	2.1	—	4.7	
w_e (mm s^{-1})	2.0	2.0	1.0	2.4	5.0	—	4.2	0.0	—	4.5	3.0 ±1.1
H (m)	733	730	588	880	925	—	1380	1034	—	1009	910

Table 5.2: Entrainment velocity from total water measurements. Symbols are defined in text.

FLIGHT NUMBER	1	2	3	4	5	6	7	8	9	10	AVE
$(\overline{w'q'_w} + \widetilde{wq_l})_H$ (mg m^{-2}s^{-1})	10.4	6.8	4.6	12.5	15 .1	—	—	2.4	—	21.2	11.8
$\Delta\overline{q}_w$ (g m^{-3})	−4.8	−3.0	−3.8	−5.9	−6.6	—	—	−3.8	—	−4.0	−4.7
w_e (mm s^{-1})	2.2	2.3	1.2	2.1	2.3	—	—	0.6	—	5.3	2.6

Table 5.3: Total water budgets (mg m^{-3} s^{-1}). Uncertainties are 90% confidence limits on the average over all flights.

FLIGHT NUMBER	1	2	3	4	5	6	7	8	9	10	AVE
$D\overline{q_w}/Dt$	0.02	0.01	0.03	0.05	0.02	—	—	0.02	—	0.01	0.02 ±0.01
$-(\partial\overline{q_w}/\partial n)(Dn/Dt)$	0.02	0.02	0.0	-0.04	0.0	—	—	0.02	—	0.0	0.0 ±0.02
$\partial(\overline{w'q'_w} + \widetilde{wq_l})/\partial z$	−0.04	−0.04	−0.04	−0.04	−0.03	—	—	−0.02	—	−0.01	−0.03 ±0.01
Q_q	0.0	−0.01	−0.01	−0.03	−0.01	—	—	0.02	—	0.0	−0.01 ±0.01

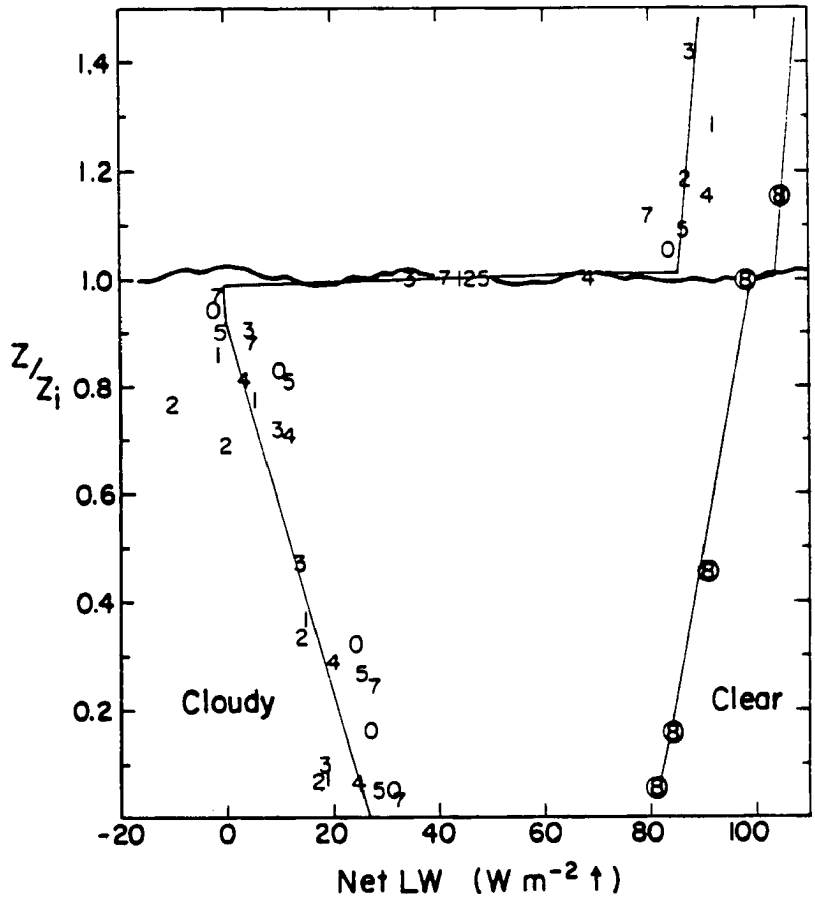

Figure 5.1: Net LW radiative flux from level legs. Numbers locate values from each flight. Clear refers to the cloud-free case and cloudy is a composite of cases with cloud-topped boundary layers.

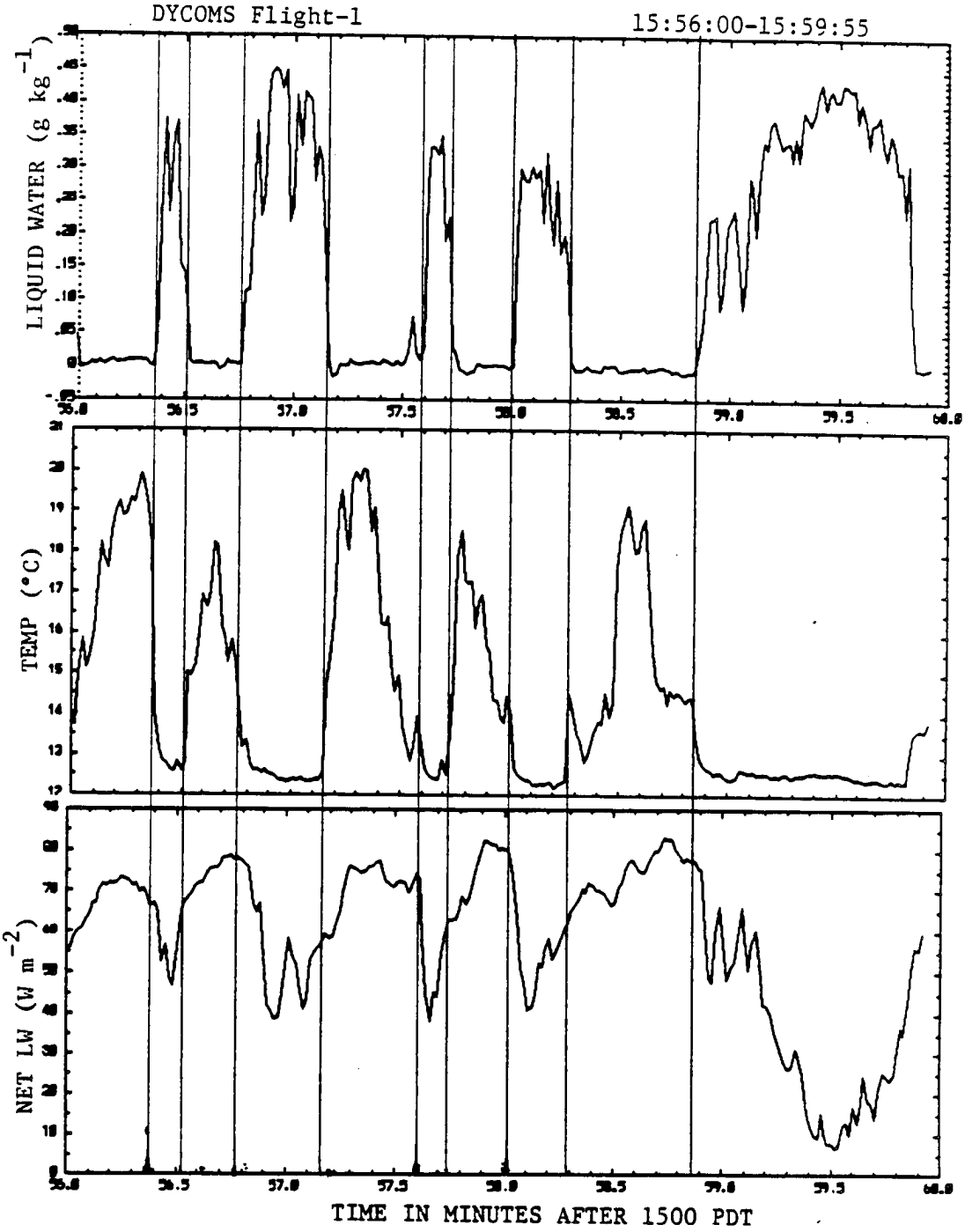

Figure 5.2: Time series of liquid water mixing ratio, temperature, and net LW radiative flux for a segment from cloud-top leg. Net LW has been advanced approximately 1 s to account for its slower response time.

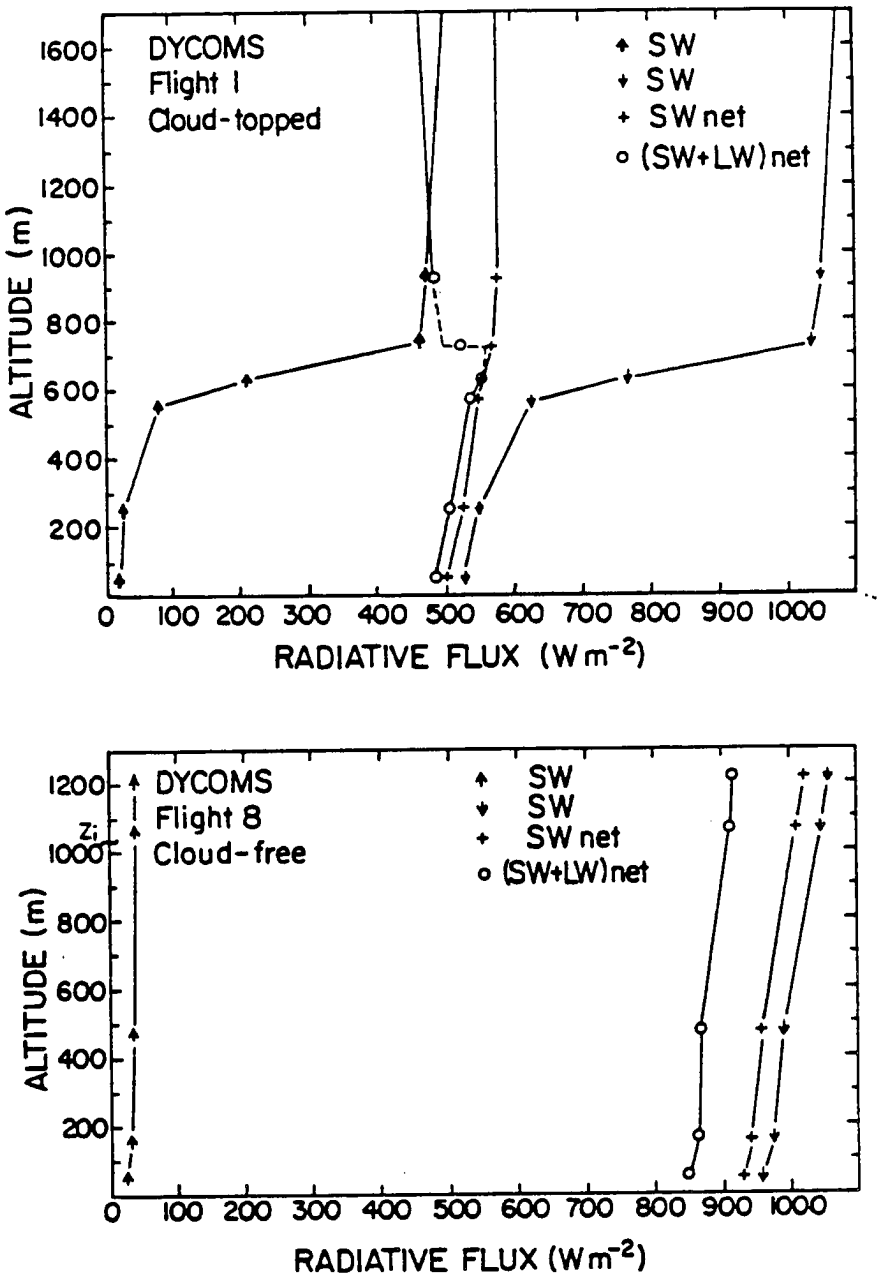

Figure 5.3: Example SW profiles from level leg data. Net (SW+LW) is positive downward.

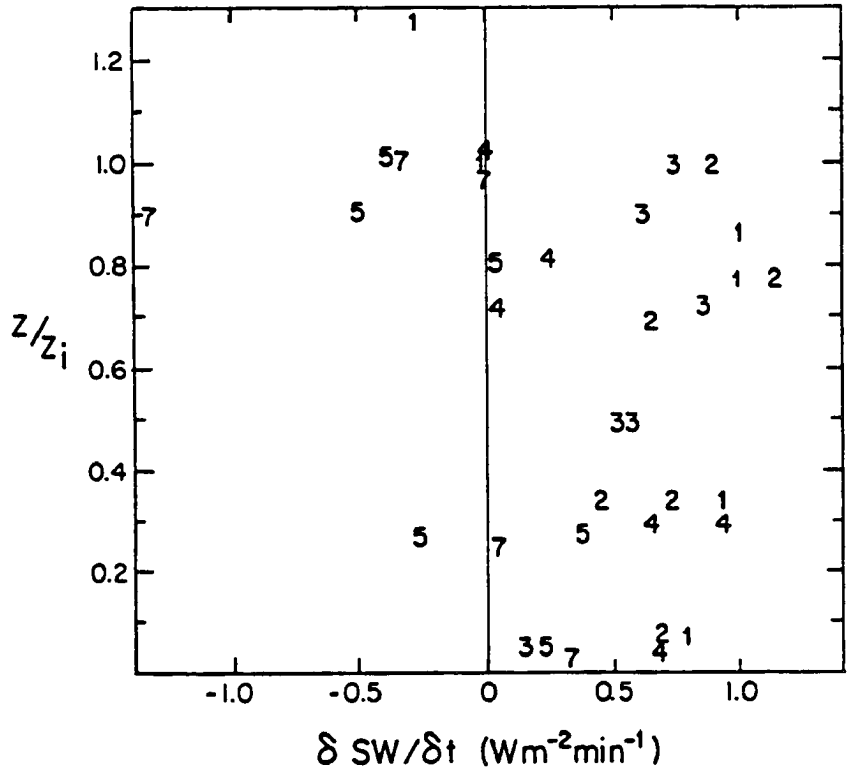

Figure 5.4: Change of net SW over time between sets of legs. Digits are flight numbers.

Table 5.4: Temperature budgets (mK m s^{-1}). Entries in the average column are for all cases for the first three lines. The average LW term excludes the clear case, Flight 8, and average SW excludes both Flights 8 and 10. Numbers in parentheses are SW divergence estimates from observed profiles.

FLIGHT	1	2	3	4	5	6	7	8	9	10	AVE
$-H[\frac{d\overline{\theta_l}}{dt}]$	−44	−22	−35	−44	−46	—	−55	−31	—	−30	−39
$w_e\Delta\overline{\theta_l}$	12	10	4	10	23	—	20	0	—	24	15
$(\overline{w'\theta_l'})_o$	13	4	10	10	9	—	7	1	—	11	9
$-\frac{1}{\rho c_p}\Delta LW$	−64	−60	−57	−55	−49	—	−47	−16	—	−46	−54
$\frac{1}{\rho c_p}\Delta SW$	83	68	78	79	63	—	75	46	—	41	74
	(15)	(87)	(97)	(55)	(82)	—	(112)	(76)	—	(39)	(75)

Chapter 6: SUMMARY

The DYCOMS dataset has proven to be a fertile field for nurturing scientific hypotheses. The intensity, scope, and quality of the data show how much can be done with modern instrumentation in a carefully planned field program. Hopefully it will continue to be a valuable resource for years to come. The statistical uncertainties are often large. No apology is needed for this. Experimentation in a research mode expects to stretch the limits of its resources. Observational analysis remains essential to the advancement of atmospheric science.

I believe progress has been made here in understanding the processes that control SC and O_3 in the atmosphere. This progress has come in two basic ways: through direct observations and through comparisons with model predictions. Direct observations contribute to our knowledge of the mean state of the SC regime and its variability, for example, the break-up and re-formation cycle of SC or transport of O_3 lamina. These phenomena lead to hypotheses about the driving mechanisms and feedbacks. Direct measurement of important processes like surface deposition and entrainment are necessary aspects of testing these hypotheses. Another valuable way of testing hypotheses is through manipulation of numerical models; in a system as complex as SC it becomes essential. But models necessarily simplify reality and must be tested continually. Documentation of model substantiation and disputation has been a major emphasis of this work.

Many possibilities for further research arise from this analysis. A large flux dataset like this is useful for testing flux parameterizations. Two possibilities are surface flux (Blanc, 1985) and mixed layer internal circulation (Wang and

Albrecht, 1986). TKE budgets for the cases could be constructed in a further effort to parameterize entrainment.

One of the most exciting potentials of this study is to integrate with the chemical sampling of other DYCOMS investigators to form full meteorological and chemical case studies. This could be a step toward unraveling that complex network of processes governing trace gas influence in climate change. Another possibility is using these data in a photochemical model to deduce concentrations of species that are difficult to measure.

This study has shown a number of difficulties involved with single aircraft sampling. Several of these, like SW and inversion height measurement, could be improved with multiple platforms and/or a variety of sensors. The FIRE program is such an effort. Hopefully, collaboration between DYCOMS and FIRE investigators will improve the results of both.

Chapter 7: REFERENCES

Ackerman, S. A. and S. K. Cox, 1981: Aircraft observations of the shortwave fractional absorptance of non-homogeneous clouds, *J. Appl. Meteorol.*, *20*, 1510-1515.

Albrecht, B. A., R. S. Penc, and W. H. Schubert, 1985: An observational study of cloud-topped mixed layers, *J. Atmos. Sci.*, *42*, 800-822.

Albrecht, B. A., D. A. Randall, and S. Nicholls, 1988: Observations of marine stratocumulus clouds during FIRE, *Bull. Am. Meteorol. Soc.*, *69*, 618-626.

Aldaz, L., 1969: Flux measurements of atmospheric ozone over land and water, *J. Geophys. Res.*, *74*, 6943-6946.

Baumgardner, D., 1983: An analysis and comparison of five water droplet measuring instruments, *J. Clim. Appl. Meteorol.*, *22*, 891-910.

Baumgardner, D., 1986: Airborne measurements for cloud microphysics, Bulletin No. 24, Research Aviation Facility, National Center for Atmospheric Research, Boulder, CO.

Baumgardner, D., 1987: Corrections for the response times of particle measuring probes, reprint for AMS Instrumentation Conference, New Orleans, LA, 148-151.

Baumgardner, D., W. Strapp, and J. E. Dye, 1985: Evaluation of the Forward Scattering Spectrometer Probe. Part II. Corrections for coincidence and dead-time losses, *J. Atmos. Oceanic Technol.*, *2*, 626-632.

Betts, A. K., 1982: Saturation point analysis of moist convective overturning, *J. Atmos. Sci.*, *39*, 1484-1505.

Blanc, T., 1985: Variation of bulk-derived surface flux, stability, and roughness results due to the use of different transfer coefficient schemes, *J. Phys. Oceanogr., 15*, 650-669.

Bolton, D., 1980: The computation of equivalent potential temperature, *Mon. Wea. Rev., 108*, 1046-1053.

Bradley, S. G. and W. D. King, 1979: Frequency response of the CSIRO liquid water probe, *J. Appl. Meteorol., 18*, 361-366.

Brost, R. A., D. H. Lenschow, and J. C. Wyngaard, 1982a: Marine stratocumulus layers. Part I: Mean conditions, *J. Atmos. Sci., 39*, 800-817.

Brost, R. A., J. C. Wyngaard, and D. H. Lenschow, 1982b: Marine stratocumulus layers. Part II: Turbulence budgets, *J. Atmos. Sci., 39*, 818-836.

Buck, A. L., 1976: The variable-path Lyman-alpha hygrometer and its operating characteristics, *Bull. Amer. Meteorol. Soc., 57*, 1113-1118.

Buck, A. L. and A. J. Hills, 1980: The Lyman-alpha hygrometer, The CHON Photochemistry of the Troposphere; Notes From a Colloquium, Summer 1980, National Center for Atmospheric Research, Boulder, CO, 106-113.

Chameides, W. and J. C. G. Walker, 1972: A photochemical theory of tropospheric ozone, *J. Geophys. Res., 78*, 8751-8760.

Chameides, W. L. and A. Tan, 1981: The two-dimensional diagnostic model for tropospheric OH: An uncertainty analysis, *J. Geophys. Res., 86*, 5209-5223.

Chameides, W. L., D. D. Davis, M. O. Rodgers, J. Bradshaw, S. Sandholm, G. Sachse, G. Hill, G. Gregory, and R. Rasmussen, 1987: Net ozone photochemical production over the eastern and central North Pacific as inferred from GTE/CITE 1 observations during Fall 1983, *J. Geophys. Res., 92*, 2131- 2152.

Chatfield, R. and H. Harrison, 1977: Tropospheric ozone 2. Variations along a meridional band, *J. Geophys. Res., 82*, 5969-5976.

Chen, C. and W. R. Cotton, 1987: The physics of the marine stratocumulus-capped mixed layer, *J. Atmos. Sci.*, *44*, 2951-2977.

Cox, S. K. and K. T. Griffith, 1979: Estimates of radiative divergence during Phase III of the GARP Atlantic tropical experiment: Part I. Methodology, *J. Appl. Meteorol.*, *36*, 576-585.

Crutzen, P. J., 1974: Photochemical reactions initiated by and influencing ozone in unpolluted tropospheric air, *Tellus*, *26*, 47-56.

Danielsen, E. F. and V. A. Mohnen, 1977: Project Dustorm Report: Ozone transport, in situ measurements, and meteorological analyses of tropopause folding, *J. Geophys. Res.*, *82*, 5867-5877.

Danielsen, E. F., S. E. Gaines, R. S. Hipskind, G. L. Gregory, G. W. Sachse, and G. F. Hill, 1987: Meteorological context for fall experiments including distributions of water vapor, ozone, and carbon monoxide, *J. Geophys. Res.*, *92*, 1986-1994.

Deardorff, J. W., 1976a: On the entrainment rate of a stratocumulus-topped mixed layer, *Q. J. R. Meteorol. Soc.*, *102*, 563-582.

Deardorff, J. W., 1976b: Usefulness of liquid-water potential temperature in a shallow-cloud model, *J. Appl. Meteorol.*, *15*, 98-102.

Deardorff, J. W., 1980a: Stratocumulus-capped mixed layers derived from a three-dimensional model, *Boundary Layer Meteorol.*, *18*, 495-527.

Deardorff, J. W., 1980b: Cloud top entrainment instability, *J. Atmos. Sci.*, *37*, 131-147.

Deardorff, J. W., 1981: On the distribution of mean radiative cooling at the top of a stratocumulus-capped mixed layer, *Q. J. R. Meteorol. Soc.*, *107*, 191-202.

Draper, N. R. and H. Smith, 1966: Applied Regression Analysis, Wiley, 1966.

Duynkerke, P. G. and A. G. M. Driedonks, 1987: A model for the turbulent structure of the stratocumulus-topped atmospheric boundary layer, *J. Atmos. Sci.*, *44*, 43-64.

Dye, J. E. and D. Baumgardner, 1984: Evaluation of the Forward Scattering Spectrometer Probe. Part I. Electronic and optical studies, *J. Atmos. Oceanic Technol.*, *1*, 329-344.

Fabian, P. and P. G. Pruchniewicz, 1977: Meridional distribution of ozone in the troposphere and its seasonal variations, *J. Geophys. Res.*, *82*, 2063- 2073.

Fishman, J. and P. J. Crutzen, 1977: A numerical study of tropospheric photochemistry using a one-dimensional model, *J. Geophys. Res.*, *82*, 5897-5906.

Fishman, J., S. Solomon, and P. J. Crutzen, 1979: Observational and theoretical evidence in support of a significant in-situ photochemical source of tropospheric ozone, *Tellus*, *31*, 432-446.

Fishman, J. and W. Seiler, 1983: Correlative nature of ozone and carbon monoxide in the troposphere: Implications for the tropospheric ozone budget, *J. Geophys. Res.*, *88*, 3662-3670.

Fishman, J., 1985: Ozone in the troposphere, in Ozone In the Free Atmosphere, R. C. Whitten and S. S. Prasad, eds., Van Nostrand Reinhold, New York.

Fishman, J., G. L. Gregory, G. W. Sachse, S. M. Beck, and G. F. Hill, 1987: Vertical profiles of ozone, carbon monoxide, and dew-point temperature obtained during GTE/CITE 1, October-November 1983, *J. Geophys. Res.*, *92*, 2083-2094.

Fitzjarrald, D. R. and D. H. Lenschow, 1983: Mean concentration and flux profiles for chemically reactive species in the atmospheric surface layer, *Atmos. Environ.*, *17*, 2505-2512.

Fravalo, C., Y. Fouquart, and R. Rosset, 1981: The sensitivity of a model of low stratiform clouds to radiation, *J. Atmos. Sci.*, *38*, 1049-1062.

Friehe, C. A., R. L. Grossman, and Y. Pann, 1986: Calibration of an airborne Lyman-alpha hygrometer and measurement of water vapor flux using a thermoelectric hydrometer, *J. Atmos. Oceanic Technol.*, *3*, 299-304.

Galbally, I. E. and C. R. Roy, 1980: Destruction of ozone at the earth's surface, *Q. J. R. Meteorol. Soc.*, *106*, 599-620.

Garland, J. A., A. W. Elzerman, and S. A. Penkett, 1980: The mechanism for dry deposition of ozone to seawater surfaces, *J. Geophys. Res.*, *85*, 7488-7492.

Gregory, G. L., S. M. Beck, and J. A. Williams, 1984: Measurements of free tropospheric ozone: An aircraft survey from 44° North to 46° South latitude, *J. Geophys. Res.*, *89*, 9642-9648.

Hanson, H. P., 1984: On mixed-layer modeling of the stratocumulus-topped marine boundary layer, *J. Atmos. Sci.*, *41*, 1226-1234.

Hanson, H. P. and V. E. Derr, 1987: Parameterization of radiative flux profiles within layer clouds, *J. Clim. Appl. Meteorol.*, *26*, 1511-1521.

Kawa, S. R., 1986: Ozone deposition, scalar budgets and radiative heating over Texas coastal forest and ocean, Atmospheric Science Paper No. 398, Department of Atmospheric Science, Colorado State University, Fort Collins, CO.

King, W. D., J. E. Dye, J. W. Strapp, D. Baumgardner, and D. Huffman, 1985: Icing wind tunnel tests on the CSIRO liquid water probe, *J. Atmos. Oceanic Technol.*, *2*, 340-352.

Kopp, F. J., 1985: Deduction of vertical motion in the atmosphere from aircraft measurements, *J. Atmos. Oceanic Technol.*, *2*, 684-688.

Kuo, H. C. and W. H. Schubert, 1988: Stability of cloud-topped boundary layers, *Q. J. R. Meteorol. Soc.*, *114*, 887-916.

Leighton, P. A., 1961: Photochemistry of Air Pollution, Academic Press, New York.

Lenschow, D. H., 1974: The measurement of air velocity and temperature using the NCAR Buffalo aircraft measuring system, NCAR-TN/EDD-74.

Lenschow, D. H., R. Pearson, Jr., and B. B. Stankov, 1981: Estimating the ozone budget in the boundary layer by use of aircraft measurements of ozone eddy flux and mean concentration, *J. Geophys. Res.*, *86*, 7291-7297.

Lenschow, D. H., 1982: Reactive trace species in the boundary layer from a micrometeorological perspective, *J. Meteor. Soc. of Jpn.*, *60*, 472-480.

Lenschow, D. H., R. Pearson, Jr., and B. B. Stankov, 1982: Measurements of ozone vertical flux to ocean and forest, *J. Geophys. Res.*, *87*, 8833-8837.

Lenschow, D. H., I. R. Paluch, A. R. Bandy, R. Pearson, Jr., S. R. Kawa, C .J. Weaver, B. J. Huebert, J. G. Kay, D. C. Thornton, and A. R. Driedger III, 1988a: Dynamics and chemistry of marine stratocumulus (DYCOMS) experiment, submitted to Bull Am. Meteorol. Soc., in press, 1988.

Lenschow, D. H., V. Patel, and A. Isbell, 1988b: Measurements of fine-scale structure at the top of marine stratocumulus, Reprint Volume, 8th Symposium on Turbulence and Diffusion, 25-29 April 1988, American Meteorological Society, Boston, MA.

Levy II, H., J. D. Mahlman, W. J. Moxim, and S. C. Liu, 1985: Tropospheric ozone: The role of transport, *J. Geophys. Res.*, *90*, 3753-3772.

Lilly, D. K., 1968: Models of cloud-topped mixed layers under a strong inversion, *Q. J. R. Meteorol. Soc.*, *94*, 292-309.

Liou, K.-N. and G. D. Wittman, 1979: Parameterization of the radiative properties of clouds, *J. Atmos. Sci.*, *36*, 1261-1273.

Liu, S. C., D. Kley, M. McFarland, J. D. Mahlman, and H. Levy II, 1980: On the origin of tropospheric ozone, *J. Geophys. Res.*, *85*, 7546-7552.

Liu, S. C., M. McFarland, D. Kley, O. Zafirou, and B. Huebert, 1983: Tropospheric NO_x and O_3 budgets in the equatorial Pacific, *J. Geophys. Res.*, *88*, 1360-1368.

Logan, J. A., M. J. Prather, S. C. Wofsy, and M. B. McElroy, 1981: Tropospheric chemistry: A global perspective, *J. Geophys. Res.*, *86*, 7210-7254.

Logan, J. A., 1985: Tropospheric ozone: Seasonal behavior, trends, and anthropogenic influence, *J. Geophys. Res.*, *90*, 10,463-10,482.

Mahrt, L. and J. Paumier, 1984: Heat transport in the atmospheric boundary layer, *J. Atmos. Sci.*, *41*, 3061-3075.

Matthews, R. D., R. F. Sawyer, R. W. Shefer, 1977: Interference in chemiluminescent measurements of NO and NO_2 emissions from combustion systems, *Environ. Sci. Technol.*, *11*, 1092-1096.

Moeng, C.-H., 1986: Large-eddy simulation of a stratus-topped boundary layer. Part I. Structure and budgets, *J. Atmos. Sci.*, *43*, 2886-2900.

Moeng, C.-H., 1987: Large-eddy simulation of a stratus-topped boundary layer. Part II: Implications for mixed-layer modeling, *J. Atmos. Sci.*, *44*, 1605-1614.

Neiburger, M., 1960: The relation of air mass structure to the field of motion over the Eastern North Pacific Ocean in summer, *Tellus*, *12*, 31-40.

Nicholls, S., 1984: The dynamics of stratocumulus: Aircraft observations and comparisons with a mixed layer model, *Q. J. R. Meteorol. Soc.*, *110*, 783-820.

Nicholls, S. and J. Leighton, 1986: An observational study of the structure of stratiform cloud sheets. Part I. Structure, *Q. J. R. Meteorol. Soc.*, *112*, 431-460.

Nicholls, S. and J. O. Turton, 1986: An observational study of the structure of stratiform cloud sheets. Part II. Entrainment, *Q. J. R. Meteorol. Soc.*, *112*, 461-480.

Panofsky, H. A. and J. A. Dutton, 1984: Atmospheric Turbulence, Wiley-Interscience, New York, 397 pp.

Pearson, R. Jr., 1988: Measuring ambient ozone with high sensitivity and bandwidth, submitted to Rev. Sci. Instrum., in press, 1988.

Pearson, R. Jr. and D. H. Stedman, 1980: Instrumentation for fast-response ozone measurement from aircraft, *Atmos. Technol.*, *12*, 51-55.

Pearson, R. Jr. and C. J. Weaver, 1988: Ozone conservation and entrainment in cumulus congestus, submitted to J. Atmos. Sci., June 1988.

Piotrowicz, S. R., D. A. Boran, and C. J. Fischer, 1986: Ozone in the boundary layer of the equatorial Pacific Ocean, *J. Geophys. Res.*, *91*, 13,113-13,119.

Randall, D. A., 1980: Entrainment into a stratocumulus layer with distributed radiative cooling, *J. Atmos. Sci.*, *37*, 148-159.

Randall, D. A., J. A. Coakley, Jr., C. W. Fairall, R. A. Kropfli, and D. H. Lenschow, 1984: Outlook for research on subtropical marine stratiform clouds, *Bull. Am. Meteorol. Soc.*, *65*, 1290-1301.

Randall, D. A., 1984: Buoyant production and consumption of turbulence kinetic energy in cloud-topped mixed layers, *J. Atmos. Sci.*, *41*, 402-413.

Rogers, D. P. and J. W. Telford, 1986: Metastable stratus tops, *Q. J. R. Meteorol. Soc.*, *112*, 481-500.

Rogers, R. R., 1979: A Short Course in Cloud Physics, Pergammon Press, 232 pp.

Routhier, F., R. Dennett, D. D. Davis, A. Wartburg, P. Haagenson, and A. C. Delany, 1980: Free tropospheric and boundary-layer airborne measurements of ozone over the latitude range of 58°S to 70°N, *J. Geophys. Res.*, *85*, 7307-7321.

Schubert, W. H., 1976: Experiments with Lilly's cloud-topped mixed layer model, *J. Atmos. Sci.*, *33*, 436-446.

Schubert, W. H., J. S. Wakefield, E. J. Steiner, and S. K. Cox, 1979a: Marine stratocumulus convection. Part I: Governing equations and horizontally homogeneous solutions, *J. Atmos. Sci.*, *36*, 1286-1307.

Schubert, W. H., J. S. Wakefield, E. J. Steiner, and S. K. Cox, 1979b: Marine stratocumulus convection. Part II: Horizontally inhomogeneous solutions, *J. Atmos. Sci.*, *36*, 1308-1324.

Seiler, W. and J. Fishman, 1981: The distribution of carbon monoxide and ozone in the free troposphere, *J. Geophys. Res.*, *86*, 7255-7265.

Slingo, A., S. Nicholls, and J. Schmetz, 1982: Aircraft observations of marine stratocumulus during JASIN, *Q. J. R. Meteorol. Soc.*, *108*, 833-856.

Slingo, A. and H. M. Schrecker, 1982: On the shortwave radiative properties of stratiform water clouds, *Q. J. R. Meteorol. Soc.*, *108*, 407-426.

Spyers-Duran, P. A. and C. D. Winant, 1985: Comparison of sea surface temperature obtained from an aircraft using remote and direct sensing techniques, *J. Atmos. Oceanic Technol.*, *2*, 667-671.

Stage, S. A. and J. A. Businger, 1981a: A model for entrainment into a cloud-topped marine boundary layer. Part I: Model description and application to a cold-air outbreak episode, *J. Atmos. Sci.*, *38*, 2213-2229.

Stage, S. A. and J. A. Businger, 1981b: A model for entrainment into a cloud-topped marine boundary layer. Part II: Discussion of model behavior and comparison with other models, *J. Atmos. Sci.*, *38*, 2230-2242.

Stephens, G. L., 1978: Radiation profiles in extended water clouds. I: Theory, *J. Atmos. Sci.*, *35*, 2111-2122.

Stephens, G. L., G. W. Paltridge, and C. M. R. Platt, 1978: Radiation profiles in extended water clouds. III: Observations, *J. Atmos. Sci.*, *35*, 2133-2141.

Stephens, G. L., S. Ackerman, and E. A. Smith, 1984: A shortwave parameterization revised to improve cloud absorption, *J. Atmos. Sci.*, *41*, 687-690.

Thompson, A. M., 1984: The effect of clouds on photolysis rates and ozone formation in the unpolluted troposphere, *J. Geophys. Res.*, *89*, 1341-1349.

Thompson, A. H. and R. J. Cicerone, 1982: Clouds and wet removal as causes of variability in the trace-gas composition of the marine troposphere, *J. Geophys. Res.*, *87*, 8811-8826.

Wang, S. and B. A. Albrecht, 1986: A stratocumulus model with an internal circulation, *J. Atmos. Sci.*, *43*, 2374-2391.

Weaver, C. J., 1987: Observational analysis of cumulus and stratocumulus entrainment using ozone, Atmospheric Science Paper No. 422, Department of Atmospheric Science, Colorado State University, Fort Collins, CO.

Wesely, M. L., D. R. Cook, and R. M. Williams, 1981: Field measurement of small ozone fluxes to snow, wet bare soil, and lake water, *Boundary Layer Meteorol., 20*, 459-471.

Wesely, M. L., D. R. Cook, R. L. Hart, and R. M. Williams, 1982: Air-sea exchange of CO_2 and evidence for enhanced upward fluxes, *J. Geophys. Res., 87*, 8827-8832.

Wesely, M. L., 1983: Turbulent transport of ozone to surfaces common in the eastern half of the United States, from *Trace Atmospheric Constituents: Properties, Transformations, and Fates*, S. E. Schwarz, ed., John Wiley and Sons, Inc.

APPENDIX A: DYCOMS SOUNDINGS

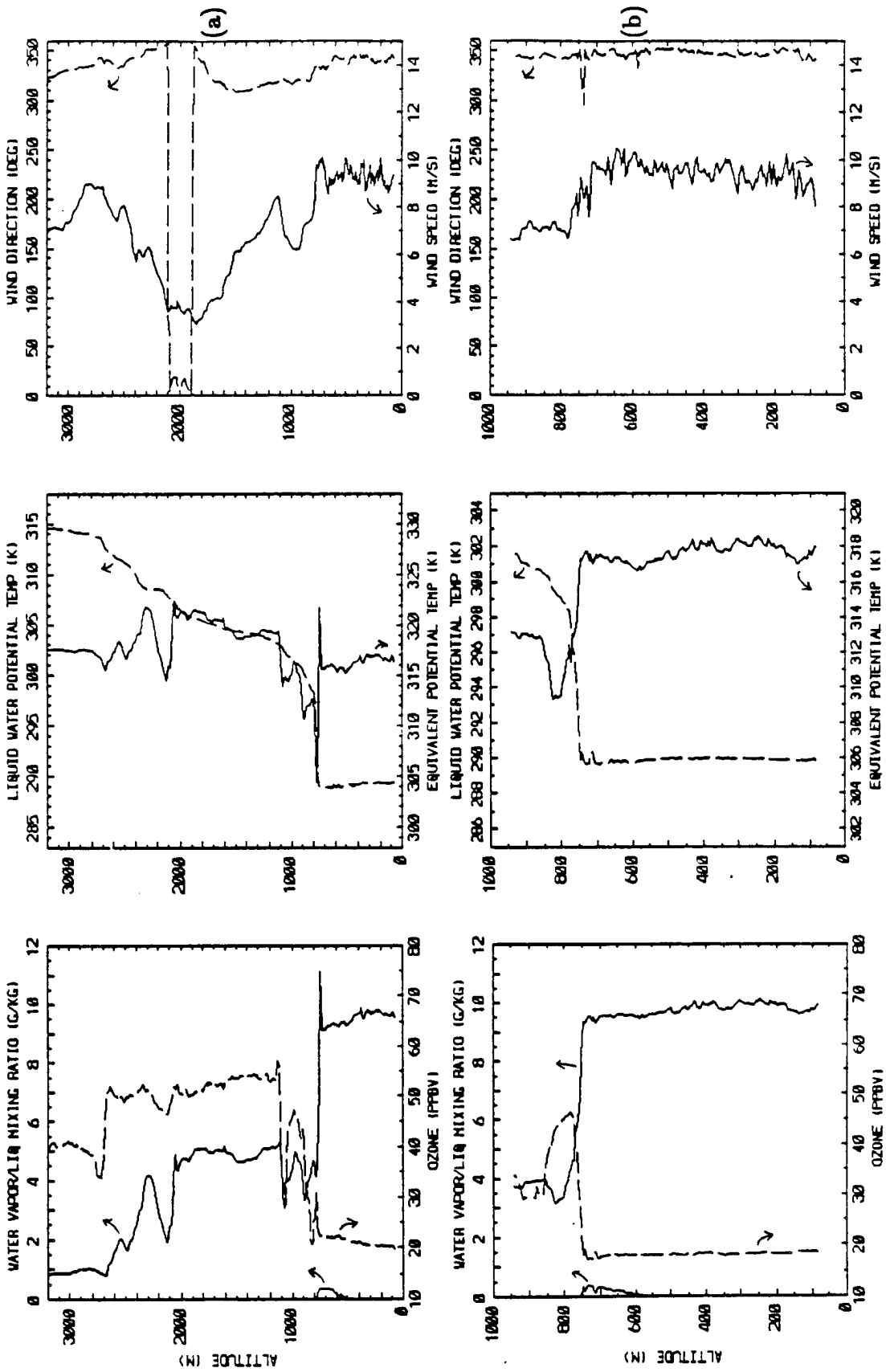

Figure A.1: Flight 1, slant descents 12:09-12:26(a) and 14:34-14:47(b). All times are PDT.

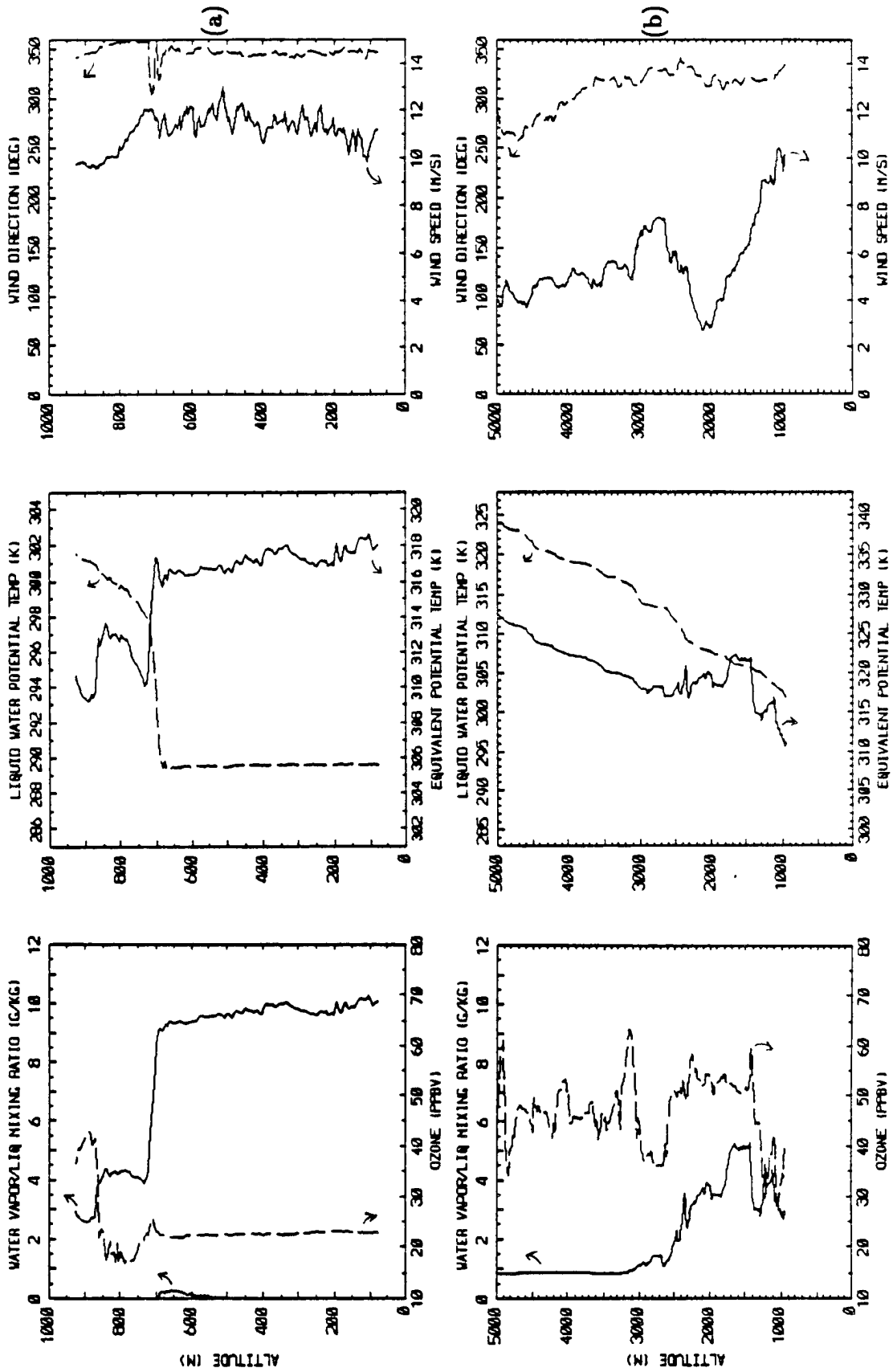

Figure A.2: Flight 1, slant ascents 16:21-16:29(a) and 17:00-17:14(b).

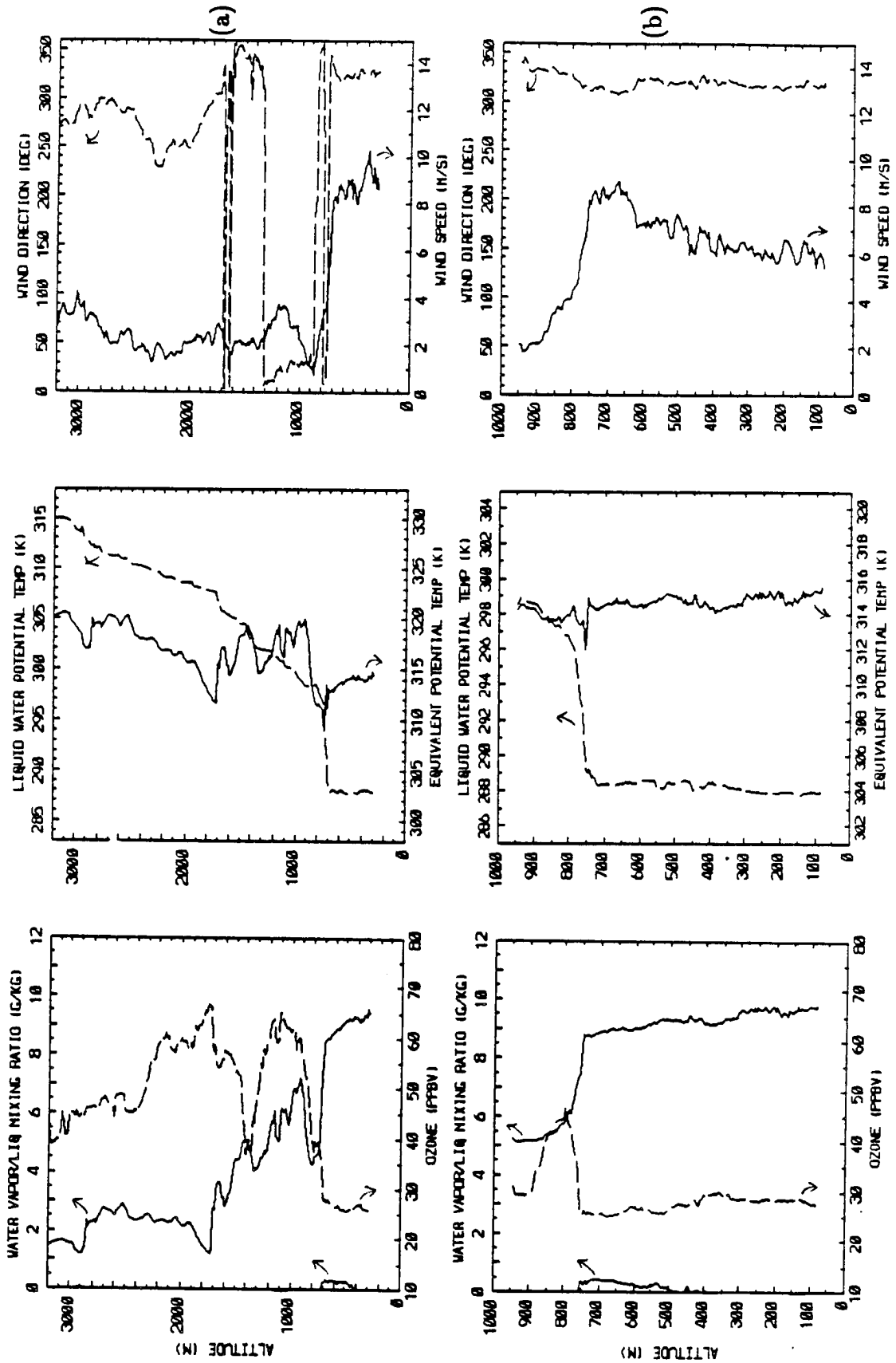

Figure A.3: Flight 2, spiral descent 09:58-10:25(a) and slant descent 13:00-13:10(b).

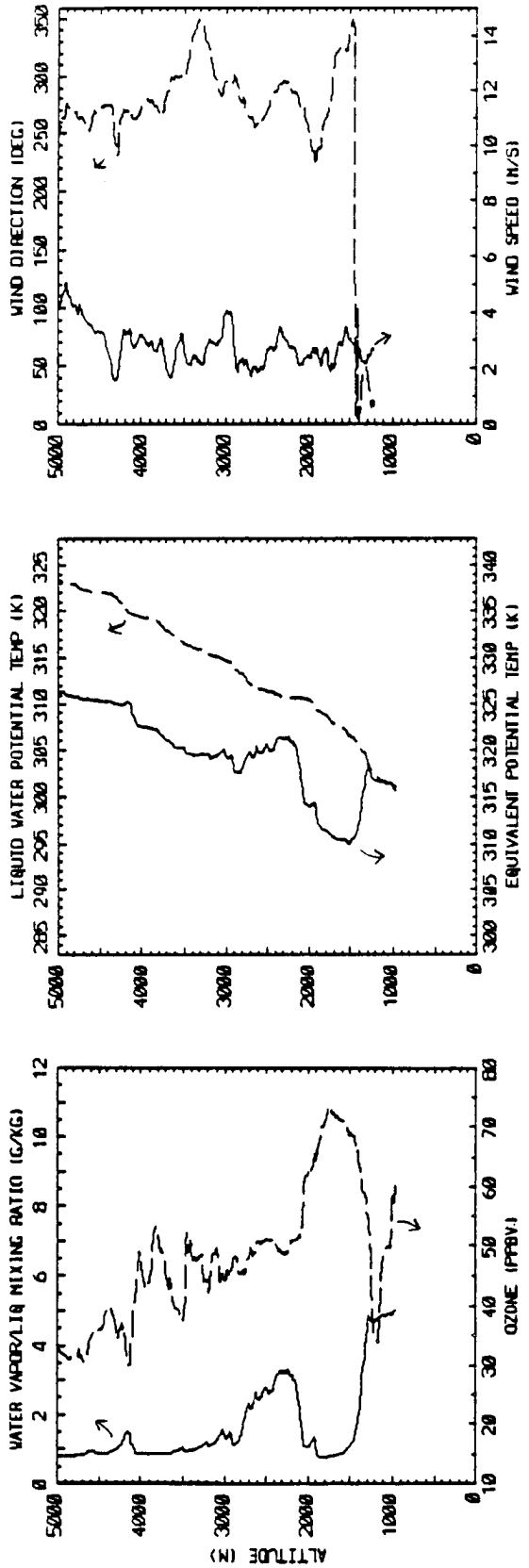

Figure A.4: Flight 2, slant ascent 14:59-15:15.

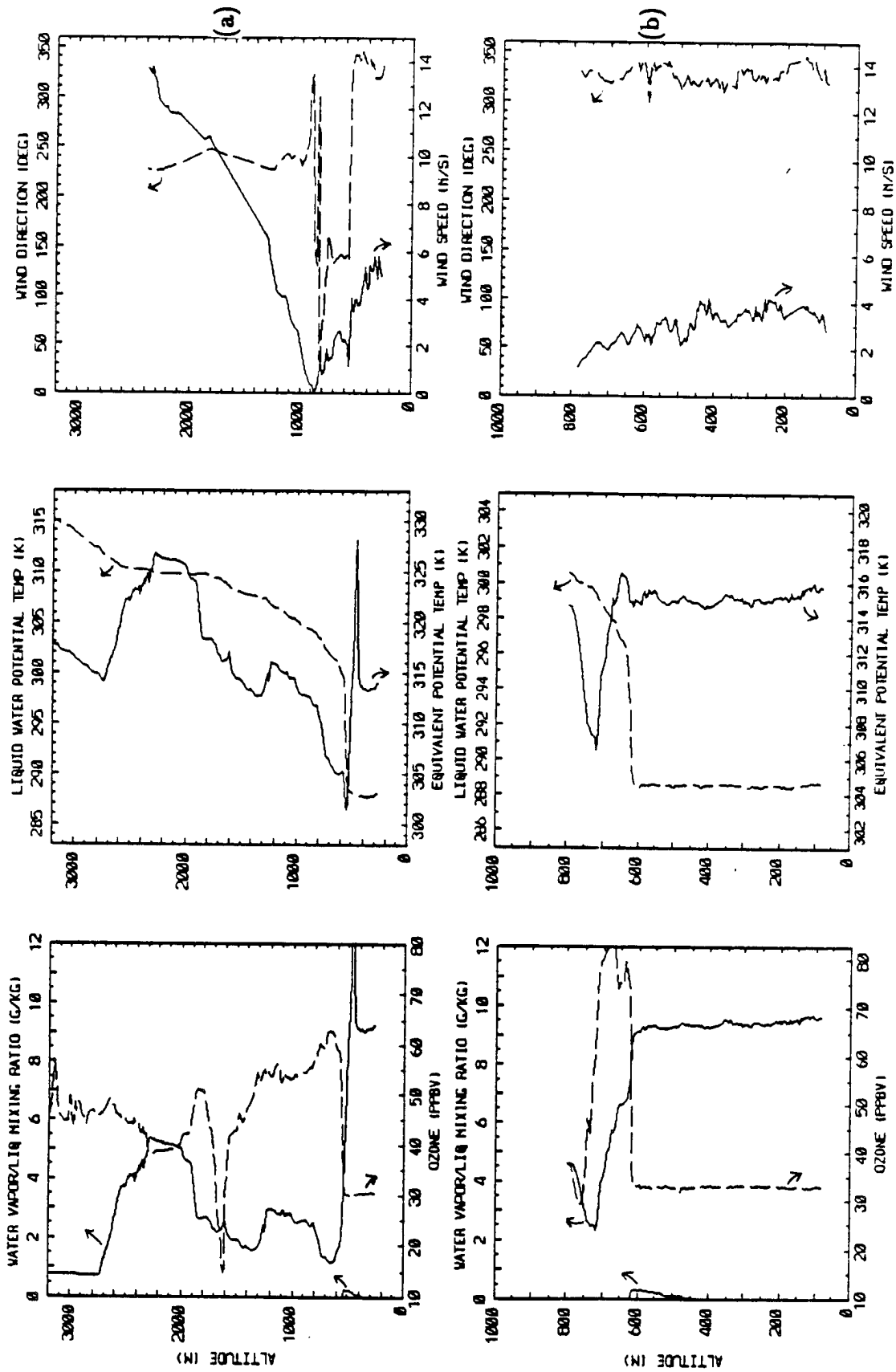

Figure A.5: Flight 3, spiral descent 10:42-10:55(a) and slant descent 13:36-13:47(b).

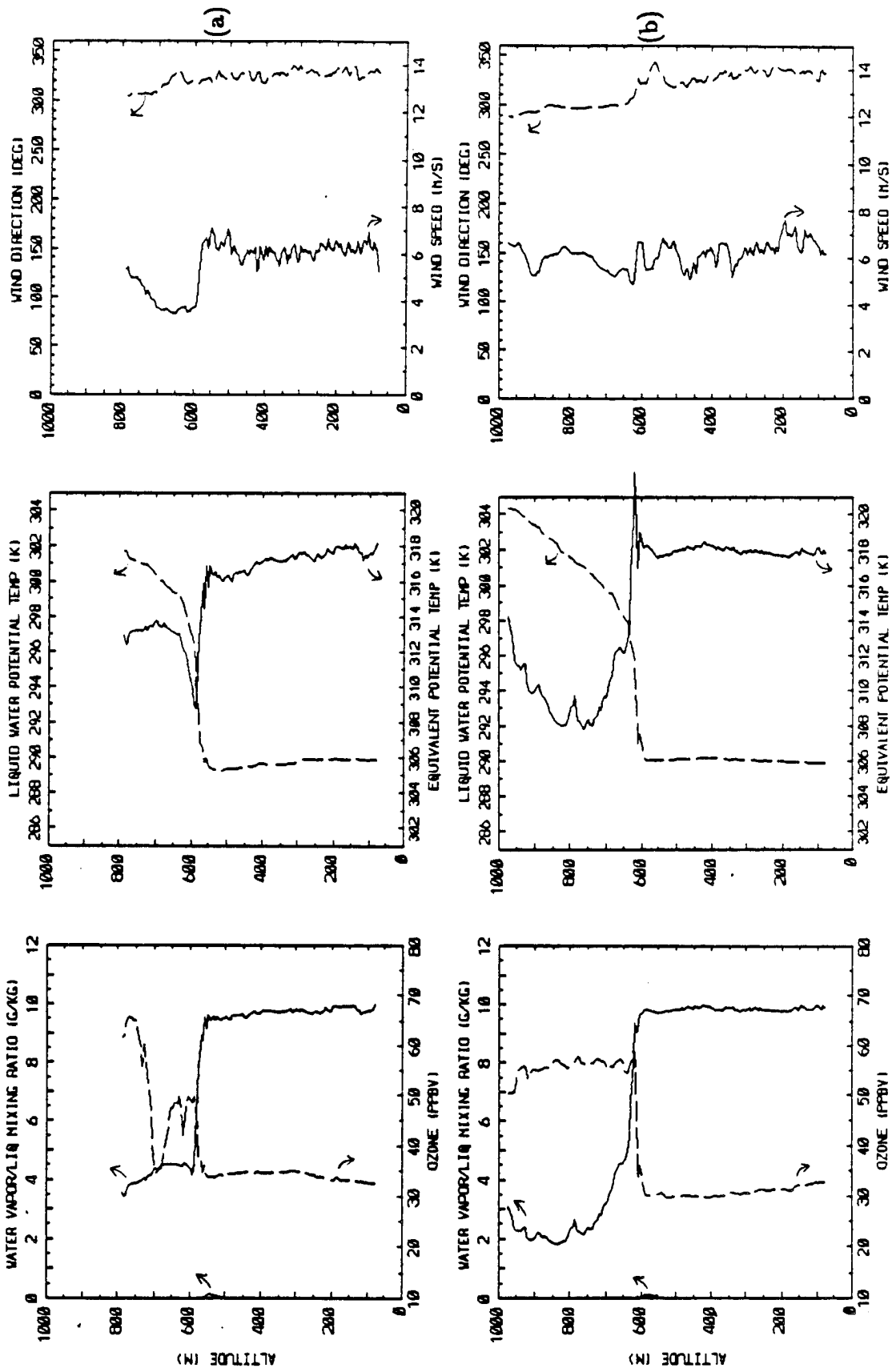

Figure A.6: Flight 3, slant descent 15:30-15:43(a) and ascent 15:43-15:48(b).

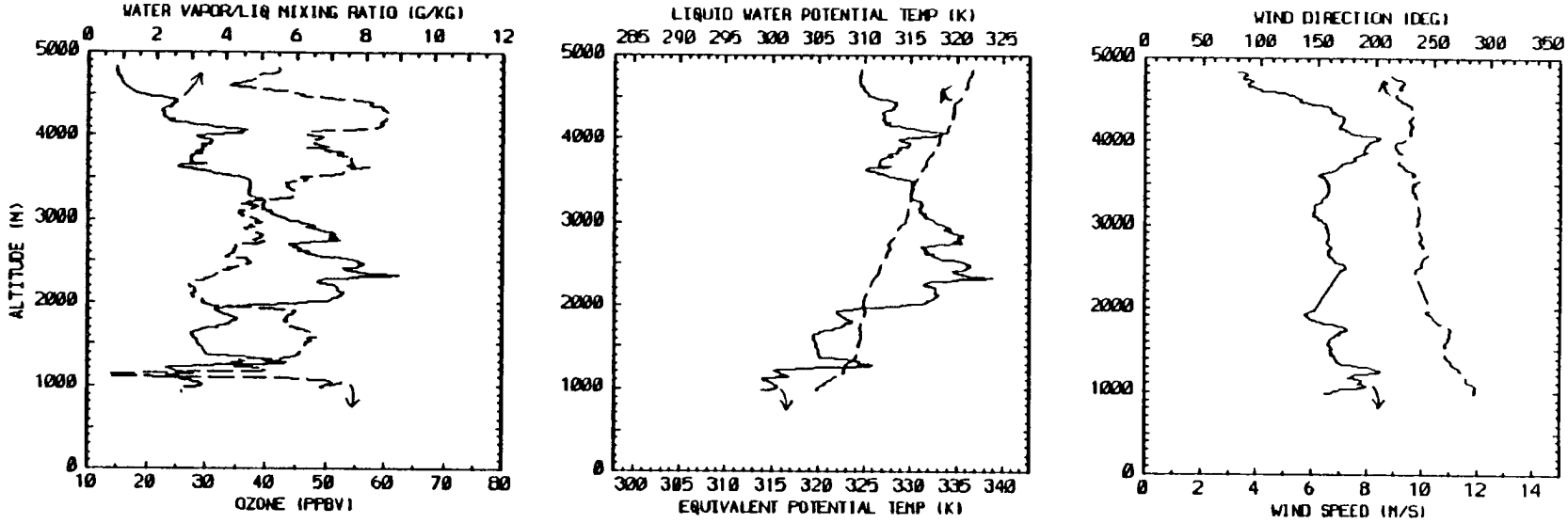

Figure A.7: Flight 3, spiral ascent 15:55-16:05.

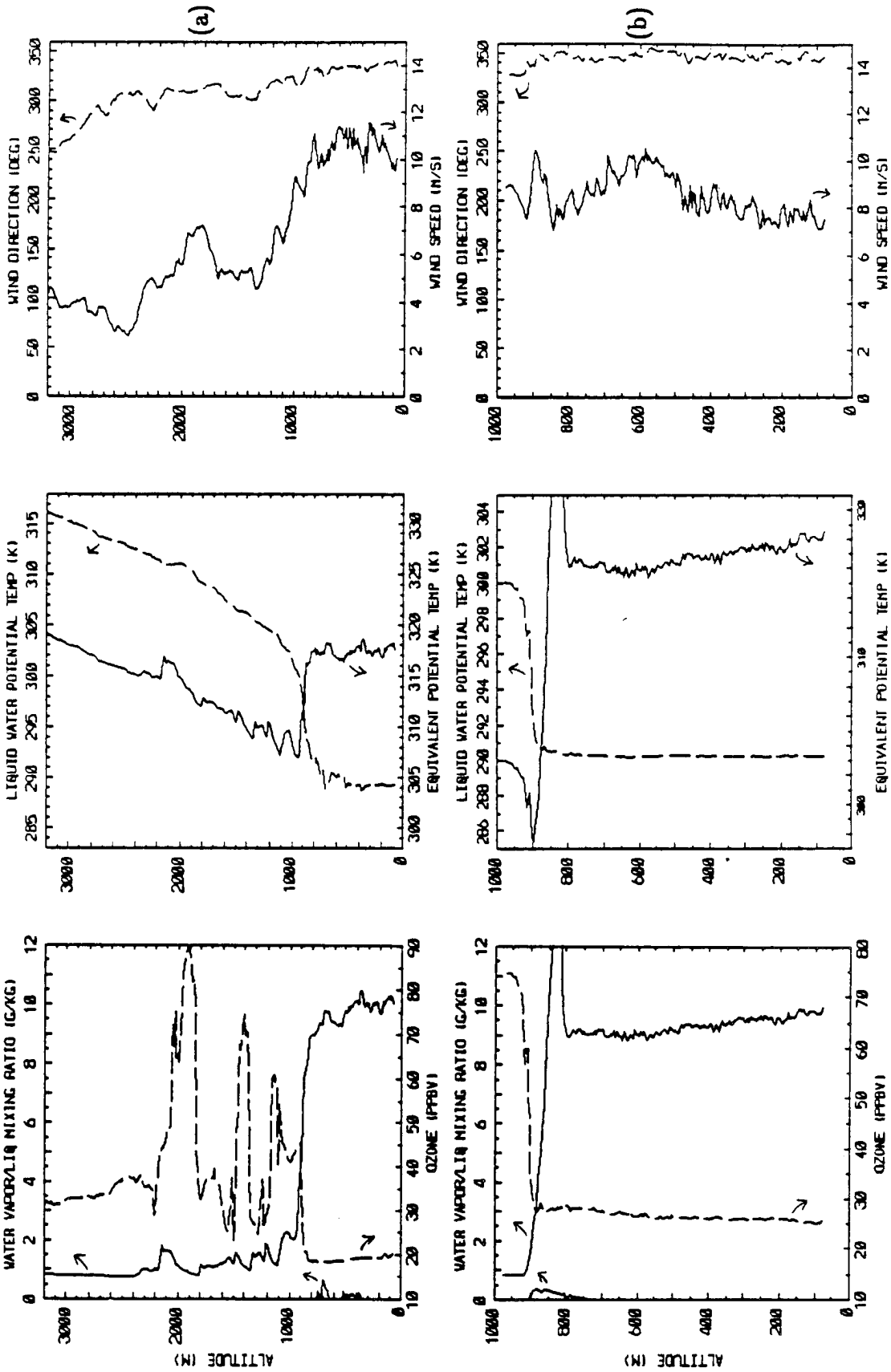

Figure A.8: Flight 4, slant descents 11:03-11:19(a) and 13:52-13:59(b).

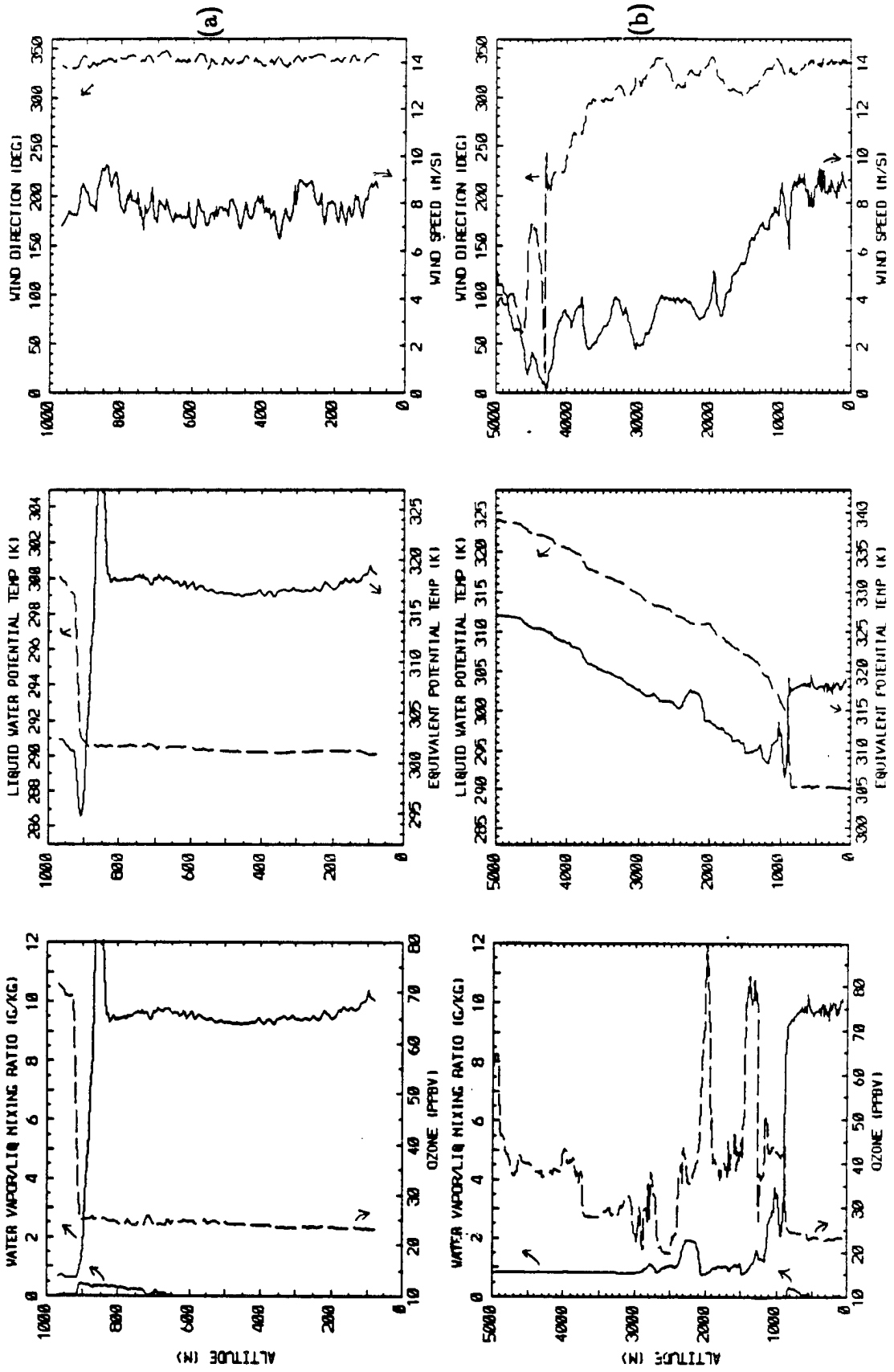

Figure A.9: Flight 4, slant descent 15:41-15:49(a) and ascent 15:49-16:09(b).

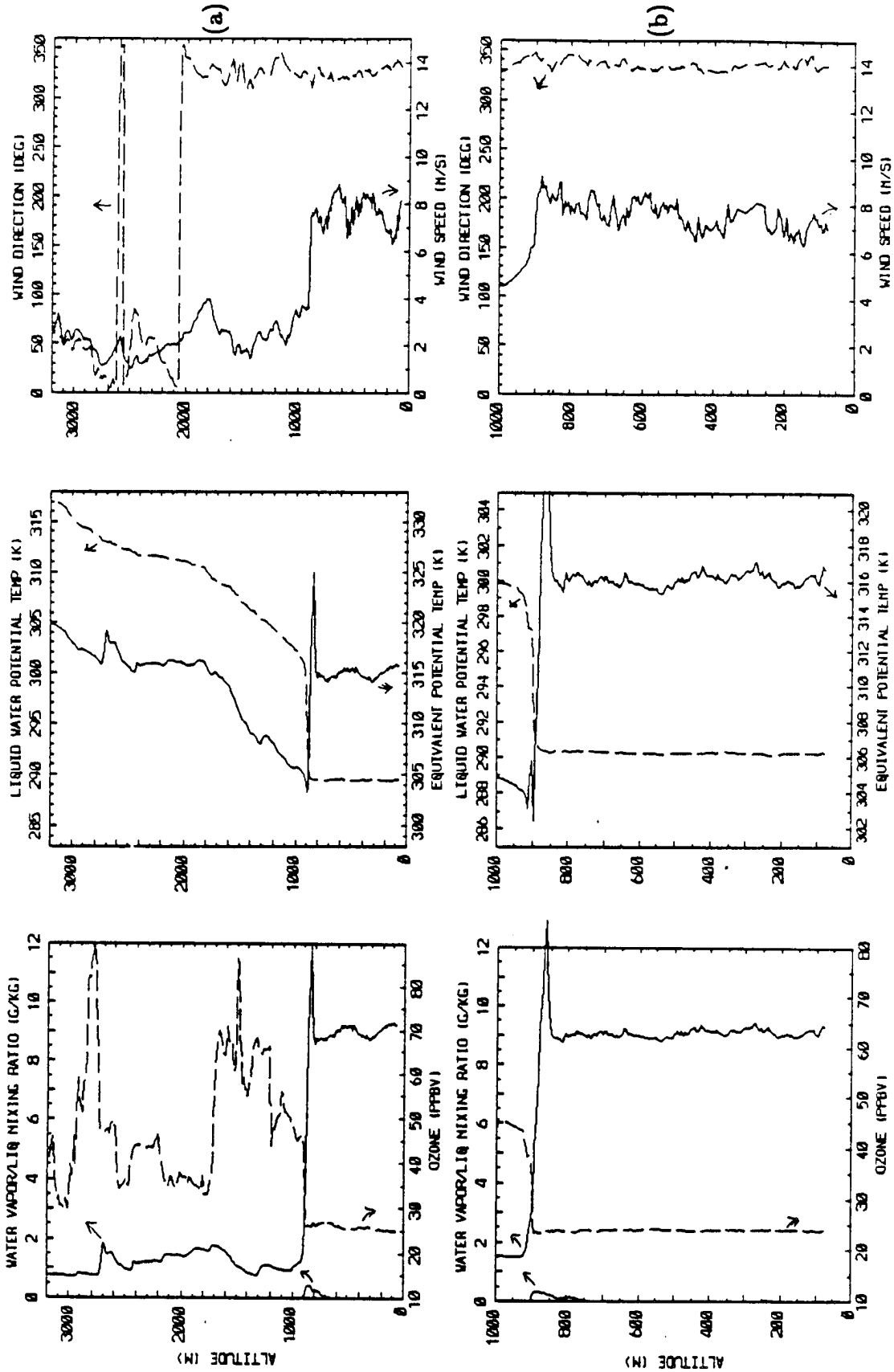

Figure A.10: Flight 5, slant descent 10:50-11:05(a) and spiral ascent 13:38-13:46(b).

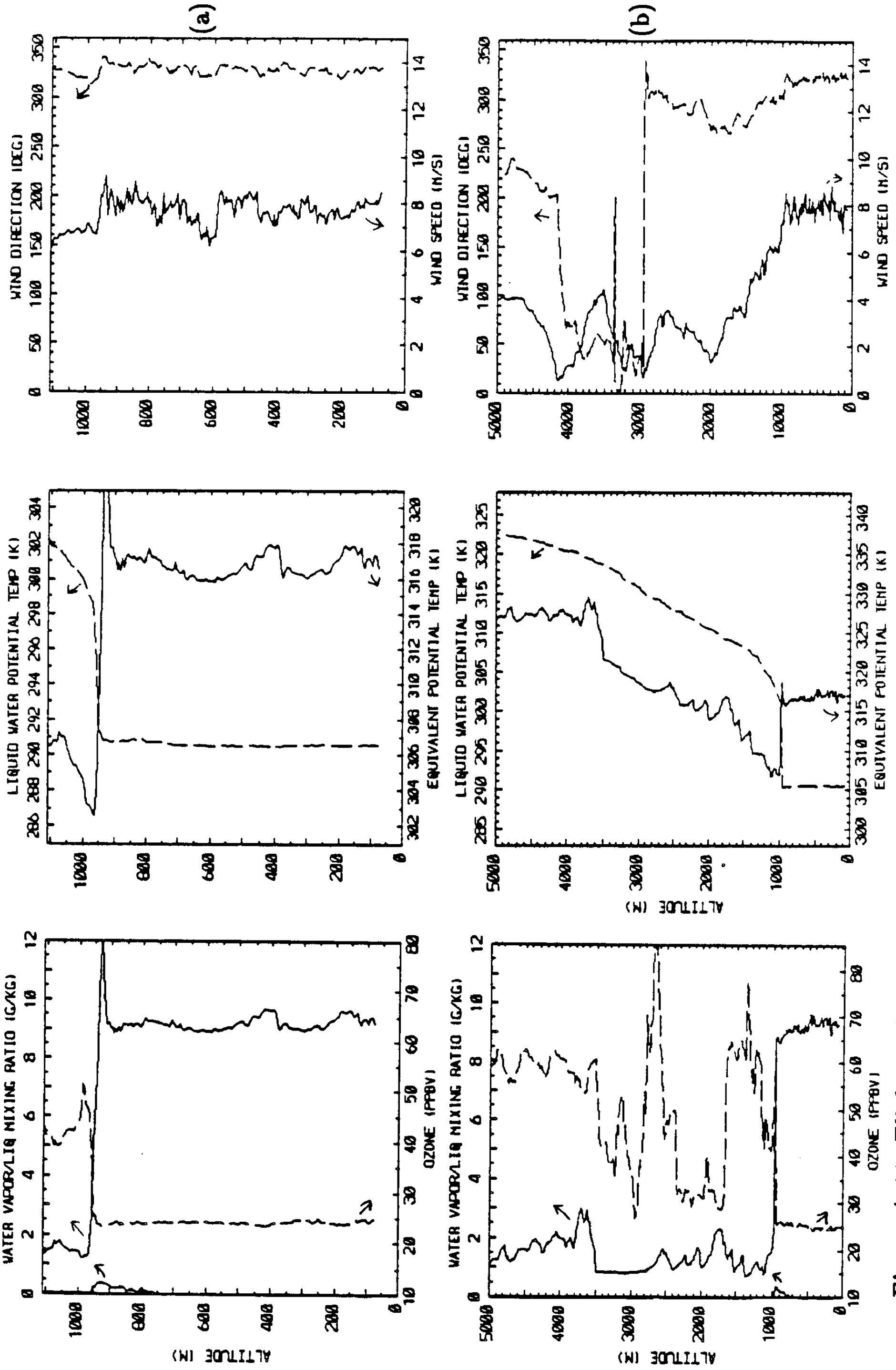

Figure A.11: Flight 5, slant descent 15:29-15:38(a) and ascent 15:38-15:55(b).

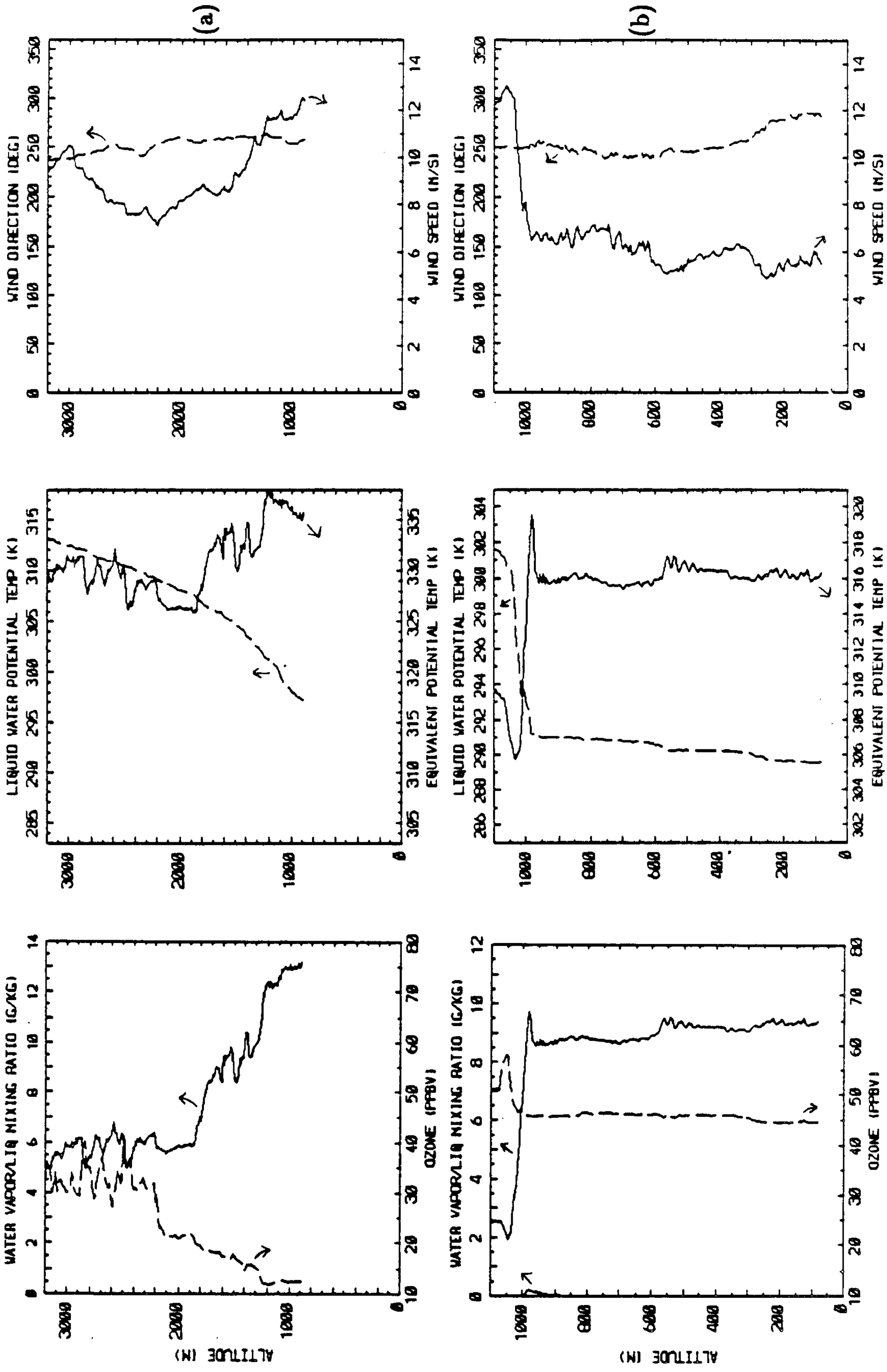

Figure A.12: Flight 6, slant descents 11:44-11:51(a) and 12:19-12:27(b).

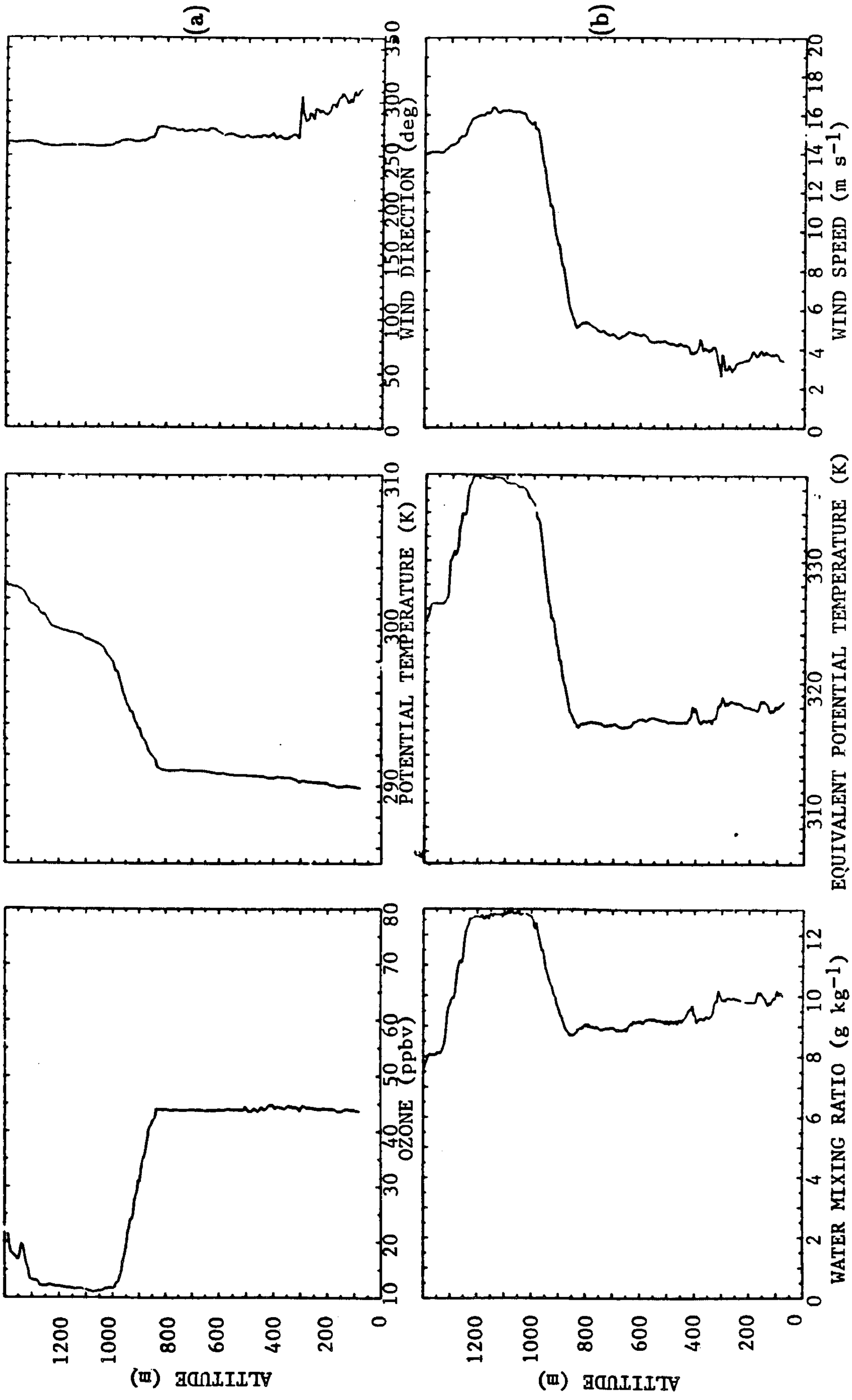

Figure A.13: Flight 6, slant ascent 14:00-14:09. Liquid water is zero throughout.

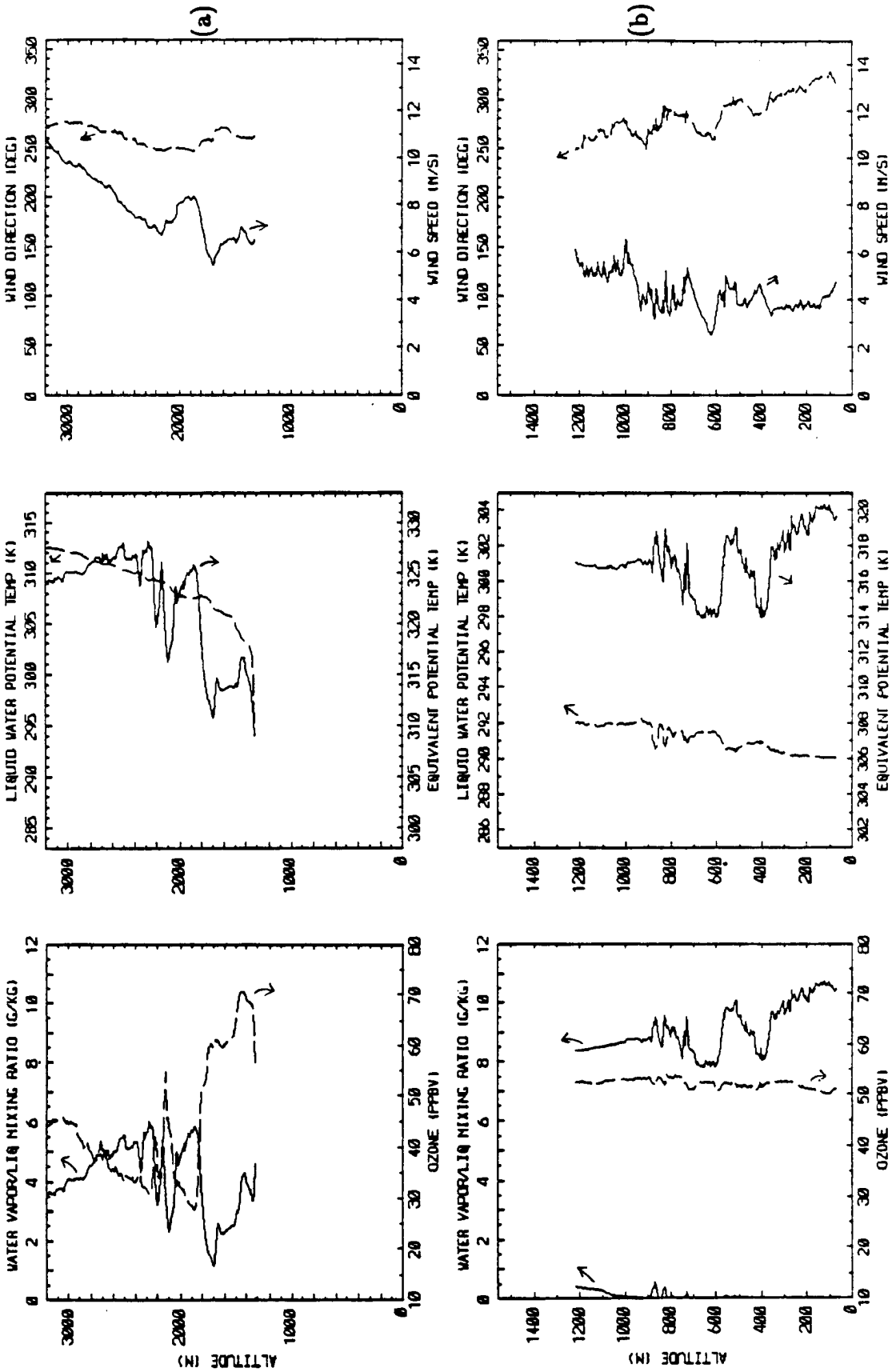

Figure A.14: Flight 7, slant descents 11:13-11:19(a) and 11:42-11:53(b).

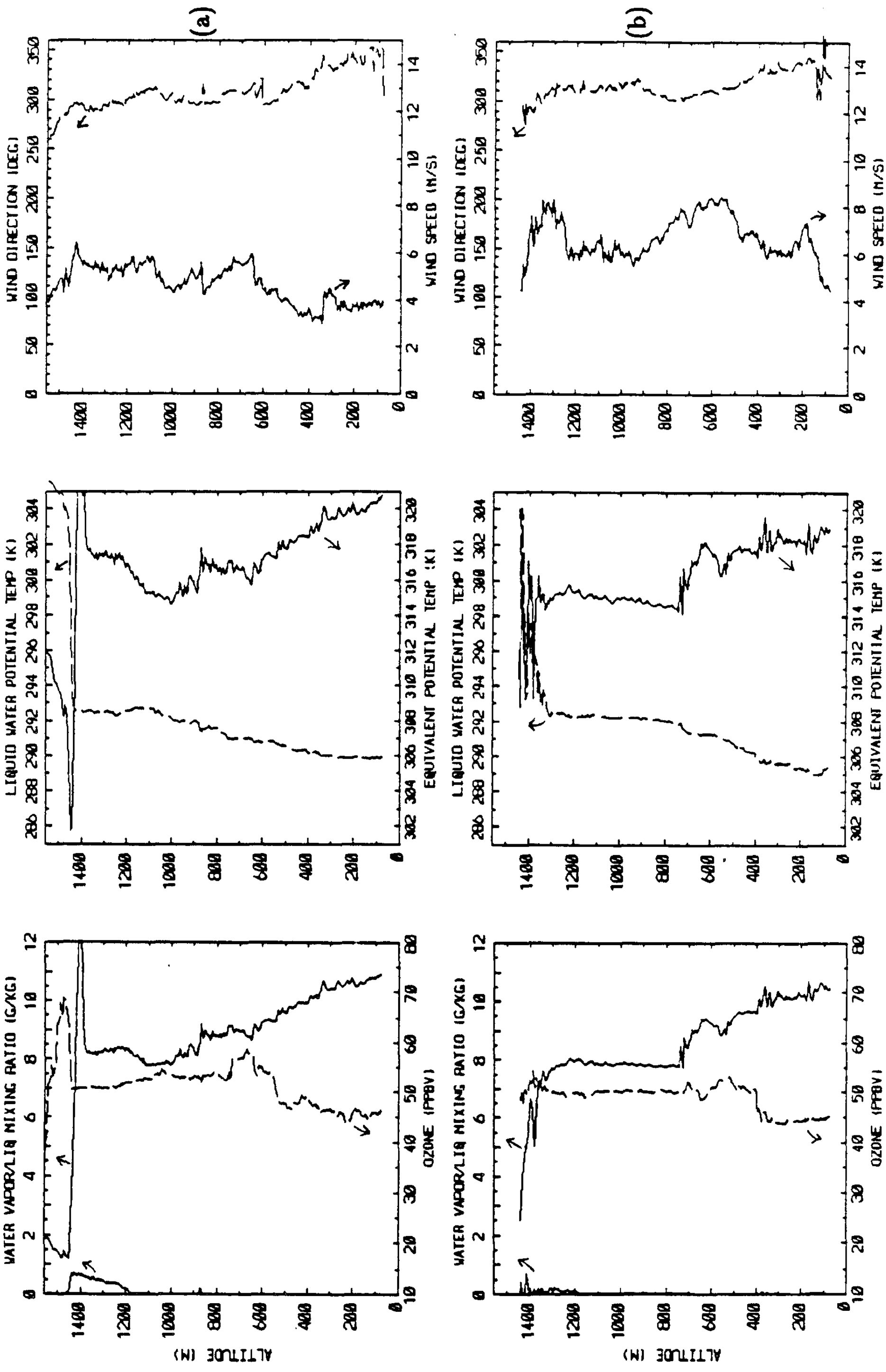

Figure A.15: Flight 7, slant descents 14:20-14:35(a) and 16:20-16:31(b).

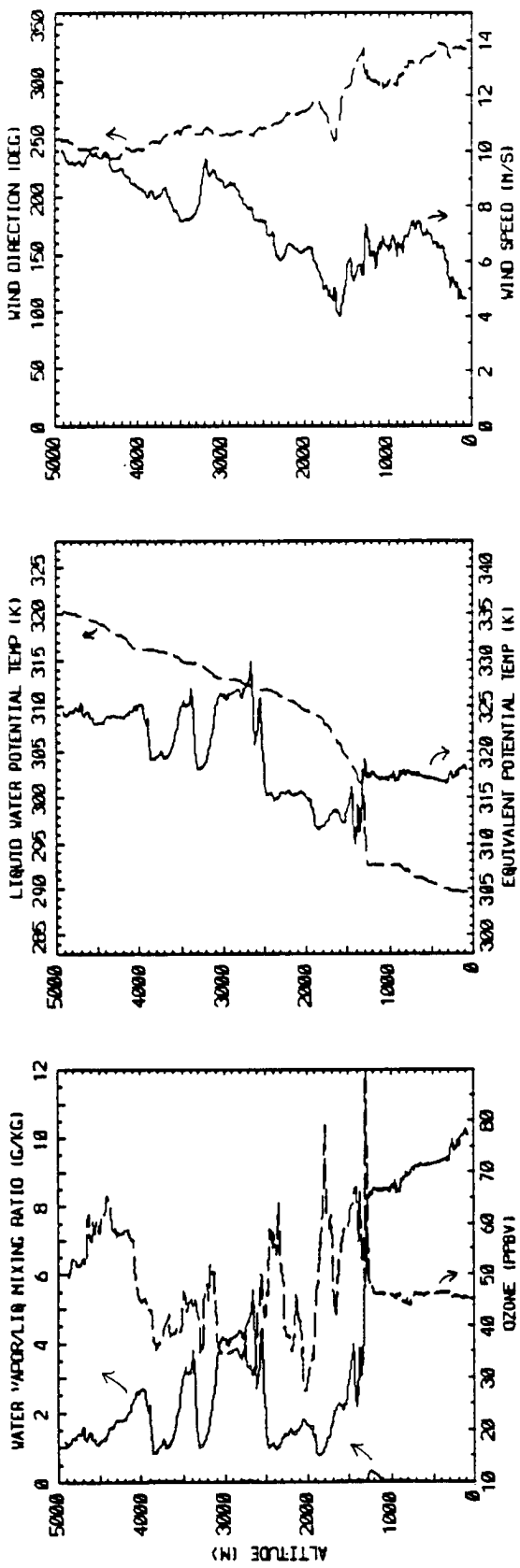

Figure A.16: Flight 7, slant ascent 16:31-16:49.

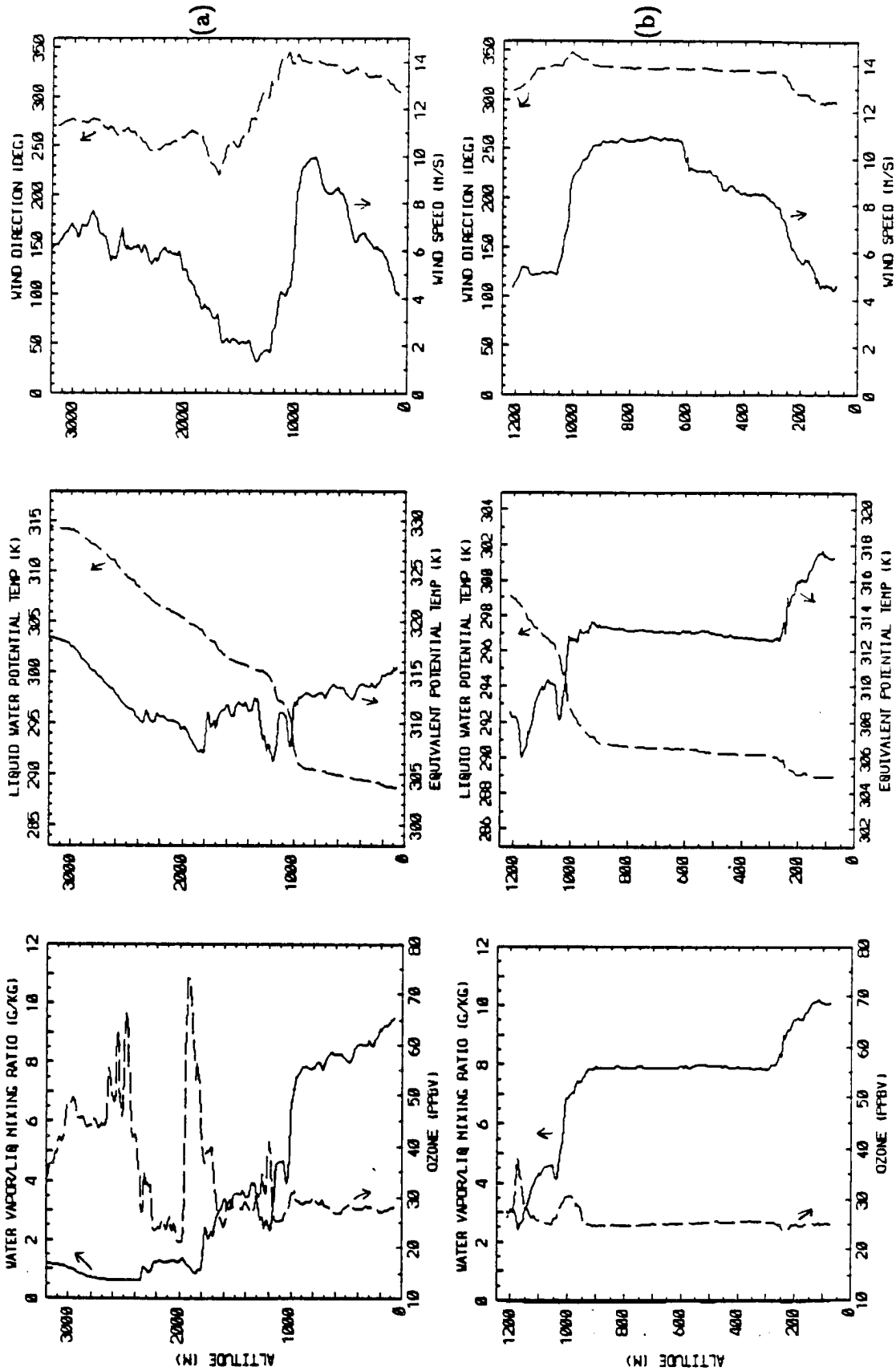

Figure A.17: Flight 8, slant descents 11:18-11:35(a) and 13:48-13:59(b).

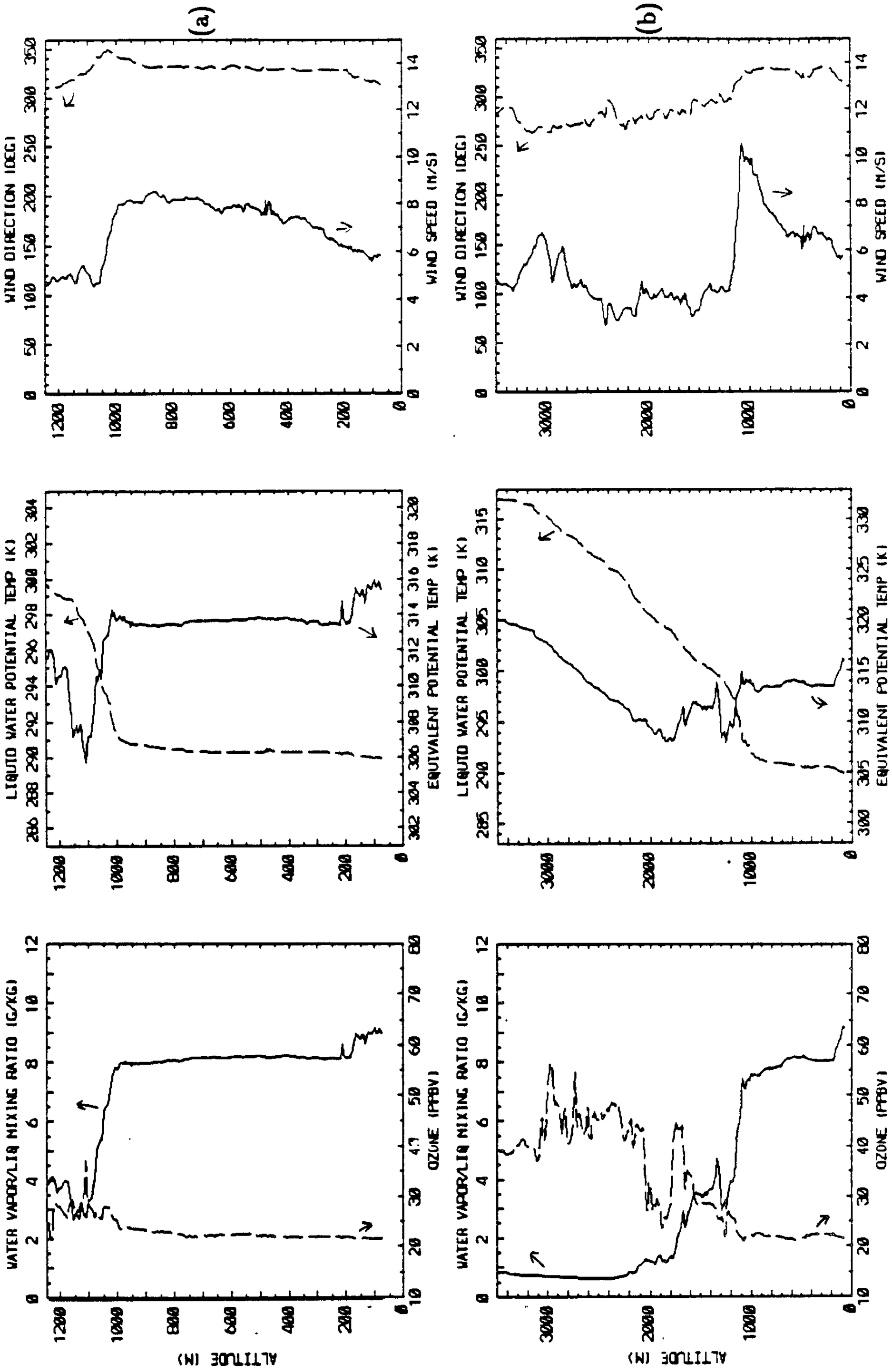

Figure A.18: Flight 8, slant descent 15:21-15:31(a) and ascent 15:31-15:45(b).

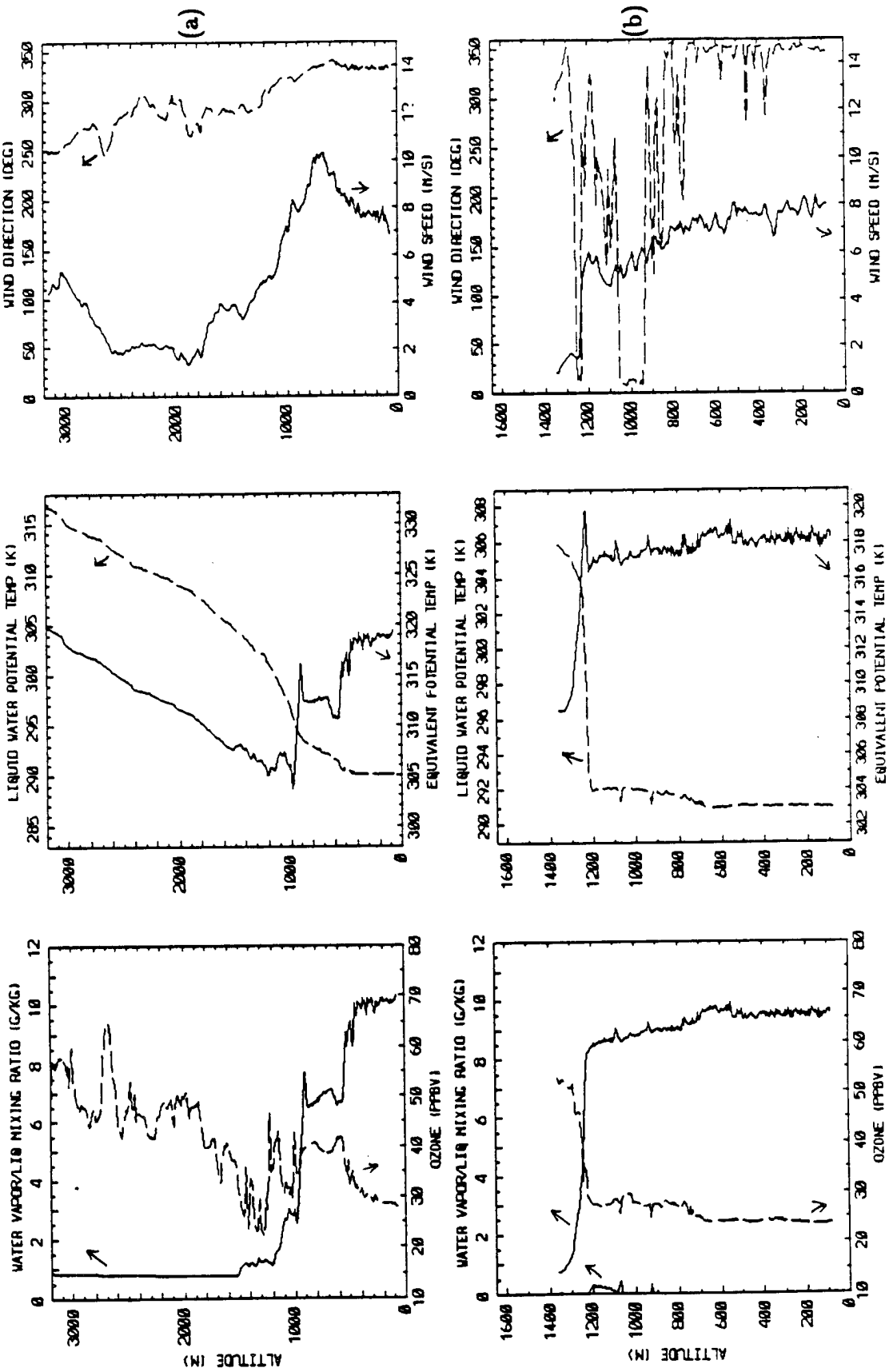

Figure A.19: Flight 9, slant descent 11:58-12:12(a) and ascent 12:59-13:07(b).

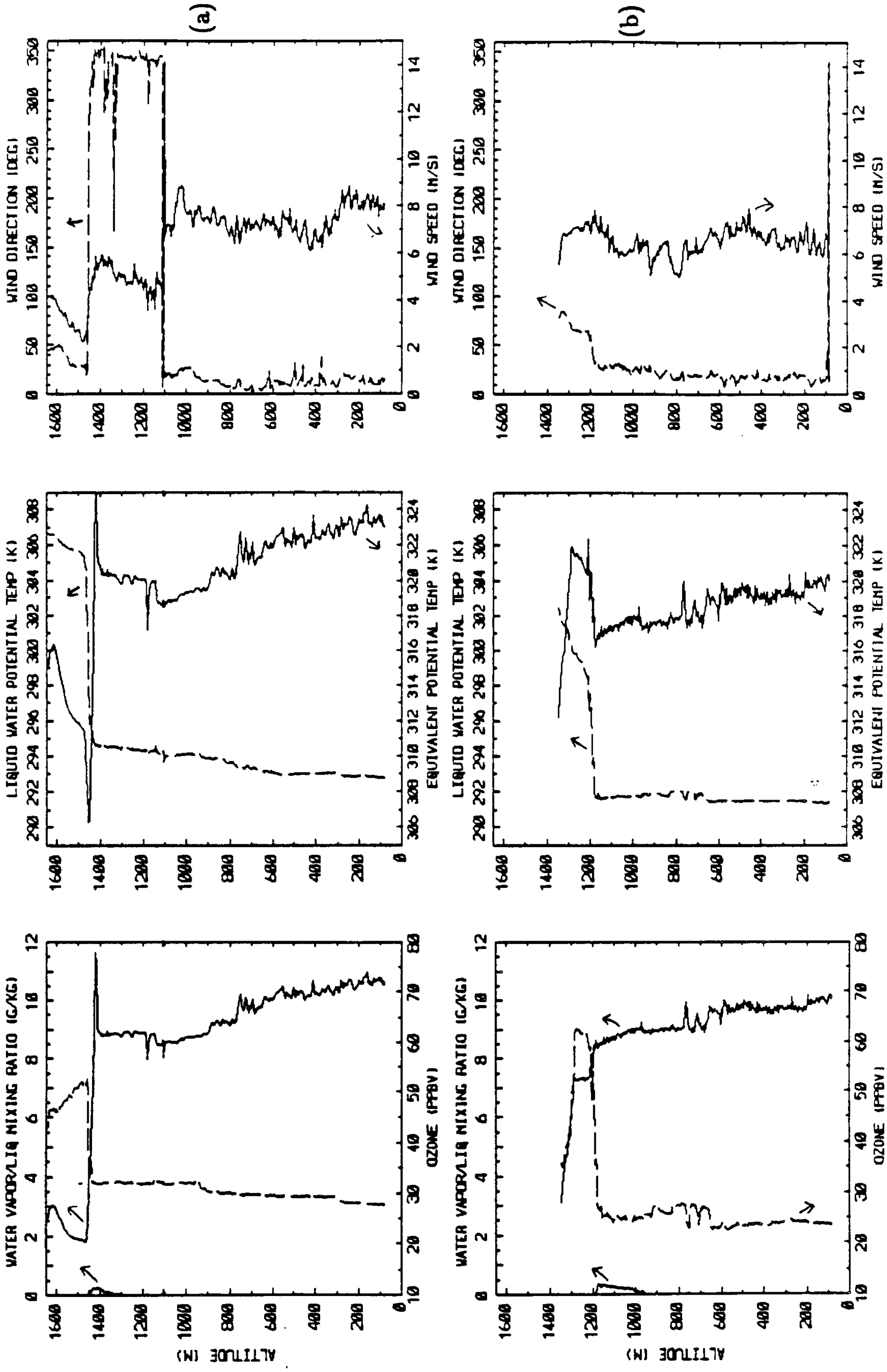

Figure A.20: Flight 9, slant descent 14:12-14:27(a) and ascent 15:14-15:22(b).

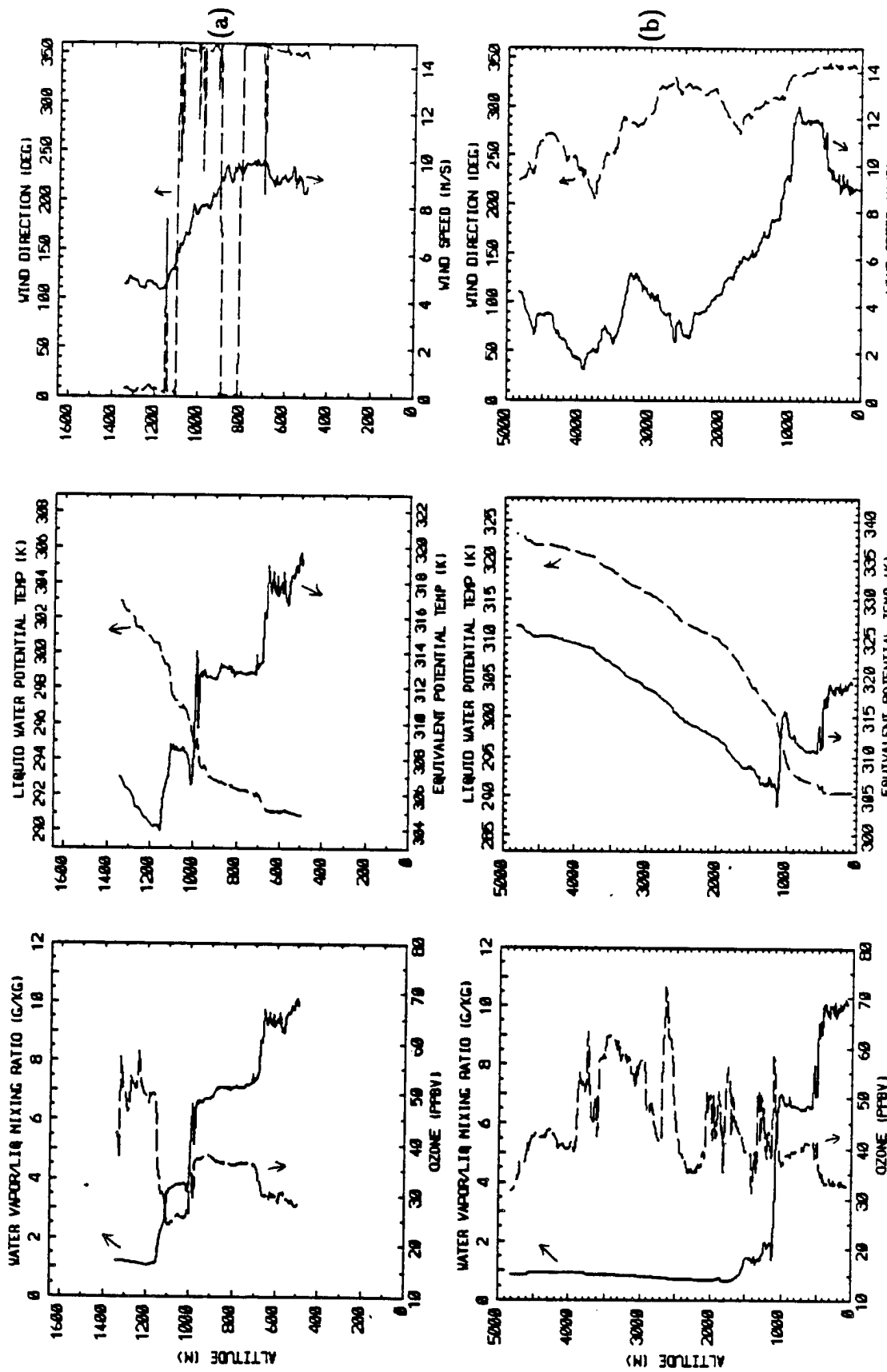

Figure A.21: Flight 9, slant descent 15:52-16:00(a) and ascent 16:51-17:09(b).

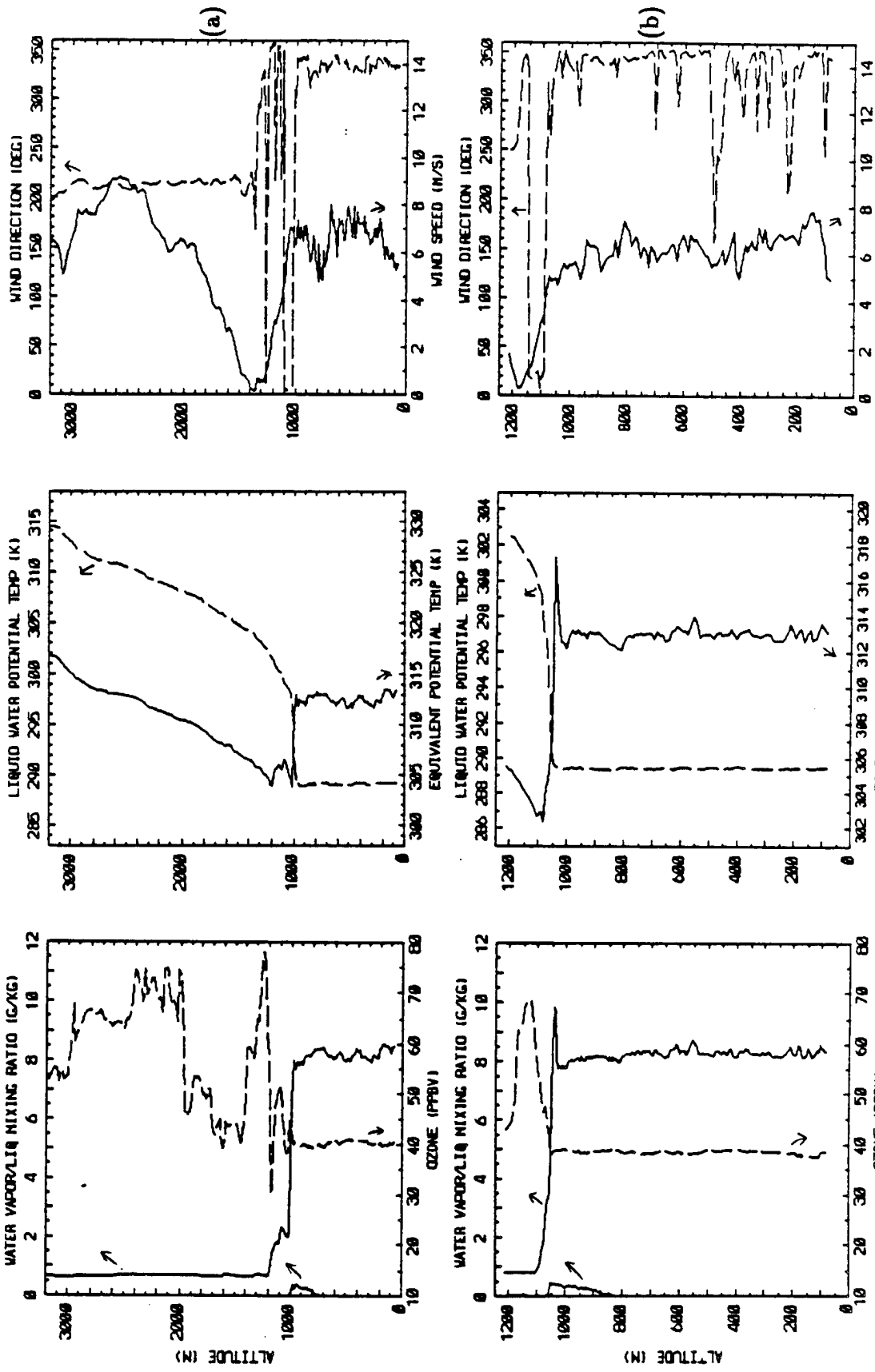

Figure A.22: Flight 10, slant descents 06:25-06:40(a) and 09:17-09:25(b).

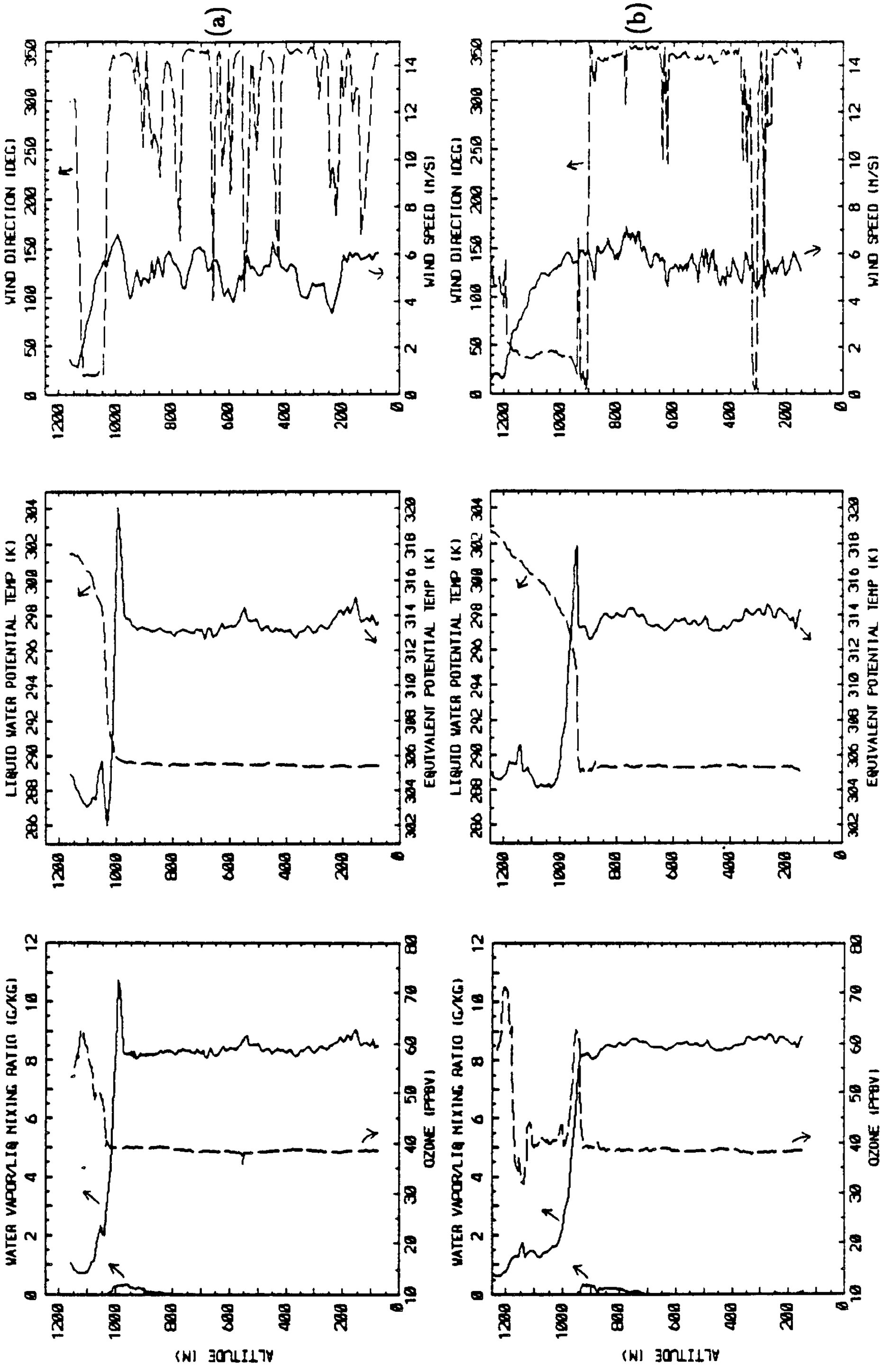

Figure A.23: Flight 10, slant descent 11:05-11:13(a) and ascent 11:17-11:25(b).

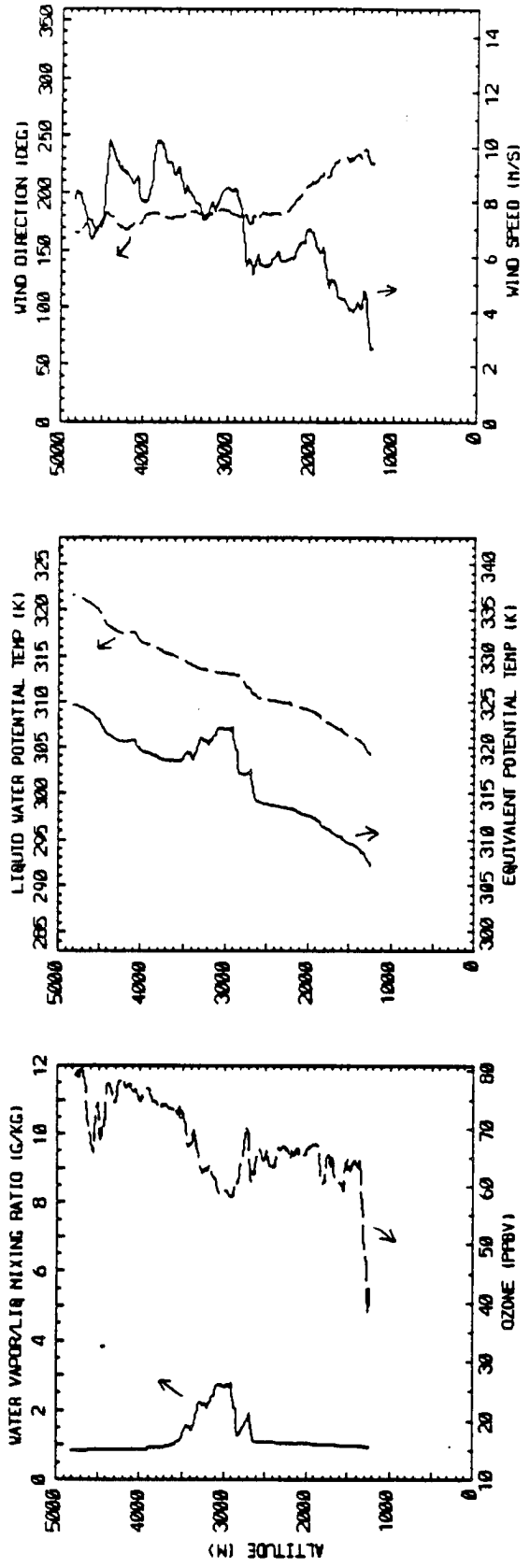

Figure A.24: Flight 10, slant ascent 11:40-11:52.